Master thesis and internship[BR]- Master's thesis : Evaluation of an OpenFOAM-based software for thermal topology optimisation using the continuous adjoint approach[BR]- Integration Internship

Auteur : Atceken, Seyda Nur
Promoteur(s) : Duysinx, Pierre; Terrapon, Vincent
Faculté : Faculté des Sciences appliquées
Diplôme : Master en ingénieur civil en aérospatiale, à finalité spécialisée en "aerospace engineering"
Année académique : 2021-2022
URI/URL : http://hdl.handle.net/2268.2/14585

University of Liège
Faculty of Applied Sciences

Evaluation of an OpenFOAM-based software for thermal topology optimisation using the continuous adjoint approach

Academic supervisors: Prof. V. Terrapon & Prof. P. Duysinx

Internship supervisor: Ir. L. Fitschy

Graduation Studies conducted for obtaining the Master's degree in Aerospace Engineering by Seyda Nur Atceken

Master thesis realised in collaboration with GDTech

Academic year 2021-2022

Acknowledgements

I would like to thank all my teachers that had an important impact in the person I have became. I am grateful to have had passionate teachers that managed to transmit their knowledge to me, and especially my secondary school Math teachers Mr Gioé, Mr Vandries, Mrs Lemaire and Mrs Swinnen. I dedicate a special thanks to Mr Terrapon and Mr Duysinx for their interest in my thesis and the mastery they have transmitted to me.

Then, I would like to thank GDTech, and especially the CFD department who had allowed to treat the current thesis. I dedicate a big thank to my supervisor Laurent and its colleague Nicolas for their precious help and availability during my internship.

I also thank my friends for their big support during my studies. I would have been unhappy without their presence.

Finally, I want to affirm my biggest acknowledgement to my lovely mum. She is the only one who unconditionally loves and supports me. I cannot say enough how lucky I am to have such a personality like her in my life, and I wish her the best even if life can throw at us difficulties.

Topology optimisation: Application and validation of the density-based method on a conjugate heat transfer problem

Seyda Nur Atceken

Academic supervisors: Prof. V. Terrapon & Prof. P. Duysinx
Internship supervisor: Ir. L. Fitschy
Master in Aerospace Engineering
Faculty of applied sciences, University of Liège
Academic year 2021-2022

Abstract

This thesis deals with density-based topology optimisation applied in the scope of a conjugate heat transfer problem. After an explanation of the methods of topology optimisation, the latter is specified to fluid based problems, and especially to conjugate heat transfer applications for which the density-based method is used.

The goal of the optimisation is to maximise the heat transferred to the coolant fluid while limiting the pressure drops as much as possible. A single type of design variable stands for the representation of the material distribution. Through this variable, the presence of solid will be taken into account thanks to a Brinkmann type penalisation term that is included in the flow equations. This term blocks the flow where there should be solid material. The temperature is modelled through the convection-diffusion equation which describes both conduction in the solid and convection in the fluid. As the gradient-based approach is used to perform the optimisation, the design variable can take intermediate values which leads to an unclear topology. To cope with this, a processing of the design field known under the name of the Three Field Scheme Topology Optimisation is used.

The analysis of the density-based topology optimisation is conducted on a simple conjugate heat transfer problem using the *adjointOptimisationFoam* solver of OPENFOAM. The optimisation conducted topologically proves its efficiency by increasing up to almost 200% the heat transferred to the coolant fluid, and a drastically reduced pressure drop compared to the initial configuration of the domain.

The method is then applied on the optimisation of a 3D heat exchanger subjected to a highly turbulent flow. Although the design generated by the optimisation is not converged, the method gave interesting topologies for the first optimisation cycles.

Contents

List of Figures

List of Tables

1

Chapter 1

Introduction

1.1 Context and motivations

Optimising mechanical systems has always been the point of interest of engineers desiring better and better performances. The fast development of computer aided programming along with the validation of new methods has permitted to introduce sophisticated tools in the scope of optimisation. Researchers being driven by the wish of creating more and more optimal designs, lots of scientific studies have been led in the area. The utilisation of optimisation methods is in fact a good alternative to conducting experiments on predefined structures that could be expensive to do.

There exist several methods of optimisation. These can be grouped in three main categories: size, shape, and topology optimisations. These are illustrated in Fig. 1.1. Size optimisation consists in only changing the dimensions of the components of a given structure such as the cross sectional area. Shape optimisation differentiates itself by the fact the boundaries are first defined and then the optimisation process leads to modifications in the boundary. In contrast to that, topology optimisation can create new boundaries, new holes, and can also modify the dimensions of the system.
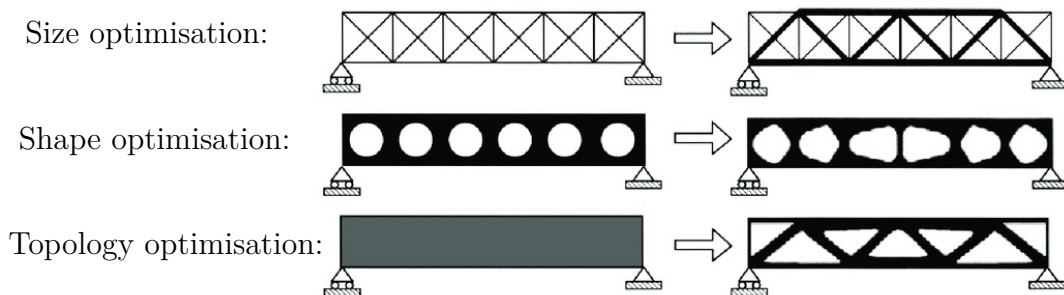
Figure 1.1: Comparative illustration of size, shape, and topology optimisations [1].

Given the bigger freedom in topologically optimised structures, topology optimisation (TO) is the most revolutionary method. Topology optimisation saw a growing importance in the past few decades in the design process of optimal structures. With the flexibility brought by additive manufacturing (AM), the use of topology optimisation has been prompted in order to create non-intuitive structures that meet challenging objectives. Together with the ease of AM, complex shapes that fulfil burdensome criteria can be manufactured. The idea is to find the optimal distribution of material given a certain objective function that has to be minimised (or maximised) and some constraints that have to be verified. Thus, the question is "where to put the material ?" or similarly "where the holes should be ?". Today, topology optimisation is a mature technique in the scope of solid mechanics where the method sees its origins. Topology optimisation techniques are available in almost all finite element analysis (FEA) packages and computer aided design (CAD) packages. The very first application of topology optimisation dates back to 1904 with Michell's truss theory invented by George Michell [3]. The aim of the method was to decrease the volume of trusses under a single load and a stress constraint. In the late 1980s, topology optimisation saw again the day with the works of Bendsoe and Kikuchi on the homogenisation method [4]. With their article, topology optimisation became a revolutionary technique. Soon after, the SIMP method has been developed by Bendsoe [5] and Rozvany *et al.* [6]. In the beginning of the 2000's, the level set method was introduced successively by Wang *et al.* [7] and Allaire *et al.* [8].

All of these methods have been applied to structural mechanics problems. They can also be applied to problems including various types of physics where the governing equations can be expressed by partial differential equations. The method is in fact extendable to fluid flow, acoustics, electromagnetism, biomedical designs, etc [9].

As topology optimisation can be coupled to any type of application, this efficient method is now commonly used in thermal applications. The optimisation of thermal systems mainly relied on trial and error methods which are very time consuming and expensive due to the need of experimental data. With topology optimisation, much more sophisticated topologies are created in an efficient way with a great enhancement of the features of the design.

1.2 Objectives

The goal of this thesis is to first figure out the methodology that is behind topology optimisation. A detailed explanation of the methods used in general topology optimisation problems will be provided. Then, the specification to fluid-based problems, applied in this study to conjugate heat transfer (CHT) problems, will be done.

Once the theory is understood, a practical CHT application will be considered in 2D. This consists in the heat transfer between a solid body and a fluid flowing inside it. The objectives of this study will be to maximise the heat transferred to the coolant fluid while minimizing the pressure drops. This analysis will then permit to see the effects of the different parameters involved in the optimisation.

After that, the method will be validated using a body-fitted mesh. The computed heat transfer and pressure losses given by this body-fitted mesh will be compared to the results of topology optimisation. This will allow to corroborate the approach used in fluid based topology optimisation.

Then, the optimisation of a 3D heat exchanger subjected to a highly turbulent flow will be tried. This will show how difficult is to treat such a problem.

The study will finally end with perspectives of what could be done in future works. These will give an insight of the points that have to be handled in order to ameliorate the methodology used in topology optimisation.

1.3 Thesis outline

Following this introductory chapter, a detailed theoretical study of topology optimisation will be done in chapter 2. The theory will be first explained for general methods of topology optimisation that have been already used in structural mechanics. Then, a specification for the fluid based problems will be performed. A review of existing works of topology optimisation in fluid problems will be done. Following this, the governing equations used for the density-based method applied on CHT problems will be constructed. Together with this, new developments related to the treatment of the material distribution will be presented. After that, the continuous adjoint formulation will be provided. The latter being commonly used in topology optimisation problems, it will be specified for the case of a CHT problem. The chapter will finally end with the general procedure of topology optimisation in fluid problems. Subsequently, a complete study of the parameters involved in CHT topology optimisation will be done in chapter 3. To do this, the *adjointOptimisationFoam* [10] solver of OpenFOAM will be used. Then, the optimisation of the 3D heat exchanger will be handled in chapter 4. The work will end in chapter 5 with a brief conclusion and future objectives.

Chapter 2

Theoretical background

In this chapter, the principal different methods that exist in topology optimisation will be briefly described. Then, a chronology of the method will be done with pioneering works in the scope of fluid based problems. Subsequently, the technique will be mathematically specified using the density-based method for fluid applications, and especially CHT problems, with a detailed explanation of the adjoint formulation and all other particularities related to these types of problems.

2.1   Methods in topology optimisation

The general methodology of a topology optimisation problem is to find the optimal distribution of material, given a design domain, constraints and an objective function that describes the performance of the system that has to be minimised (or maximised). To do so, topology optimisation seeks for the optimal value of a certain design variable value at each node (for vertex-centered codes) or cell (cell-centered codes). The two significant values of this design variable are one and zero to which correspond respectively solid and void entities.

There exist two main categories of topology optimisation techniques that can be found in the literature. These are the gradient-based (GB) and non-gradient based (NGB) algorithms. The GB algorithms are the most mature ones with various methods that will be described later. NGB algorithms are quite new and keep appearing in the literature.

In the current thesis, the GB method will be used. As the gradient information is needed, the design variable has to vary continuously between zero and one, corresponding respectively to void and solid, in order to be able to compute the gradient. This leads to grey regions which are difficult to interpret and blur the transition from solid to fluid regions. Nevertheless, there exist numerous techniques that permit to obtain a discrete 0-1 design. These techniques are for example the penalisation, thresholding, or projection methods that will be explained later. The computation of the gradient may seem to be very costly as the number of design variable is very high in a practical topology optimisation problem. But this is not

a big issue since there exists a very efficient way of computing the gradient with the adjoint formulation that will be clarified later.

When using GB methods, the dependency of the obtained solution on the initial guess is highly important. There are lots of design variables and the convergence to a global optimum is less and less susceptible with increasing number of design variables. This is illustrated in Fig. 2.1 for an arbitrary 2D function $f(x_1, x_2)$. The optimisation path, and hence the obtained solution greatly depend on the initial conditions. Note that the center of smallest contour circles correspond to the minima of an arbitrary 2D function whose values are not shown for sake of clarity. This aspect is very difficult to cope with when employing topology optimisation problems. Nevertheless, GB methods are widely used in the scope of topology optimisation, and there are many methods that are mature enough and have been widely used. They are summarized in the following subsections.
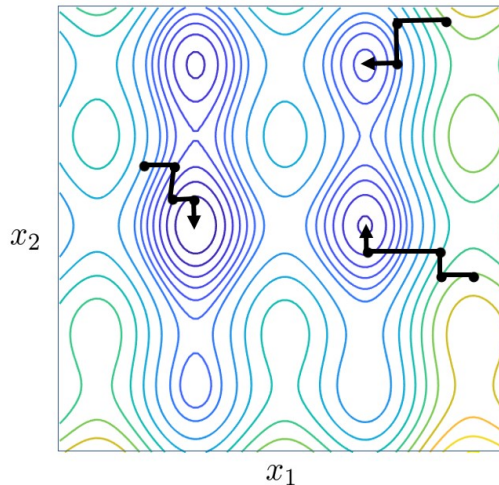
Figure 2.1: Contour plots of an arbitrary 2D function $f(x_1, x_2)$ with three different optimisation paths depending on the initial guess.

2.1.1 Homogenisation method

Introduced by Bendsoe and Kikuchi [4], the homogenisation method is considered to be the pioneering work in computed-aided topology optimisation. In this technique, the computational domain is divided into finite elements. Each of them are treated as porous material with controllable micro-structures. The micro-structures are constructed with a certain periodicity with some voids inside the element. By tuning the micro-structures of the unit cells, the macro-scale properties can be adapted in order to give rise to a structure that is well-suited for some stress level and minimise a given objective function.

2.1.2 Hard kill methods

The hard kill methods can be seen as 'discrete' methods in which each element is handled as material or void. The idea of these methods is to remove and add gradually elements, that are filled with material or that are void, into the structure.

The most well-know method is the evolutionary structural optimisation (ESO) [11] in which the elements are removed gradually. Its recent version, called bi-directional evolutionary structural optimisation (BESO) [12], permits also the addition of elements that are filled or not with material. In these methods, 'grey' elements, i.e. elements that are neither filled totally with material nor void, are omitted thanks to the explicit addition or removal of material.

2.1.3 Boundary variation methods

Boundary variation methods were firstly used in shape optimisation. Boundary movement techniques in topology optimisation allow both changes in the structural boundaries as in shape optimisation, but also topological changes, i.e. creation, disappearance, and combination of void zones.

One of the techniques commonly used is the level-set method. The boundaries are represented implicitly through the contour line of a field that depends on the design variable. This field is a scalar function ϕ called the level-set function. The boundaries are represented by closed curves Γ defined as

$$\Gamma \equiv \{(x, y) | \phi(x, y) = 0\}.$$

Thereupon, the boundaries are modified implicitly by controlling the level-set function taking into consideration the considered physical problem and optimisation conditions [13].

This method was first introduced by Osher and Sethian [14] for moving interface problems in physics. It has then been used in numerous research areas [15, 16], and then in topology optimisation in the early 2000s by Sethian and Wiegmann [17] where the goal was to represent the free boundary of a structure for linearly elastic problems.

2.1.4 Density methods

Density based methods are the most popular techniques used structural topology optimisation. These are an extension of the homogenisation method. The advantages of using such a process is its simplicity and ease of implementation. They have the ability to change dramatically the design of a given structure. This is done thanks to the knowledge of the design sensitivities over the optimised domain. This makes the power of the method. Its SIMP (Solid Isotropic Material with penalisation) variation is the most common techniques used to find optimal material distribution. This method was proposed by Bendsoe [5] and Rozvany *et al.* [6].

The idea is to divide the domain into finite elements that are filled or not with an isotropic material. To reflect this, a density ρ_e is associated to each element:

$$\rho_e = \begin{cases} 1 \text{ when the element is filled with material} \\ 0 \text{ when the element is empty} \end{cases}$$

But the problem is binary. That is why a continuous relative distribution of density is introduced. Each element can have a density between a certain minimum value and one. This leads to porous elements, i.e. elements with intermediate values of the density. Due to the continuous variation of the density, if the Young Modulus is for example characterized inside a given problem, then this quantity varies also continuously. This is expressed by the following equation:

$$E(\rho_e) = \rho_e^p E_o$$

where p is a penalty factor and E_o is the Young Modulus of the isotropic material. The variation of the Young Modulus with the density is illustrated in Fig. 2.2. It can be pointed out that the increase of the penalty factor makes drop the contribution of the porous elements.
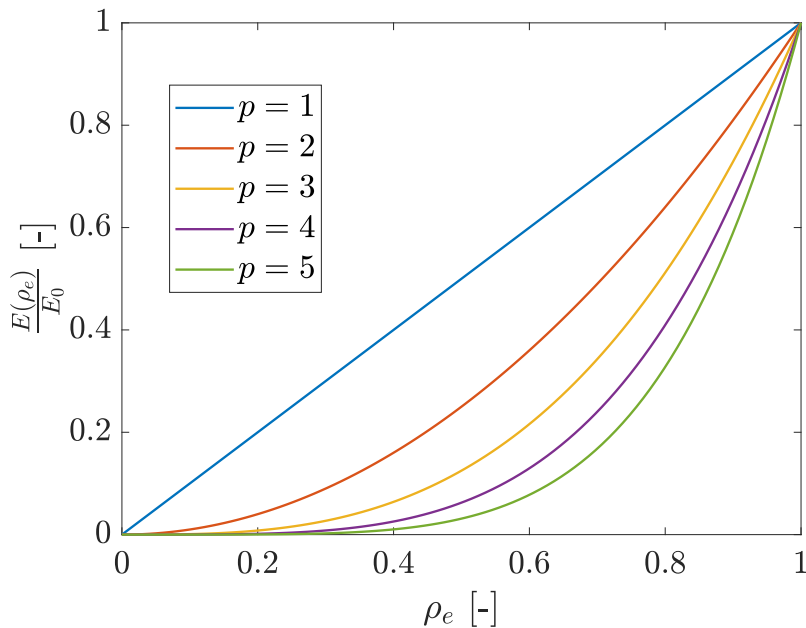
Figure 2.2: Relative Young modulus variation with the density for increasing value of the penalisation factor p.

The most common application of the density-based approach in solid mechanics is the maximisation of stiffness, i.e. minimisation of the compliance C:

$$\begin{cases} \min C(\rho) = \mathbf{u}^T \mathbf{F}(\rho) \\ \text{s.t. } \mathbf{K}(\rho)\mathbf{u} = \mathbf{F} \end{cases} \tag{2.1}$$

where C is the compliance, **u** is the displacement vector, **F** is the vector of forces applied on the structure, and **K** is the stiffness matrix. In order to find the optimal material distribution, the optimiser needs the sensitivities of the objective function. These correspond to the derivatives of the objective function C with respect to the design variables which are the densities associated to the elements.

This method will be used in the scope of this thesis. The specification to a CHT problem will be done later.

2.2 General procedure of a topology optimisation problem resolution

Now that the main GB methods of topology optimisation are known, the purpose is to know how a general problem of topology optimisation is solved. First of all, the computation of the gradient will be explained. Then, the succeeding goal will be the explanation of how the sensitivities are used in order to update the design variables.

In the upcoming subsections, the efficient approach of using the adjoint approach for computing the sensitivities will be explained. Then, the update of the design variables with the method of moving asymptotes (MMA) combined with the optimality criteria will be described.

2.2.1 Adjoint approach for computing the sensitivities

There exist several ways of computing the gradient information of an objective function. This could be done thanks to the finite differentiation (FD) or the direct differentiation (DD). The issue is that an optimisation problem is often constrained by partial differential equations (PDE's) that have to be satisfied. For example, in the FD method, each of the design variables is perturbed by an infinitesimally small quantity, and then the variation of the objective function divided by this small perturbation gives the sensitivity with respect to the considered design variable. The complexity is the resolution of the PDE's for each perturbed design variable, which is very costly in topology optimisation due to the high number of design variables. A more cost-effective method is thus needed in order to compute the gradient.

The adjoint method is an efficient approach that prevents the resolution of the PDE's each time a component of the gradient is computed. To prove the competence of the approach, a classical optimisation problem of the following form is considered

$$\begin{cases} \min J(U, x) \\ \text{s.t. } R(U, x) = 0 \end{cases} \tag{2.2}$$

with $J(U, x)$ $(\mathbb{R}^{n_U} \times \mathbb{R}^{n_x} \to \mathbb{R})$ is an objective function to be minimised, x corresponds to the design variables, U is the set of state variables, with the relationship $R(U, x) = 0$ for a

function R ($\mathbb{R}^{n_U} \times \mathbb{R}^{n_x} \to \mathbb{R}^{n_U}$) to be satisfied. The methodology employed to explain the adjoint approach is the same as in [18].

The goal is to compute the total variation, or the sensitivity, of the objective function with respect to the design variables. The relationship $R(U, x) = 0$ is generally complicated to solve. For given given values of the design variables, the state variables U are obtained by the resolution of $R(U, x) = 0$. When employing for FD or DD methods, then n_x finite differences must be computed, which means that $R(U, x) = 0$ must be solved n_x times. For a topology optimisation problem, this becomes rapidly expensive due to the presence of a lot of design variables, i.e. because of the high value of n_x. With the adjoint approach, the computational cost is significantly decreased compared to the FD (or DD) approach since the adjoint method introduces a set of equations to be solved only once together with the relationship $R(U, x) = 0$ that is then solved also only one time in the scope of one optimisation cycle.

Considering the simple case of an objective function directly depending on the state variables, then $J \equiv J(U)$ where the state variables U depend on the design variables x. The aim is to compute cost-effectively dJ/dx defined as

$$\frac{dJ}{dx} = \frac{dJ(U(x))}{dx} = \frac{\partial J}{\partial U}\frac{dU}{dx} \tag{2.3}$$

and

$$R(U, x) = 0 \tag{2.4}$$

must be satisfied everywhere. Eq. 2.4 implies that $dR/dx = 0$ because $R = 0$ for each of the design variables.

The adjoint approach makes use of the adjoint variables through the construction of the Lagrangian given by the following equation

$$\mathcal{L}(U, x, \xi) \equiv J(U) + \xi^T R(U, x) \tag{2.5}$$

where ξ is the vector of Lagrange multipliers (or adjoint variables).

As $R(U, x) = 0$ for each x, $\mathcal{L}(U, x, \xi) \equiv J(U)$ and ξ can be chosen freely. With this new variant of the objective function $J(U)$, Eq. 2.3 becomes

$$\begin{aligned}
\frac{dJ}{dx} = \frac{d\mathcal{L}}{dx} &= \frac{\partial J(U)}{\partial U}\frac{dU}{dx} + \frac{d\xi^T}{dx}R + \xi^T\left(\frac{\partial R}{\partial U}\frac{dU}{dx} + \frac{\partial R}{\partial U}\right) \\
&= \frac{\partial J}{\partial U}\frac{dU}{dx} + \xi^T\left(\frac{\partial R}{\partial U}\frac{dU}{dx} + \frac{\partial R}{\partial U}\right) \\
&= \left(\frac{\partial J}{\partial U} + \xi^T\frac{\partial R}{\partial U}\right)\frac{dU}{dx} + \xi^T\frac{\partial R}{\partial U}.
\end{aligned} \tag{2.6}$$

If ξ is chosen such that

$$\frac{\partial R}{\partial U}^T \xi = -\frac{\partial J}{\partial U}^T \tag{2.7}$$

10

then the expensive computation of $\frac{dU}{dx}$ is avoided, and the final expression of the sensitivity of the objective function with respect to the design variables is then given by

$$\frac{dJ}{dx} = \xi^T \frac{\partial R}{\partial U}. \tag{2.8}$$

Eq. 2.7 represents the adjoint equation that has to be solved only once in order to derive the final sensitivity of J. Note that once the adjoint variables are obtained thanks to Eq. 2.7, then dJ/dx is obtained with the vector dot product between the adjoint variables ξ and $\partial R/\partial U$ at a negligible cost compared to solving the equation $R(U, x) = 0$ n_x times.

Now that the approach used in order to compute the sensitivities is known, the following step is to introduce how the design variables are updated. This is detailed in the upcoming section.

2.2.2 Method of moving asymptotes (MMA) and optimality criteria

Once the sensitivities are computed, the design variables are updated using the Method of Moving Asymptotes (MMA) or its Globally Convergent version (GCMMA). (GC)MMA is a method that can handle easily the bounds imposed on the design variables and other types of constraints. These methods were introduced by Krister Svanberg [19]. The explanation of the method is the same as in [19].

A standard topology optimisation problem has the following form

$$\begin{cases} \min \ f_0(\mathbf{x}) \\ \text{s.t. } f_i(\mathbf{x}) \leqslant 0 & i = 1, ..., m \\ x_j^{min} \leqslant x_j \leqslant x_j^{max} & j = 1, ..., n \end{cases} \tag{2.9}$$

where $f_0(\mathbf{x})$ is the objective function quantifying the performance of the system, $\mathbf{x}$ is the vector of dimension j comprising the design variables, $f_i(\mathbf{x})$ $(i = 1, ..., m)$ are the functions of the constraints of the problem that have to be verified, and x_j^{min} (resp. x_j^{max}) is the lower (resp. upper) bound of the design variables.

The idea of MMA is to generate a convex approximation of a given problem. Having a convex problem helps in fact to solve it more easily since a convex problem has a unique solution. This convex approximation gives rise to a sub-problem. Once this convex sub-problem is solved, its solution is a new iterated point around which a new convex approximation is done, and thus gives a new sub-problem that is solved, and its solution is again a new iterated point. The process continues until the optimal solution is reached. Its globally convergent version (GCMMA) is also based on the same idea but is used as a kind of "line search".

So in order to update the design field, a convex approximation is done in each optimisation cycle using MMA. Then, this sub-problem is solved using the Karush-Kuhn-Tucker (KKT)

conditions leading to a whole system of equations whose solution is obtained with the Newton method. More details about these conditions will be given in the following subsection.

Whatever the considered optimisation problem, it will be based on the following form

$$
\begin{cases}
\min \ f_0(\mathbf{x}) + a_0 z + \sum_{i=1}^{m} \left(c_i y_i + \frac{1}{2} d_i y_i^2 \right) \\
\text{s.t. } f_i(\mathbf{x}) - a_i z - y_i \leqslant 0 \quad i = 1, ..., m \\
\qquad x_j^{\min} \leqslant x_j \leqslant x_j^{\max} \quad j = 1, ..., n \\
\qquad \mathbf{y} \geqslant 0, \ z \geqslant 0
\end{cases}
\tag{2.10}
$$

where x_j are the "natural" design variables, n is their total number, y_j $(i = 1, ..., m)$ are "artificial" optimisation variables, and the variable $z \in \mathbb{R}$. The functions f_0, f_1, ..., f_m are continuously differentiable real valued functions, $x_j^{\min}$ and $x_j^{\max}$ correspond respectively to the lower and upper bounds of the design variables x_j.
The coefficients must be such that:

- a_0, a_i, c_i, and d_i are real numbers with $a_0 > 0$, $a_i \geqslant 0$, $c_i \geqslant 0$, $d_i \geqslant 0$, and $c_i + d_i > 0$ for $i = 1, ..., m$;

- $a_i c_i > a_0$ for $i = 1, ..., m$ with $a_i > 0$.

The reason why the problems will be based on problems of type (2.10) is that it has always feasible solutions, and also at least one optimal solution. The proof is given in [19].

In order to make correspond problem (2.9) to (2.10), the parameters of (2.10) should be chosen as follows:

- $a_i = 0$ for each i, which leads to $z = 0$ in any optimal solution of (2.10);

- $d_i = 0$ for each i, and c_i is a large number such that y_i is enforced to be equal to zero in any optimal solution of (2.10).

Proceeding this way, the optimal solution of (2.10) will then become the optimal solution of (2.9).

Then it comes to the definition of the approximating sub-problem in each optimisation cycle. At a given iterated point $\mathbf{x}^k$ corresponding to the $k - th$ optimisation cycle, the functions $f_i(\mathbf{x})$ for $i = 0, 1, ..., m$ are replaced by convex approximations $g_i^k(\mathbf{x})$. In order to construct these approximating functions, the gradient information of the functions $f_i(\mathbf{x})$ at the current iteration point $\mathbf{x}^k$ is needed. There are also other parameters that intervene in the definition of the convex problem. These are the upper and lower asymptotes u_j^k and l_j^k which can be updated in each optimisation cycle. That is why we call them moving asymptotes. Based on all of this information, the different functions are then approximated as

$$
g_i^k(\mathbf{x}) = \sum_{j=1}^{n} \left(\frac{p_{ij}^k}{u_j^k - x_j} + \frac{q_{ij}^k}{x_j - l_j^k} \right) + r_i^k \quad i = 0, 1, ..., m
\tag{2.11}
$$

where

$$p_{ij}^k = (u_j^k - x_j^k)^2 \left(\frac{\partial f_i}{\partial x_j}(\mathbf{x}^k) \right)^+, \tag{2.12}$$

$$q_{ij}^k = (x_j^k - l_j^k)^2 \left(\frac{\partial f_i}{\partial x_j}(\mathbf{x}^k) \right)^-, \tag{2.13}$$

$$r_i^k = f_i(\mathbf{x}^k) - \sum_{j=1}^n \left(\frac{p_{ij}^k}{u_j^k - x_j} + \frac{q_{ij}^k}{x_j - l_j^k} \right), \tag{2.14}$$

$$\tag{2.15}$$

with $\left(\frac{\partial f_i}{\partial x_j}(\mathbf{x}^k) \right)^+ = \max \left\{ 0, \frac{\partial f_i}{\partial x_j}(\mathbf{x}^k) \right\}$, and $\left(\frac{\partial f_i}{\partial x_j}(\mathbf{x}^k) \right)^- = \max \left\{ 0, -\frac{\partial f_i}{\partial x_j}(\mathbf{x}^k) \right\}$.

The MMA sub-problem is then defined as

$$\begin{cases}
\min g_0^k(\mathbf{x}) + z + \sum_{i=1}^m \left(c_i y_i + \frac{1}{2} d_i y_i^2 \right) \\
\text{s.t. } g_i^k(\mathbf{x}) - a_i z - y_i \leqslant 0 & i = 1, ..., m \\
\alpha_j^k \leqslant x_j \leqslant \beta_j^k & j = 1, ..., n \\
y_i \geqslant 0 & i = 1, ..., m \\
z \geqslant 0
\end{cases} \tag{2.16}$$

where the bounds α_j^k and β_j^k are called moving limits and are updated in each optimisation cycle as

$$\alpha_j^k = \max \left\{ x_j^{\min}; x_j^k - 0.5(x_j^{\max} - x_j^{\min}) \right\}, \tag{2.17}$$

$$\beta_j^k = \min \left\{ x_j^{\max}; x_j^k + 0.5(x_j^{\max} - x_j^{\min}) \right\}. \tag{2.18}$$

Concerning the update of the moving asymptotes, this is done as follows

- k = 1 and k = 2:

$$l_j^k = x_j^k - 0.5(x_j^{\max} - x_j^{\min});$$
$$u_j^k = x_j^k + 0.5(x_j^{\max} - x_j^{\min}).$$

- k ⩾ 3:

$$l_j^k = x_j^k - \gamma_j^k(x_j^{k-1} - l_j^{k-1});$$
$$u_j^k = x_j^k + \gamma_j^k(x_j^{k-1} - l_j^{k-1}).$$

where γ_j^k takes by default the following values

$$\gamma_j^k = \begin{cases}
0.7 & \text{if } (x_j^k - x_j^{k-1})(x_j^{k-1} - x_j^{k-2}) < 0 \\
1.2 & \text{if } (x_j^k - x_j^{k-1})(x_j^{k-1} - x_j^{k-2}) > 0 \\
1 & \text{if } (x_j^k - x_j^{k-1})(x_j^{k-1} - x_j^{k-2}) = 0
\end{cases} \tag{2.19}$$

The value of the update parameter γ_j^k is lower than unity when there is oscillation in the optimisation process. This allows to stabilise the process.

An example of how MMA treats a problem is illustrated in Fig. 2.3 for the approximation of the strain energy in a two-ply symmetric laminate subject to shear load and torsion. In this case, at a given optimisation cycle k, the approximation being done at the black dotted point, only the lower asymptote is activated due to the negative value of the first order derivative. The role of the move limit is also noted. It prevents in fact the iterated point to not go far away from the desired solution.
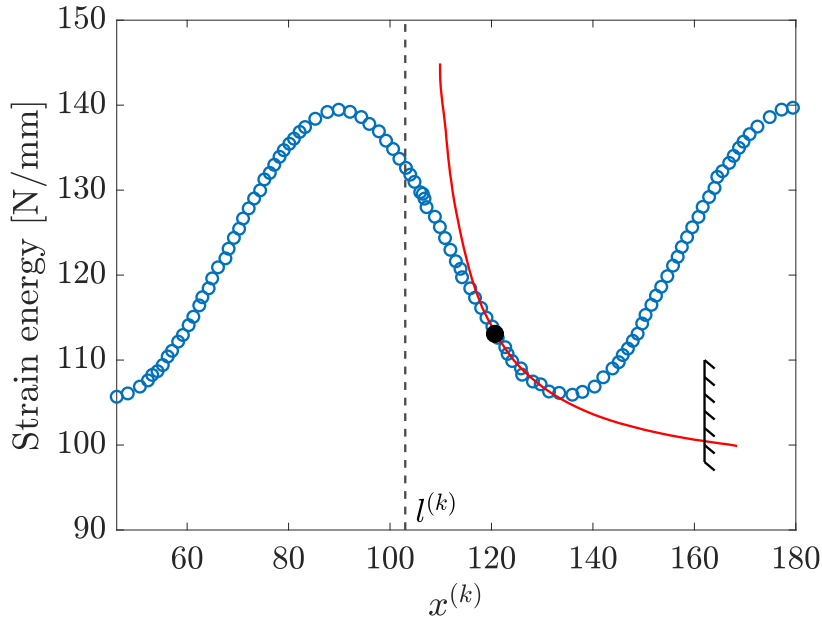
Figure 2.3: Approximation with MMA of the strain energy in a two-ply symmetric laminate subject to shear load and torsion (only the lower asymptote and the upper moving limit are activated in this case) [2].

2.2.2.1 Globally Convergent Method of Moving Asymptotes (GCMMA)

The Globally Convergent version of MMA exists also. This plays the role of some kind of "line search". As a matter of fact, it may happen that the value of the approximating function g_i^k evaluated at the new iterated point $\mathbf{x}^{k+1}$ is lower than the value of the original function $f_i(\mathbf{x})$ evaluated at $\mathbf{x}^{k+1}$. Therefore, if GCMMA is used, inner iterations are going to be generated. The condition to have no need of inner iterations is thus

$$g_i^k(\mathbf{x}^{k+1}) \geqslant f_i(\mathbf{x}^{k+1}) \tag{2.20}$$

If the condition 2.20 is not satisfied, then inner iterations are created. These are denoted by the symbol ν. The solution obtained by the outer iteration k becomes

$$\mathbf{x}^{k+1} = \mathbf{x}^{k,1}$$

with the number 1 corresponding to the first inner iteration. Then, from this point $\mathbf{x}^{k,1}$, a new sub-problem is created and this new sub-problem is more conservative than the sub-problem of the outer iteration. The problems generated in the inner iterations are similar to the one of the outer iteration, but the inner sub-problems are much conservative thanks to an introduction of a parameter $\rho_i^{k,\nu}$ associated to its corresponding function $f_i(\mathbf{x})$. The approximating functions in GCMMA are given by

$$g_i^k(\mathbf{x}) = \sum_{j=1}^{n} \left(\frac{p_{ij}^k}{u_j^k - x_j} + \frac{q_{ij}^k}{x_j - l_j^k} \right) + r_i^k \quad i = 0, 1, ..., m \tag{2.21}$$

where

$$p_{ij}^k = (u_j^k - x_j^k)^2 \left[\left(\frac{\partial f_i}{\partial x_j}(\mathbf{x}^k) \right)^+ + \frac{\rho_i^{k,\nu}}{x_j^{\max} - x_j^{\min}} \right], \tag{2.22}$$

$$q_{ij}^k = (x_j^k - l_j^k)^2 \left[\left(\frac{\partial f_i}{\partial x_j}(\mathbf{x}^k) \right)^- + \frac{\rho_i^{k,\nu}}{x_j^{\max} - x_j^{\min}} \right], \tag{2.23}$$

$$r_i^k = f_i(\mathbf{x}^k) - \sum_{j=1}^{n} \left(\frac{p_{ij}^k}{u_j^k - x_j} + \frac{q_{ij}^k}{x_j - l_j^k} \right). \tag{2.24}$$

The parameter $\rho_i^{k,\nu}$ controls the conservative form of the approximating functions g_i^k. It is updated as follows

- if $g_i^{k-1,\nu}(\mathbf{x}^k) < f_i(\mathbf{x}^k)$ then $\rho_i^{k,\nu}$ is increased in order to have a more conservative approximating sub-problem;

- if $g_i^{k-1,\nu}(\mathbf{x}^k) \geqslant f_i(\mathbf{x}^k)$ then $\rho_i^{k,\nu}$ remains the same.

The strategy employed in GCMMA is showed in Fig. 2.4 where for increasing values of the parameter $\rho^{k,\nu}$, the approximations get more conservative.

The update rules for the moving limits and for the asymptotes are the same as for MMA. The computation of the gradients of the functions $f_i(\mathbf{x})$ is done only one time and this happens in the outer iteration k. In the inner iterations, this operation does not take place.
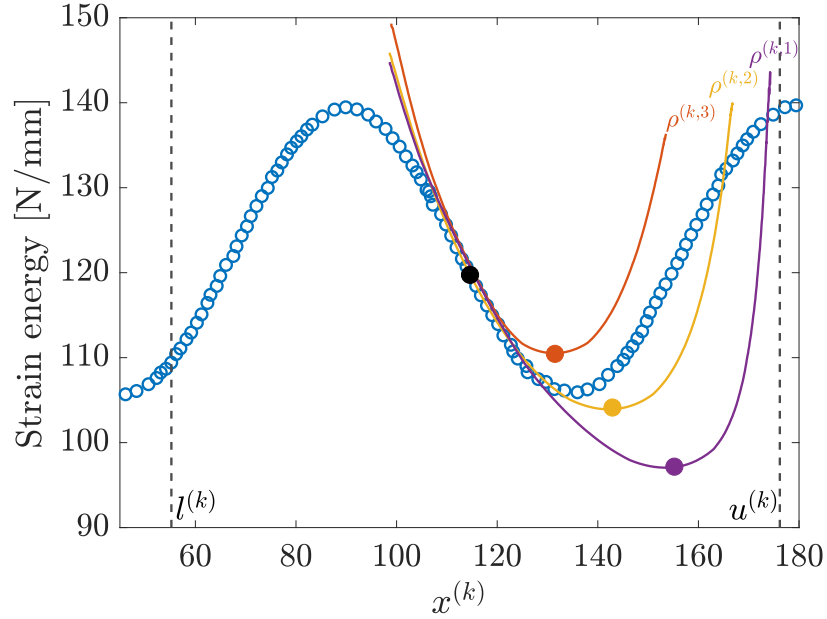
Figure 2.4: Approximation with GCMMA of the strain energy in a two-ply symmetric laminate subject to shear load and torsion; influence of the parameter $\rho^{k,\nu}$ ($\rho^{k,3} > \rho^{k,2} > \rho^{k,1}$) [2].

2.2.3 Optimality conditions for the sub-problems

The sub-problems being convex, the KKT conditions are necessary and sufficient optimality conditions. The methodology in order to derive these conditions is the same as in [19]. In order to derive these conditions, the Lagrangian function corresponding to the problem (2.16) is constructed

$$
\begin{aligned}
\mathcal{L}(\mathbf{x}, \mathbf{y}, z) &= g_0^k(\mathbf{x}) + z + \sum_{i=1}^{m} \left(c_i y_i + \frac{1}{2} d_i y_i^2 \right) + \sum_{i=1}^{m} \chi_i (g_i^k(\mathbf{x}) - a_i z - y_y - r_i^k) \\
&+ \sum_{j=1}^{n} (\xi_j(\alpha_j - x_j) + \eta_j(x_j - \beta_j)) - \sum_{i=1}^{m} \mu_i y_i - \zeta z
\end{aligned}
\tag{2.25}
$$

where $\chi = (\chi_1, ..., \chi_m)^T$, $\xi = (\xi_1, ..., \xi_n)^T$, $\eta = (\eta_1, ..., \eta_n)^T$, $\mu = (\mu_1, ..., \mu_m)$, and ζ are non-negative Lagrange multipliers. These are also called the dual variables.

Taking into consideration the following equality

$$
\psi(\mathbf{x}, \chi) = g_0^k(\mathbf{x}) + \sum_{i=1}^{m} \chi_i g_i^k(\mathbf{x}) = \sum_{j=1}^{n} \left(\frac{p_j^k(\chi)}{u_j^k - x_j} + \frac{q_j^k(\chi)}{x_j - l_j^k} \right)
\tag{2.26}
$$

where $p_j^k(\chi) = p_{0j}^k + \sum_{i=1}^{m} \chi_i p_{ij}^k$ and $q_j^k(\chi) = q_{0j}^k + \sum_{i=1}^{m} \chi_i q_{ij}^k$, the Lagrangian function becomes

$$\mathcal{L}(\mathbf{x}, \mathbf{y}, z) = \psi(\mathbf{x}, \chi) + \sum_{j=1}^{n}(\xi_j(\alpha_j - x_j) + \eta_j(x_j - \beta_j)) + (1 - \zeta)z$$

$$+ \sum_{i=1}^{m}\left(c_i y_i + \frac{1}{2}d_i y_i^2 - \chi_i a_i z - \chi_i y_i - \chi_i r_i^k - \mu_i y_i\right) \tag{2.27}$$

and the KKT conditions are written as

$$\frac{\partial \psi}{\partial x_j} - \xi_j + \eta_j = 0, \quad j = 1, ..., n \tag{2.28}$$

$$c_i + d_i y_i - \chi_i - \mu_i = 0, \quad i = 1, .., m \tag{2.29}$$

$$1 - \zeta - \chi^T a = 0, \tag{2.30}$$

$$g_i^k(\mathbf{x}) - a_i z - y_i - r_i^k \leqslant 0, \quad i = 1, ..., m \tag{2.31}$$

$$\chi_i(g_i^k(\mathbf{x}) - a_i z - y_i - r_i^k) = 0, \quad i = 1, .., m \tag{2.32}$$

$$\xi_j(\alpha_j - x_j) = 0, \quad j = 1, ..., n \tag{2.33}$$

$$\eta_j(x_j - \beta_j) = 0, \quad j = 1, .., n \tag{2.34}$$

$$-\mu_i y_i = 0, \quad i = 1, .., m \tag{2.35}$$

$$-\zeta z = 0, \tag{2.36}$$

$$\alpha_j - x_j \leqslant 0 \text{ and } x_j - \beta_j \leqslant 0, \quad j = 1, ..., n \tag{2.37}$$

$$-z \leqslant 0 \text{ and } -y_i \leqslant 0, \quad i = 1, ..., m \tag{2.38}$$

$$\xi_j \geqslant 0 \text{ and } \eta_j \geqslant 0, \quad j = 1, ..., m \tag{2.39}$$

$$\zeta \geqslant 0 \text{ and } \mu_i \geqslant 0, \quad i = 1, ..., m \tag{2.40}$$

$$\chi_i \geqslant 0, \quad i = 1, ..., m \tag{2.41}$$

where

$$\frac{\partial \psi}{\partial x_j} = \frac{p_j^k(\chi)}{(u_j^k - x_j)^2} - \frac{q_j(\chi)}{(x_j - l_j^k)^2} \quad \text{and} \quad \chi^T a = \sum_{i=1}^{m}\chi_i a_i.$$

Eq. 2.28 to Eq. 2.30 correspond the stationarity of the Lagrangian function, which constitute the first requirement of the KKT conditions. Then, Eq. 2.31, Eq. 2.37, and Eq. 2.38 represent the constraints of the problem which have to be verified. Eq. 2.32 to Eq. 2.36 represent the complementary slackness equations, which stand for the third set of KKT conditions. And finally, Eq. 2.39 to Eq. 2.41 denote the dual feasibility, which states that the Lagrangian multipliers corresponding to inequality constraints must be non-negative.

In order to solve this system of equations, and thus to find the direction in which the optimisation path should go, the Newton method is used. Once the direction is found, a line search is applied in order to find the optimal step length for the optimiser to move along the direction. More details are given in [19].

2.3 Topology optimisation in fluid flows

The goal is now to learn how of topology optimisation is used in fluid-based problems which constitute the main application of topology optimisation in this thesis. For a given design domain, the question is where the fluid should flow in order to minimise the objective function while satisfying the constraints imposed on the problem. When topology optimisation is applied to fluid flow problems, the flow must be modeled by at least one governing equation. These equations could be for instance based on the Darcy flow, modeling the flow of an incompressible fluid in a porous medium, or the Stokes and Navier-Stokes equations.

For the general case of an incompressible Newtonian fluid, the Navier-Stokes equations are written as

$$\nabla \cdot \mathbf{V} = 0$$
$$\frac{\partial \mathbf{V}}{\partial t} + (\mathbf{V} \cdot \nabla)\mathbf{V} - \nu\nabla^2\mathbf{V} = -\frac{1}{\rho}\nabla p + \mathbf{g}$$

where $\mathbf{V}$ [m/s] is the velocity vector, ρ [kg/m^3] the density of the fluid, ν the kinematic viscosity of the fluid [m^2/s], p the fluid pressure [Pa], and $\mathbf{g}$ the body force per unit volume [N/m^3] (the gravity force for instance). The first equation represents the continuity equation (or mass conservation) and the second equation corresponds to the momentum equation. The Stokes equations are a linearisation of the Navier-Stokes equations. A Stoke's flow consists in a viscous fluid moving inside a narrow passage, leading to high viscous effects getting over the advective inertial forces. This type of flow happens thus at very low Reynolds number.

Besides the equations governing the flow, additional equations modeling other physics can be included. These could be for instance the equations governing the temperature, the structural mechanics, and so on. Thanks to this aspect, multi-physics topology optimisation can be achieved. There are various domains in which fluid-flow topology optimisation is combined with other physics. These are for instance problems including CHT, convection, fluid structure interaction, micro-structure, and homegenisation.

In the framework of purely fluid-based, the first work on steady-state topology-optimisation problem was published by Borrvall and Petersson in 2003 [20]. They have introduced topology optimisation of Stokes (or creeping) flow. They have based their work on the general form of the Stokes equation [21] which includes the term $\lambda I - \nu\Delta$, with λ [s^{-1}] being the inverse permeability, and ν [m^2/s] the viscosity. When $\lambda = 0$, one recovers Stokes flow with viscosity ν, and when $\nu = 0$, one recovers Darcy flow that dictates the flow in a porous medium with permeability λ^{-1}. The idea of Borrvall and Petersson was to modify this general form of the Stokes equation in such a way that the viscosity was kept constant, and the inverse permeability was tuned in order to give a very small permeability λ^{-1} at non-fluid places, and very large when the Stokes flow takes place. The role of λ is to play the role of a penalty factor that blocks the flow, i.e. makes the velocity tend to zero at non-fluid places. The objective of Borrvall and Petersson in this first study was to generate fluid topologies that minimises the dissipated energy using inhomogeneous porous materials with a spatially varying Darcy

permeability tensor. Later, this was generalized to the limiting cases of a porous material, i.e. pure solid and pure fluid parts in the domain, by Evgrafov [22]. The work of Borrvall and Petersson was extended to Navier-Stokes flow by Gersborg-Hansen *et al.* [23]. They have noticed some coincidence between their equations and the ones of a Brinkman-type Darcy's law modelling the flow inside a porous medium. This led to the construction of equations that include a penalisation term composed of a term proportional to the inverse of the Darcy number and the velocity. This permits to model arbitrarily complex solid obstacles in the flow as porous media with porosity and permeability approaching zero. So, in order to take into account the presence of material in the fluid problem, a penalisation term is added to the flow equations. Topology optimisation in fluid flows indeed makes use of a porosity-dependent term in the flow equations. Olesen *et al* [24] proposed topology optimisation for steady-state Navier-Stokes flow using this fictitious porous media approach. In their work, the presence of solid material inside the domain has been taken into account through a "friction" force **f** which is proportional to the flow velocity and is written as

$$\mathbf{f} = -\lambda \mathbf{v}.$$

Including this force into NSE, the governing equations for a steady state incompressible flow take the following form

$$\frac{\partial v_j}{\partial x_j} = 0$$

$$v_j \frac{\partial v_i}{\partial x_j} - \frac{\tau_{ij}}{\partial x_j} + \frac{\partial p}{\partial x_i} + \lambda v_i = 0$$

where $\tau_{ij} = \nu \left(\frac{\partial v_i}{\partial x_j} + \frac{\partial v_j}{\partial x_i} \right)$ [m^2/s^2] is the shear stress tensor, v_j [m/s] are the velocity components, p [Pa/(kg/m^3)] is the pressure divided by the density, and ν [m^2/s] is the kinematic viscosity. In order to control the local permeability of the design domain, they have used a design variable γ [-] which varies between 0 and 1. $\gamma = 0$ corresponds to solid material, and $\gamma = 1$ to the absence of material. Note that the design variable can vary continuously between zero and one assuming a porous and permeable material distribution. This approach allows to have a smooth problem that can be solved with efficient methods that require the sensitivities with respect to the design variable using (GC)MMA. Ensuing the work of Borrvall and Petersson, a relation between the local inverse permeability λ and the design varaible γ using a convex interpolation is introduced

$$\lambda(\gamma) \equiv \lambda_{\min} + (\lambda_{\max} - \lambda_{\min}) \frac{q(1-\gamma)}{q+\gamma}$$

with q [-] being a positive parameter that controls the shape of $\lambda(\gamma)$. In order to have ideal impermeable solid walls, $\lambda_{\max}$ must tend to infinity but for numerical reasons this cannot happen. $\lambda_{\max}$ is chosen based on the Darcy number. This will be explained later. Concerning the minimum value of λ, following [20], this has been set to zero. In areas where γ is close to zero, the inverse permeability λ is high, which means that the permeability λ^{-1} is very low, and thus leading to a zone where no flow can take place. This can be easily understood by considering the momentum equations here above. For large values of λ which happen for γ

close to zero, in order to verify the equation of momentum, the flow velocity must tend to zero. In contrast to that phenomenon, when γ is close to one, λ is close to zero, and thus the permeability λ^{-1} is high. This allows the fluid to flow and the momentum equation gets towards the classical momentum equation of Navier-Stokes.

Guest and Prévost [25] have then suggested a hybrid approach in which the solid regions correspond to areas with Darcy flow of low permeability, and the fluid around them are subjected to Stokes flow. To do so, they have used a Darcy-Stokes finite element interpolation. Othmer derived a continous adjoint formulation for shape and topology optimisation of Navier-Stokes flow [26]. This was done in the scope of the finite volume solver OpenFOAM. The adjoint formulation is important in the framework of fluid-based TO for the computation of the sensitivities with respect to the design variables. As the number of design variables can be in fact very high, computing directly the sensitivities of the objective function with respect to the design variables costs a lot. The adjoint method permits to compute the gradient of the objective function at a cost that does not depend on the total number of design variables.

Topology optimisation for unsteady flow has also been done in the past. One of the first applications was done by Kreiss *et al.* [27] who utilised density-based topology optimisation in order to enhance the design of a diffuser and oscillating flow manifold using a discrete transient adjoint formulation. After that, Deng *et al.* [28] applied density-based topology optimisation for unsteady flow using continuous transient adjoint formulation.

Concerning fluid topology optimisation in which turbulence is taken into account, these are limited to steady-state time-averaged turbulence although turbulence is a time dependent phenomenon. The approximation is done thanks to the Reynolds-Averaged Navier-Stokes (RANS) equations.
Othmer [26] included turbulence in his model, but the variation of the turbulent viscosity with the design variable was not taken into account by making the "frozen turbulence" assumption. Kontoleontos *et al.* [29] performed for the first time topology optimisation including the turbulence sensitivity using the Spalart-Allmaras turbulence model in their continuous adjoint formulation. Other examples of turbulent flow topology optimisation can be found in [30], [31], and [32].

Topology optimisation has also been used in CHT problems. This type of heat transfer is about the coupled one between a solid and the surrounding fluid. Forced convection and natural convection are the mechanisms of CHT including fluid motion. Forced convection takes place when the flow is activated by a pump, a fan, or a pressure-gradient, while natural convection is due to temperature differences giving density variations.
Many works have emerged in the field of forced convection. The first ones are the studies presented by Dede [33, 34] and Yoon [35]. After that, several applications have then appeared for forced convection. Dede has again used topology optimisation for electronics cooling [34], Matsumori *et al.* [36] optimised topologically the heat sinks under forced convection with a constant input power. Then, Mark *et al.* [37] considered a multi-objective function including both thermal and fluid objectives in their optimisation problem. Zhang and Gao [38] have also optimised with a density-based approach thermal devices with non-Newtonian

fluid flows. Topology optimisation has also been used in order to enhance heat exchangers with two separate fluids and solids, as Tawk *et al.* did [39]. Concerning natural convection, Alexandersen *et al.* [40] are the first ones to have presented a work about it with a density-based approach in order to optimise heat sinks and buoyancy-driven micro-pumps. Alexandersen *et al.* [41] have then applied their method to the optimisation of passive coolers for light-emitting diode (LED) lamps. Lazarov *et al.* [42] validated then the designs of [41] using additive manufacturing in aluminium. They have proven the agreement of the designs with numerical results.

Topology optimisation can also be used in the framework of fluid-structure interaction (FSI) problems. Three main types of FSI topology optimisation exist. These are called wet, dry, and wet and dry design modifications. A wet modification corresponds to only the internal change of the design without affecting the solid-fluid interface. The dry design modification changes only the solid-fluid interface. Finally, the wet and dry optimisation includes both wet and dry design modifications. The first work on FSI topology optimisation was proposed by Yoon [43] who had used a density-based approach.

Now that a general review of the applications in which fluid based topology optimisation has been used, the formulation of the method topology optimisation will be done for CHT problems in the following section.

2.3.1 Problem formulation of conjugate heat transfer topology optimisation with one fluid

The aim is now to appropriate the concept of topology optimisation for the enhancement of structures involving conjugate heat transfer (CHT). CHT consists in the combination of conduction in a solid together with convection through a fluid that is in contact with this solid. In the current work, CHT problems are handled with only one fluid.

The current technique used in order to approach topology optimisation with one fluid is density (or porosity) based. When dealing with density-based topology optimisation in fluid problems, the design variable is noted α [-] and corresponds to the amount or volume fraction of material present in each control volume. Then, topology optimisation aims at finding the optimal material distribution by tuning α in each control volume in order to minimise a certain objective function while verifying given constraints. Parts of the domain which are counterproductive with respect to an objective function J, which represents the performance of a system, are solidified, while the other ones are the fluid zones in which the flow takes place. If α is equal to one at a given cell, this corresponds to a solid cell, while α equal to zero represents a void cell, i.e. where the fluid can flow. The goal is to have a discrete solution with $0/1$ distribution of the design field α. However, the problem must be relaxed in order to be able to use gradient based methods when solving the problem. Therefore, α is allowed to take intermediate values between zero and one, which represent respectively the lower and upper bounds of the design variables. Regions with intermediate values of density are called grey regions which are complicated to interpret. In order to have a final discrete distribution with well defined solid and fluid regions, some post-processing must be applied to the design field.

New developments related to this treatment of the design field are also included. These are namely called the regularisation and projection. All of these will be explained in details later.

The CHT topology optimisation problem can be formulated as follows

$$
\begin{cases}
\min_{\alpha} & J(\alpha, \mathbf{U}) \\
\text{s.t.} & g_i(\alpha) \leqslant 0 \qquad i = 1, ..., m \\
& 0 \leqslant \alpha_j \leqslant 1 \quad j = 1, ..., N \\
& \mathbf{R}(\alpha, \mathbf{U}) = 0
\end{cases}
\tag{2.42}
$$

where J is the objective function, $g_i(\alpha)$ are the constraints, m is the total number of constraints, N is the total number of design variables which is equal to the number of cells when using finite volume discretisation, $\mathbf{R}(\alpha, \mathbf{U})$ represents the equations modelling the flow that have to be verified, and $\mathbf{U}$ is the vector of the state variables. In a fluid-flow problem combined with heat transfer, these are commonly the velocity, the pressure, the temperature, and the turbulent variable which is the turbulent viscosity. The state equations are dictated hereafter.

Navier-Stokes equations

The flow is modelled thanks to the the steady-state Navier-Stokes equations for an incompressible fluid. Taking into account the presence of the material using the penalisation term that acts as a resistance force that "freezes" the flow in solid areas, i.e. including the Brinkmann penalisation term, the equations are written as follow

$$
R^p = \frac{\partial v_j}{\partial x_j} = 0
\tag{2.43}
$$

$$
R_i^v = v_j \frac{\partial v_i}{\partial x_j} - \frac{\partial}{\partial x_j} \left[(\nu + \nu_t) \left(\frac{\partial v_i}{\partial x_j} + \frac{\partial v_j}{\partial x_i} \right) \right] + \frac{\partial p}{\partial x_i} + \lambda(\beta) v_i = 0
\tag{2.44}
$$

where v_j [m/s] are the velocity components, ν [m^2/s] is the fluid kinematic viscosity, ν_t [m^2/s] is the turbulent viscosity, λ [s^{-1}] corresponds to the inverse permeability and depends on β taking values in [0;1]. The field β relies on the design variable α and represents the same thing. β is obtained after the post-processing applied on α. This will be explained in details later.

The Brinkmann penalisation term is written with an interpolation based on the porosity filed. This interpolation makes then a relation between the local inverse permeability λ and the design field:

$$
\lambda(\beta) \equiv \lambda_{max} I(\beta)
\tag{2.45}
$$

with $I(\beta)$ being the interpolation function. There exists several interpolation functions that will be studied deeply later in order to know which one is best suited for a common CHT

problem.

Turbulence model

Turbulence leads to an increased viscosity. The turbulent viscosity ν_t is modelled thanks to the Spalart-Allmaras one equation turbulence model which defines ν_t as

$$\nu_t = \tilde{\nu} f_{v1} \tag{2.46}$$

with the turbulent variable $\tilde{\nu}$ obtained thanks to the resolution of the following equation

$$R^{\tilde{\nu}} = \frac{\partial(v_j \tilde{\nu})}{\partial x_j} - \frac{\partial}{\partial x_j}\left[\left(\nu + \frac{\tilde{\nu}}{\sigma}\right)\frac{\partial \tilde{\nu}}{\partial x_j}\right] - \frac{c_{b2}}{\sigma}\left(\frac{\partial \tilde{\nu}}{\partial x_j}\right)^2 - \tilde{\nu}P(\tilde{\nu}) + \tilde{\nu}D(\tilde{\nu}) = 0. \tag{2.47}$$

In Eq. 2.47, the production and dissipation terms are given by

$$P(\tilde{\nu}) = c_{b1}\tilde{Y},$$

$$D(\tilde{\nu}) = c_{w1} f_w(\tilde{Y})\frac{\tilde{\nu}}{\Delta^2}$$

where

$$\tilde{Y} = S + \frac{\tilde{\nu}}{\Delta^2 \kappa^2} f_{v2}$$

with $S = |e_{ijk}\frac{\partial v_k}{\partial x_j}\mathbf{i}_i|$ the vorticity magnitude, and Δ the distance from the wall. Details about model constants and functions can be found in [44].

Proceeding the same way as for the momentum equations, an additional source term is added to Eq. 2.47 in order to take into account the presence of material:

$$R^{\tilde{\nu}} = \frac{\partial(v_j \tilde{\nu})}{\partial x_j} - \frac{\partial}{\partial x_j}\left[\left(\nu + \frac{\tilde{\nu}}{\sigma}\right)\frac{\partial \tilde{\nu}}{\partial x_j}\right] - \frac{c_{b2}}{\sigma}\left(\frac{\partial \tilde{\nu}}{\partial x_j}\right)^2 - \tilde{\nu}P(\tilde{\nu}) + \tilde{\nu}D(\tilde{\nu}) + \lambda_{max}I(\beta)\tilde{\nu} = 0. \tag{2.48}$$

Eikonal equation

An additional state variable that appears when conducting the adjoint formulation, which will be clarified later, in order to compute the sensitivities of a fluid-based problem is the wall distance Δ. The differentiation of Δ with respect to the design variable is thus taken into account in the sensitivity analysis. The origin of the effect of the variation of Δ with α is detailed in [44]. In order to deal with $\partial\Delta/\partial\alpha$, the distance field Δ is modeled with the following equation called the Hamilton-Jacobi equation [44]

$$R^{\Delta} = \frac{\partial(c_j\Delta)}{\partial x_j} \underset{\Delta}{} \frac{\partial^2 \Delta}{\partial x_j^2} - 1 = 0 \tag{2.49}$$

where $c_j = \partial\Delta/\partial x_j$.

Heat transfer equation

In a CHT problem, both convection in the fluid and conduction in the solid material take place. The material distribution is not known a priori, so one cannot know which equation should be adapted in each cell. Therefore, both convection and diffusion must be taken into account.

The steady-state heat convection-diffusion equation without no sink nor source is written as

$$\nabla \cdot (\gamma_{th}\nabla T) - \nabla \cdot (\mathbf{v}T) = 0, \tag{2.50}$$

In Newtonian notation, Eq. 2.50 becomes

$$\underbrace{\frac{\partial}{\partial x_j}\left(\gamma_{th}\frac{\partial T}{\partial x_j}\right)}_{\text{Diffusion}} - \underbrace{\frac{\partial}{\partial x_j}(v_j T)}_{\text{Convection}} = 0. \tag{2.51}$$

γ_{th} [m²/s] is the thermal diffusivity, and T [K] is the temperature.
The thermal diffusivity of a solid is defined as

$$\gamma_{th}^s = \frac{k^s}{\rho^s c_p^s} \tag{2.52}$$

where k^s [W/(m·K)] is the conductivity of the solid, ρ^s [kg/m³] is its density, and c_p^s is the specific heat capacity [J/(kg·K)].
For a fluid, this is defined as

$$\gamma_{th}^f = \left(\frac{\nu}{Pr} + \frac{\nu_t}{Pr_t}\right) \tag{2.53}$$

where ν/Pr is the molecular thermal diffusivity of the fluid, and ν_t/Pr_t is the turbulent one. Pr corresponds to the laminar Prandtl number quantifying the ratio between the momentum diffusivity and the thermal diffusivity

$$Pr = \frac{c_p^f \mu}{k^f}$$

where c_p^f [J/(kg·K)] is the specific heat of the fluid, μ [Pa·s] is the dynamic viscosity of the fluid, and k^f is the thermal conductivity of the fluid [W/(m·K)]. The turbulent Prandtl number is denoted Pr_t and describes the ratio between the momentum eddy diffusivity ε_M [m²/s] and the heat transfer eddy diffusivity ε_H [m²/s] [45].

As mentioned previously, the material distribution in the domain is not known beforehand. In order to cope with this, the solution is to introduce the interpolation of the thermo-physical properties between the solid and the fluid. This interpolation depends again on the field β. The thermal diffusivity ratio becomes

$$\gamma_{th} = \frac{k(I^k(\beta))}{\rho(I^\rho(\beta))c_p(I^{cp}(\beta))} + \frac{\nu_t(I^{\nu_t}(\beta))}{Pr_t(I^{Pr_t}(\beta))} \tag{2.54}$$

where the interpolation functions I will be studied later.

As a result, the diffusion term of Eq. 2.51 becomes

$$\frac{\partial}{\partial x_j}\left(\gamma_{th}\frac{\partial T}{\partial x_j}\right) = \frac{\partial}{\partial x_j}\left[\left(\frac{k(I^k(\beta))}{\rho(I^\rho(\beta))c_p(I^{c_p}(\beta))} + \frac{\nu_t(I^{\nu_t}(\beta))}{Pr_t(I^{Pr_t}(\beta))}\right)\frac{\partial T}{\partial x_j}\right]. \tag{2.55}$$

Concerning the convection term, the latter is multiplied by $(1-\beta)$ in order to cancel its contribution in solidified parts of the domain. Taking this into account together with Eq. 2.55, the CHT equation is derived

$$R^T = (1-\beta)\rho(I^\rho(\beta))c_p(I^{c_p}(\beta))\frac{\partial(v_jT)}{\partial x_j}$$
$$- \frac{\partial}{\partial x_j}\left[\left(k(I^k(\beta)) + \rho(I^\rho(\beta))c_p(I^{c_p}(\beta))\frac{\nu_t(I^{\nu_t}(\beta))}{Pr_t(I^{Pr_t}(\beta))}\right)\frac{\partial T}{\partial x_j}\right] = 0 \tag{2.56}$$

The primal equations that govern the steady-state incompressible flow of a CHT topology optimisation problem are finally summarized here below:

$$R^p = \frac{\partial v_j}{\partial x_j} = 0 \tag{2.57}$$

$$R_i^v = v_j\frac{\partial v_i}{\partial x_j} - \frac{\tau_{ij}}{\partial x_j} + \frac{\partial p}{\partial x_i} + \lambda_{max}I^v(\beta)v_i = 0 \tag{2.58}$$

$$R^{\tilde{\nu}} = v_j\frac{\partial\tilde{\nu}}{\partial x_j} - \frac{\partial}{\partial x_j}\left[\left(\nu + \frac{\tilde{\nu}}{\sigma}\frac{\partial\tilde{\nu}}{\partial x_j}\right)\right] - \frac{c_{b2}}{\sigma}\left(\frac{\tilde{\nu}}{\partial x_j}\right)^2 + (-P(\tilde{\nu}) + D(\tilde{\nu}))\tilde{\nu} + \lambda_{max}I^{\tilde{\nu}}(\beta)\tilde{\nu} = 0 \tag{2.59}$$

$$R^\Delta = \frac{\partial}{\partial x_j}(\frac{\partial\Delta}{\partial x_j}\Delta) - \Delta\frac{\partial^2\Delta}{\partial x_j^2} - 1 = 0 \tag{2.60}$$

$$R^T = (1-\beta)\rho(I^\rho(\beta))c_p(I^{c_p}(\beta))\frac{\partial(v_jT)}{\partial x_j}$$
$$- \frac{\partial}{\partial x_j}\left[\left(k(I^k(\beta)) + \rho(I^\rho(\beta))c_p(I^{c_p}(\beta))\frac{\nu_t(I^{\nu_t}(\beta))}{Pr_t(I^{Pr_t}(\beta))}\right)\frac{\partial T}{\partial x_j}\right] = 0 \tag{2.61}$$

A particular attention must be accorded to the value of the maximum inverse permeability. λ_{max} controls in fact the values of v_j, $\tilde{\nu}$, and Δ in the solidified domain. In order to have almost impermeable solid walls, λ_{max} must tend to infinity. However, a very high value of λ_{max} may lead to numerical instabilities. A practical rule for choosing the value of λ_{max} is based on the Darcy number Da which represents the ratio between the viscous forces and the porous forces:

$$Da = \frac{\nu}{\lambda_{max}l^2} \tag{2.62}$$

25

where l [m] is the characteristic length of the considered problem. This number must be small enough in order to have v_j, $\tilde{\nu}$, and Δ very close to zero in solidified zones. According to [24], almost impermeable solid zones are obtained for $Da \lesssim 10^{-5}$. This will be studied in chapter 3.

Concerning the boundary conditions, these are typical of an ordinary fluid problem. They are summarized in Tab. 2.1 for the velocity U, the pressure p, the temperature T, and the turbulent variables. Note that for the temperature, different type of boundary conditions may be imposed on the solid walls. If some of the solid walls are in fact adiabatic, then a zero Neumann boundary condition is imposed.

	Inlet	Outlet	Solid walls
U	Dirichlet	zero Neumann	zero Diricihlet
p	zero Neumann	zero Neumann	zero Dirichlet
T	Dirichlet	zero Neumann	Dirichlet or zero Neumann
$\tilde{\nu}$	Dirichlet	Zero Neumann	Dirichlet
ν_t	Dirichlet	Dirichlet	Dirichlet
Δ	zero Neumann	zero Neumann	Dirichlet

Table 2.1: General primal boundary conditions for a CHT problem.

2.3.2 Three field topology optimisation scheme

When using a density (or porosity) based approach in topology optimisation, some modifications should be applied to the design field α in order to have a clear material distribution. The design variable α varying between zero and one, grey zones with intermediate values of α appear, which blurs the transition from solid to fluid regions. On top of that, checkerboard patterns may appear. In order to deal with these effects, and have a clear transition from fluid to solid parts without generating alternating fluid and solid zones, the design field must be regularised and projected. The successive adjustments made on the field α give rise to the three field topology optimisation scheme. The regularisation gives the regularised field $\tilde{\alpha}$. The projection applied on $\tilde{\alpha}$ produces then the regularised and projected field β. If the regularisation and the projection are omitted, then β corresponds to α. Note that if they are activated, the regularisation and the projection are applied at the end of each optimisation cycle. The order of the three field scheme steps and their respective effects are shown in Fig. 2.5. For the non-regularised design field α, the checkerboard patterns are observed for the white zones inside the black regions. The additional blurring brought by the regularisation is also remarkable for the regularised field $\tilde{\alpha}$, but in which the checkerboard is removed. Finally, thanks to the regularisation and the projection, a clear transition from fluid to solid region is obtained.

(a) Design field α.   **(b)** Regularised design field $\tilde{\alpha}$.   **(c)** Regularised and projected field β.

Figure 2.5: Three field scheme TO steps and their respective effects.

The interpretation of these fields is the same. A white region corresponds to a non-solid place where the respective value of the field is zero and a solid region correspond to the black color with the field equal to one in the solid parts. The proceedings of each step of the three field topology optimisation scheme are explained in the following sections.

2.3.2.1 Regularisation of the design field

When using a density-based approach in topology optimisation, the solution is highly mesh-dependent. With the refinement of the mesh, the solution may get more and more different. Also, the material distribution can have checkerboard patterns, i.e. alternating solid and fluid regions, which do not represent a physically acceptable flow. In order to avoid these phenomena and mitigate the effects of the mesh such that the solution is mesh independent without alternating fluid and solid zones, some modifications must be applied to the design field α.

In order to deal with those problems, the solution is to regularise the density field such that the latter looks smoother. Several techniques of regularisation have been implemented in the past. One of the developed techniques is the density-based filter which is directly applied on the design field α [46]. The density in a given cell depends on the density of the neighbouring cells by modifying α of a cell based on the density of the nearby cells. This is done through a convolution product

$$\tilde{\alpha}(\mathbf{x}) = (F * \alpha)(\mathbf{x}) = \int_B F(\mathbf{x} - \mathbf{y})\alpha(\mathbf{y})\, d\mathbf{y} \tag{2.63}$$

where F is the filter function, α is the initial design field, $\tilde{\alpha}$ is the filtered one, F is a weighting function, and B is the support domain of the filter function. B is a circle in 2D and a sphere in 3D, both of radius R. Given this circle (sphere), the density in a cell is a weighted average of the density in the neighbouring cells, with the neighborhood given by this circle (sphere) of radius R. There exists different weighting functions, but the most common one is the hat function [47] defined as

$$F(\mathbf{x}) = \begin{cases} \frac{1}{F_w}\left(1 - \frac{|\mathbf{x}|}{R}\right) & \text{if } |\mathbf{x}| \leqslant R \\ 0 & \text{if } |\mathbf{x}| > R \end{cases} \tag{2.64}$$

where F_w is a weighting parameter ensuring that the filter preserves the total volume. This condition is obtained thanks to the following integral

$$\int_B F(\mathbf{x})\,d\mathbf{x} = 1. \tag{2.65}$$

Thanks to this condition, the material volume will be the same for the filtered field and the non-filtered one.

The problem with this mesh-dependent density-based filtering is that it needs the information of the neighbouring cells. Taking information from other cells that are close to a given volume cell may be cumbersome when the geometry is complicated. The complexity of the process also increases when employing parallel running. In this case, the domain being partitioned into sub-domains, the volume cells at the border of the sub-domains will need information from the cells in the nearby sub-domain. The communication between the sub-domains is a costly process when doing parallel running. For all of these reasons, a more robust way of implementing regularisation is then needed.

The alternative solution to the convolution given by Eq. 2.63 is a Helmotz type PDE. This was first used for sensitivity filtering [48], and was then also used for density filtering [46]. The filtered (or regularised) field is acquired thanks to the solution of the following PDE

$$-r^2\frac{\partial^2\tilde{\alpha}}{\partial x_j^2} + \tilde{\alpha} = \alpha \tag{2.66}$$

where r controls the effective width of the filter, and $\tilde{\alpha}$ is the regularised field. For large values of r, there will be large grey zones, while for small values of r the transition from solid to fluid regions will be clear, and small-scale features will be captured. So r highly controls the solution that will be obtained. This is illustrated in Fig. 2.6 and Fig. 2.7. The solution for different radii are completely different. For small a radius, the difference between the fields α and $\tilde{\alpha}$ is almost negligible and the small details are captured. For a big radius, even though the field α includes small features in its distribution of material, the big radius of the regularisation makes somehow disappear them by bringing some blurring in the regularised field. It must be remarked that these two solutions are obtained for the same optimisation parameters that are not detailed here. Only the radius of the regularisation differs between the two solutions. This proves how much impact the radius can have in the solution.

(a) Design field α. (b) Regularised field $\tilde{\alpha}$.

Figure 2.6: Design field α and the regularised field $\tilde{\alpha}$ of a solution with a small regularisation radius.

(a) Design field α.

(b) Regularised field $\tilde{\alpha}$.

Figure 2.7: Design field α and the regularised field $\tilde{\alpha}$ of a solution with a big regularisation radius.

It is possible to obtain a relation between the length parameter r and the filter radius R [47]. These two parameters are correlated as follows

$$r = \frac{R}{2\sqrt{3}} \tag{2.67}$$

and Eq. 2.66 becomes

$$-\left(\frac{R}{2\sqrt{3}}\right)^2 \frac{\partial^2 \tilde{\alpha}}{\partial x_j^2} + \tilde{\alpha} = \alpha. \tag{2.68}$$

As stated in [10], the filter radius R is generally obtained from the average cell volume $\bar{V}$

$$R = \left(\bar{V}\right)^{1/d} \tag{2.69}$$

where d is equal to 2 in 2D, and 3 in 3D problems.

The modification of the design field does not end with the regularisation. As a matter of fact, after the regularisation, the density field gets blurred, giving thus grey zones, with the design variable taking intermediate values between zero and one, that are not acceptable. Although these grey zones can be removed thanks to the penalisation parameter in the interpolation functions that will be seen later, it is required to apply a supplementary adjustment. This is done by the projection. This is explained in the following section.

2.3.2.2 Projection of the design field

The projection helps to give a precise transition from solid to fluid regions. There are two reasons why the material distribution is blurred. First of all, the problem is a relaxed one in the sense that the design variable α can take intermediate values between zero and one. The second reason is the blurring brought by the regularisation. Because of these phenomena, the design field has to be projected in order to remove grey zones. This is done thanks to the parameterised projection suggested by Xu *et al.* [49]. This projection technique was then adapted in [50], and the projected density field β is obtained by a smooth function controlled by a threshold η and a steepness parameter b:

$$\beta = \begin{cases} \eta \left[e^{-b(1-\tilde{\alpha}/\eta)} - (1-\tilde{\alpha}/\eta)e^{-b} \right], & 0 \leqslant \tilde{\alpha} \leqslant \eta \\ (1-\eta)\left[1 - e^{-b(\tilde{\alpha}-\eta)/(1-\eta)} + (\tilde{\alpha}-\eta)/(1-\eta)e^{-b} \right] + \eta, & \eta < \tilde{\alpha} \leqslant 1 \end{cases} \tag{2.70}$$

The expression given by Eq. 2.70 can be replaced by a shorter one based on the tanh function:

$$\beta = \frac{\tanh(\eta b) + \tanh[b(\tilde{\alpha} - \eta)]}{\tanh(\eta b) + \tanh[b(1 - \eta)]} \tag{2.71}$$

Concerning the choice of the threshold parameter η, Xu *et al.* [49] and Kawamoto *et al.* [51] showed that the convergence for η close to 0.5 is smooth. This value is used in the following.
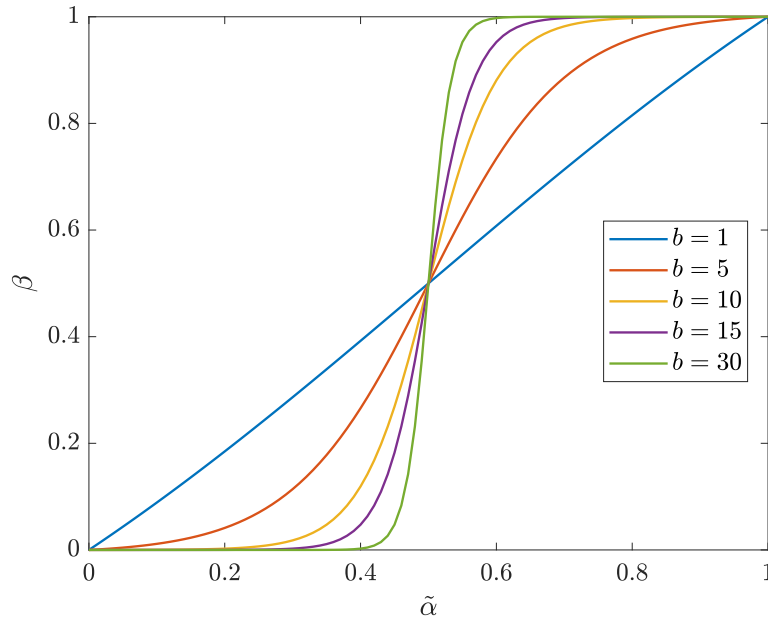
Figure 2.8: Projection function for different values of its steepness parameter b.

Regarding the sharpening parameter b, the latter plays a big role in the final distribution of material in the domain. The allure of the projection function given by Eq. 2.71 is shown in Fig. 2.8. For increasing values of b, the projection gets sharper. A priori, it can be deduced that the value of b should be high enough in order to generate a clear material distribution without grey zones. But in the upcoming examples of chapter 3, it will be shown that imposing a high value for b will lead to a topology with almost no material.

2.3.3 Continuous adjoint formulation

Given a certain objective function J, the goal is to have information about its sensitivity with respect to the design field α in order to generate the optimal material distribution. This objective function depends on the state variables. As it was explained in section 2.2.1, the computation of the sensitivity using a direct or a finite difference approach is a very costly operation whose price is proportional to the (very high) number of design variables N. In order to prevent the resolution of the system of primal equations a number of times proportional to the dimension N of the problem in each optimisation cycle, the solution is to

perform the adjoint formulation which constitutes a robust way of computing $\delta J/\delta\alpha$. Thanks to this approach, the flow equations have to be solved only once in each optimisation cycle, and then another set of equations which are called the adjoint equations are solved also only one time in the course of one cycle. Thanks to this technique, the sensitivity $\delta J/\delta\alpha$ in each optimisation cycle is obtained at a price that does not depend on N. This makes the power of the adjoint formulation.

The starting point of the adjoint method is to define an augmented objective function in which the primal equations are taken into account. These equations have to be satisfied, and thus can be seen as constraints. The augmented objective function is defined as

$$J_{aug} = J + \int_\Omega p_a R^P \, d\Omega + \int_\Omega u_i R_i^v \, d\Omega + \int_\Omega \tilde{\nu}_a R^{\tilde{\nu}} \, d\Omega + \int_\Omega \Delta_a R^\Delta \, d\Omega + \int_\Omega T_a R^T \, d\Omega \quad (2.72)$$

where p_a, u_i, $\tilde{\nu}_a$, Δ_a, and T_a correspond respectively to the adjoint pressure, adjoint velocity components, adjoint to turbulence variable $\tilde{\nu}$, adjoint to the wall distance, and ajoint temperature. As the primal equations have to be satisfied, it can be noted that $J_{aug} \equiv J$. In the upcoming, if it is not clearly specified, the distinction between J and J_{aug} will not be done.

The goal is now to compute the total variation $\frac{\delta J}{\delta\alpha}$:

$$\frac{\delta J_{aug}}{\delta\alpha} = \frac{\delta J}{\delta\alpha} + \frac{\delta}{\delta\alpha} \int_\Omega p_a R^P \, d\Omega + \frac{\delta}{\delta\alpha} \int_\Omega u_i R_i^v \, d\Omega + \frac{\delta}{\delta\alpha} \int_\Omega \tilde{\nu}_a R^{\tilde{\nu}} \, d\Omega + \frac{\delta}{\delta\alpha} \int_\Omega \Delta_a R^\Delta \, d\Omega + \int_\Omega T_a R^T \, d\Omega$$
$$(2.73)$$

For a quantity ϕ, its total variation is defined as

$$\frac{\delta\phi}{\delta\alpha} = \frac{\partial\phi}{\partial\alpha} + \frac{\partial\phi}{\partial x_k} \frac{\delta x_k}{\delta\alpha}. \quad (2.74)$$

Since there is no modification in the mesh nor in the boundaries of the domain, Eq. 2.74 becomes

$$\frac{\delta\phi}{\delta\alpha} = \frac{\partial\phi}{\partial\alpha} \quad (2.75)$$

Using Eq. 2.75 and the Leibniz theorem, Eq. 2.73 becomes

$$\frac{\delta J_{aug}}{\delta\alpha} = \frac{\delta J}{\delta\alpha} + \int_\Omega p_a \frac{\partial R^p}{\partial\alpha} \, d\Omega + \int_\Omega u_i \frac{\partial R_i^v}{\partial\alpha} \, d\Omega + \int_\Omega \tilde{\nu}_a \frac{\partial R^{\tilde{\nu}}}{\partial\alpha} \, d\Omega + \int_\Omega \Delta_a \frac{\partial R^\Delta}{\partial\alpha} \, d\Omega + \int_\Omega T_a \frac{\partial R^T}{\partial\alpha} \, d\Omega$$
$$(2.76)$$

In Eq. 2.76, the differentiation of the primal equations leads to the differentiation of the state variables. But the objective of the adjoint method is to prevent the costly computation of these state variables differentiation. Therefore, the solution brought by the adjoint method is to further develop Eq. 2.76 into volume and surface integrals, and then to derive the adjoint equations and the adjoint boundary conditions that are going to cancel the volume and surface integrals that include the differentiation of the state variables with the design field. The lengthy process in order to derive the adjoint equations and the adjoint boundary conditions is done in [44, 52, 53]. Following the developments in these sources, the adjoint equations are written as

$$R^{p_a} = -\frac{\partial u_j}{\partial x_j} = 0 \tag{2.77}$$

$$R_i^u = \underbrace{u_j \frac{\partial v_j}{\partial x_i}}_{\text{ATC}} - \frac{\partial(v_j u_i)}{\partial x_j} + \frac{\partial p_a}{\partial x_i} - (\nu + \nu_t)\frac{\partial}{\partial x_j}\left(\frac{\partial u_j}{\partial x_i} + \frac{\partial u_i}{\partial x_j}\right) \tag{2.78}$$

$$+ \tilde{\nu}_a \frac{\partial \tilde{\nu}}{\partial x_i} - \frac{\partial}{\partial x_l}\left(C_S(\tilde{\nu})\frac{1}{S}e_{mjk}\frac{\partial v_k}{\partial x_j}e_{mli}\tilde{\nu}_a\tilde{\nu}\right) + \lambda_{max}I^v(\beta)u_i = 0$$

$$R^{\tilde{\nu}_a} = -\frac{\partial(v_j\tilde{\nu}_a)}{\partial x_j} - \frac{\partial}{\partial x_j}\left[\left(\nu + \frac{\tilde{\nu}}{\sigma}\right)\frac{\partial\tilde{\nu}_a}{\partial x_j}\right] + \frac{1}{\sigma}\frac{\partial\tilde{\nu}_a}{\partial x_j}\frac{\partial\tilde{\nu}}{\partial x_j} \tag{2.79}$$

$$+ \frac{2c_{b2}}{\sigma}\frac{\partial}{\partial x_j}\left(\tilde{\nu}_a\frac{\partial\tilde{\nu}}{\partial x_j}\right) + \tilde{\nu}_a\tilde{\nu}C_{\tilde{\nu}} + \frac{\partial\nu_t}{\partial\tilde{\nu}}\frac{\partial u_i}{\partial x_j}\left(\frac{\partial v_i}{\partial x_j} + \frac{\partial v_j}{\partial x_i}\right)$$

$$+ (-P(\tilde{\nu}) + D(\tilde{\nu}))\tilde{\nu}_a + \lambda_{max}I^{\tilde{\nu}}(\beta)\tilde{\nu}_a + \rho\frac{c_p}{Pr_t}\frac{\partial T_a}{\partial x_j}\frac{\partial T}{\partial x_j}\frac{\partial\nu_t}{\partial\tilde{\nu}} = 0$$

$$R^{\Delta_a} = -2\frac{\partial}{\partial x_j}\left(\Delta_a\frac{\partial\Delta}{\partial x_j}\right) + \tilde{\nu}\tilde{\nu}_a C_\Delta = 0 \tag{2.80}$$

$$R^{T_a} = -\rho c_p\frac{\partial}{\partial x_j}\left[(1-\beta)v_j T_a\right] \tag{2.81}$$

$$- \frac{\partial}{\partial x_j}\left[\left(k(I^k(\beta)) + \rho(I^\rho(\beta))c_p(I^{c_p}(\beta))\frac{\nu_t(I^{\nu_t}(\beta))}{Pr_t(I^{Pr_t}(\beta))}\right)\frac{\partial T_a}{\partial x_j}\right] = 0$$

More information about the factors $C_{\tilde{\nu}}$, C_S, and C_Δ can be found in [44, 52, 53].

The first equation represents the adjoint to the continuity equation. The second set of equations corresponds to the adjoint momentum equations which include the convection, diffusion, adjoint pressure gradient terms, and other terms related to the turbulence model variables. The convection term is linear since the adjoint velocity is convected by the primal velocity which is known a priori thanks to the primal equations solved before the resolution of the adjoint equations. The ATC label in Eq. 2.79 corresponds to the adjoint transpose convection. This term is numerically stiff and may cause in some cases convergence problems. To cope with this term, several model exists. These will be described further. The other equations stand respectively for the adjoint turbulence model equation, the adjoint wall distance equation, and the adjoint energy equation.

Regrading the adjoint boundary conditions, these are obtained thanks to the cancellation of the boundary integrals involving the differentiation of the flow variables. Following the same approach as in [54, 44], the adjoint conditions applied at the different boundaries are summarised here below:

Inlet

The following adjoint conditions should be verified at the inlet

$$u_i n_i = -\frac{\partial J}{\partial p}, \ u_i t_i = 0 \tag{2.82}$$

where t_i are the components of the unit tangent to the inlet surface.

Zero Dirichlet boundary conditions are imposed for the adjoint effective viscosity $\tilde{\nu}_a$ and for the adjoint temperature, and a zero Neumann boundary condition is applied on the adjoint pressure p_a. Concerning the latter, no boundary integral with flow variable differentiation needs a specific adjoint boundary condition for p_a. So the adjoint boundary condition of the adjoint pressure p_a is natural, in the sense that it has the same type of condition as the primal pressure at the inlet.

Outlet

The adjoint boundary conditions for the adjoint pressure p_a and the adjoint velocity compoenents u_i are obtained with the resolution of the following equation

$$\begin{aligned}
\mathcal{BC}_{1,i} &= u_i v_j n_j + (\nu + \nu_t)\frac{\partial u_i}{\partial x_j} n_j + (u_j v_j + p_a)n_i + \frac{\partial J}{\partial v_i} \\
&+ \tilde{\nu}_a \tilde{\nu} n_i + \tilde{\nu}_a \tilde{\nu} C_S(\tilde{\nu})\frac{1}{S}e_{jki}e_{jmq}\frac{\partial v_q}{\partial x_m} n_k + TT_a n_i = 0
\end{aligned} \tag{2.83}$$

The adjoint boundary conditions for T_a and $\tilde{\nu}_a$ are given by the following Robin type equations

$$\mathcal{BC}_2 = v_i n_i T_a + \left(\frac{\nu}{Pr} + \frac{\nu_t}{Pr_t}\right)\frac{\partial T_a}{\partial x_j} n_j + \frac{\partial J}{\partial T} = 0 \tag{2.84}$$

$$\begin{aligned}
\mathcal{BC}_3 &= -\frac{\delta \nu_t}{\delta \tilde{\nu}}u_i \left(\frac{\partial v_i}{\partial x_j} + \frac{\partial v_j}{\partial x_i}\right)n_j - \frac{\delta \nu_t}{\delta \tilde{\nu}}\frac{T_a}{Pr_t}\frac{\partial T}{\partial x_j} n_j + \tilde{\nu}_a v_j n_j \\
&+ \left(\nu + \frac{\tilde{\nu}}{\sigma}\right)\frac{\partial \tilde{\nu}_a}{\partial x_j} n_j + \frac{\partial J}{\partial \tilde{\nu}} = 0
\end{aligned} \tag{2.85}$$

Solid wall boundaries

Zero Dirichlet conditions are imposed to u_i, T_a, and $\tilde{\nu}_a$, and a zero Neumann boudnary ondition is applied on p_a.

Now that the adjoint equations and adjoint boundary conditions are developed, the final expression of the sensitivity can be derived. This is done hereafter.

2.3.4 Final expression of the sensitivity

The adjoint equations and the adjoint boundary conditions satisfied, the final expression of the sensitivity can now be obtained. Since the design field undergoes in each optimisation cycle the regularisation and the projection ordered as illustrated in Fig. 2.9, $\delta J/\delta\alpha$ is obtained by a kind of chain rule.
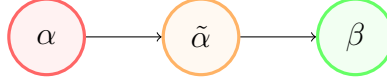
Figure 2.9: Illustration of the order of the modifications applied on the design field: α is the initial field, $\tilde{\alpha}$ is the regularised one, and β is the regularised and projected field.

In order to go from the regularised field to the projected field, there exists an analytical expression (Eq. 2.71). Therefore, the partial derivative $\frac{\partial\beta}{\partial\tilde{\alpha}}$ can be easily computed. Using the chain rule, the differentiation of J with respect to $\tilde{\alpha}$ is thus given by

$$
\begin{aligned}
\frac{\delta J}{\delta\tilde{\alpha}} = &\int_\Omega \lambda \left[\left(u_i v_i \frac{\partial I^v}{\partial\beta} + \tilde{\nu}_a\tilde{\nu}\frac{\partial I^{\tilde{\nu}}}{\partial\beta} + \Delta_a\Delta\frac{\partial I^\Delta}{\partial\beta} \right) - \rho c_p T_a \frac{\partial(v_j T)}{\partial x_j} \right] \frac{\partial\beta}{\partial\tilde{\alpha}} \, d\Omega \\
&+ \int_\Omega \left[\frac{\partial}{\partial x_j}\left(T_a\frac{\partial T}{\partial x_j} \right) - T_a\frac{\partial^2 T}{\partial x_j^2} \right] \frac{\partial k}{\partial\beta}\frac{\partial\beta}{\partial\tilde{\alpha}} \, d\Omega \\
&+ \int_\Omega (1-\beta)T_a\frac{\partial(v_j T)}{\partial x_j}\left(c_p\frac{\partial\rho}{\partial\beta} + \rho\frac{\partial c_p}{\partial\beta} \right) \frac{\partial\beta}{\partial\tilde{\alpha}} \, d\Omega
\end{aligned}
\tag{2.86}
$$

The challenge is to calculate the differentiation of $\tilde{\alpha}$ with α. As a matter of fact, there is no direct relation between $\tilde{\alpha}$ and α. As stated in [10], the solution is to introduce the adjoint regularisation equation which has the same form as the primal regularisation equation (Eq. 2.66):

$$
R^{\Psi_{\tilde{\alpha}}} = -r^2\frac{\partial^2\Psi_{\tilde{\alpha}}}{\partial x_j^2} + \Psi_{\tilde{\alpha}} - \frac{\delta J}{\delta\tilde{\alpha}} = 0
\tag{2.87}
$$

where $\Psi_{\tilde{\alpha}}$ is equal to $\frac{\delta J}{\delta\alpha}$. By combining Eq. 2.86 and Eq. 2.87, the total variation of J with the design field α is found.

2.3.5 Global layout of the optimisation

Now that all the steps in order to solve the problem are known, the global procedure used in the software in order to deal with a fluid based topology optimisation of a CHT problem can be described. This is summarised in Fig. 2.10.
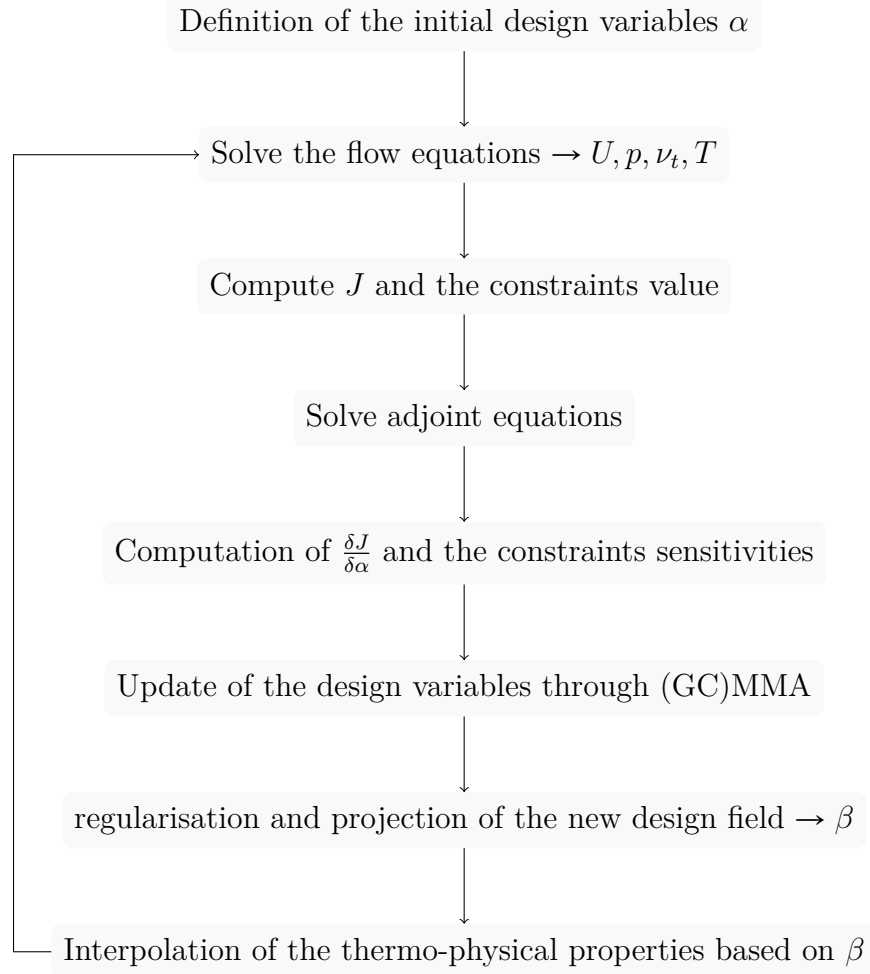
Figure 2.10: Global layout of the optimisation process in a fluid problem.

First of all, the initial design field α across the domain is defined. Then, the optimiser starts to do its optimisation loops. In each one, the primal equations are resolved. This resolution gives the state variables of the problem. Then, the objective function J and the constraints, which also corresponds to certain functions, are computed. Subsequently, the adjoint equations are solved, which permits the computation of the sensitivity $\delta J/\delta \alpha$. The sensitivity of the constraints are also computed. Thanks to these sensitivities, convex sub-problems are successively created with (GC)MMA in order to find the new iterated solution, i.e. the new design-field. The convex approximation of the optimisation problem done thanks to (GC)MMA makes possible to use the KKT conditions which are necessary and sufficient optimality conditions in the case of a convex problem. Once this convex sub-problem is solved, a new design field α is obtained. This field is regularised and projected. Afterwards, the thermo-physical properties are interpolated. Subsequently, a new optimisation cycle begins with the resolution of the primal equations and continues the ensuing steps explained here above.

2.3.6 OpenFOAM software

The software used in the scope of this thesis is OPENFOAM (Open-source Field Operation And Manipulation) [55]. This is an open-source software written in C++ widely used for Computational Fluid Dynamics (CFD). It relies on finite-volume method and can handle a multitude of physics going from simple laminar flows to complex flow patterns including various types of physics such as heat transfer, acoustics, electromagnetism and so on.

2.3.6.1 *adjointOptimisationFoam* executable

The *adjointOptimisationFoam* executable is used in the current work. The corresponding software is OpenFOAM v1906 [56] which was developed by the Parallel CFD & Optimization Unit of the National Technical University of Athens [57]. The software employs the continuous adjoint method in order to compute the gradient and then conduct optimisation loops.

As topology optimisation will be applied to CHT problems, both flow equations and energy equation must be considered. In the software, the available solver that is used in order to handle the primal equations for this type of problem is called *simpleEnergy* which is based on the *simpleFoam* solver. The latter is used for steady-state, incompressible, turbulent flow in which the SIMPLE (Semi-Implicit Method for Pressure Linked Equations) algorithm is implemented. The word "Energy" in *simpleEnergy* stands for the energy equation which is solved by setting a single temperature field over the fluid and solid at the same time. As it was explained in section 2.3.1, the thermal properties are interpolated between the fluid and the solid, and the convection term is cancelled in solid parts thanks to the factor $(1 - \beta)$ in front of the latter. This makes possible the resolution of a single energy equation.

In order to treat the adjoint equations, the same methodology as for the primal equations is used. The adjoint equations for a CHT problem are solved thanks to the *adjointSimpleEnergy* solver which is the similar of *simpleEnergy*.

Chapter 3

Parameter study

In this section, the different parameters involved in the optimisation process will be studied. To do so, a practical example consisting of a two-dimensional CHT problem will be considered. The goal for this system will be to enhance the heat transfer to the fluid flowing inside the domain and decrease as much as possible the pressure losses given a volume constraint that has to be verified.

First of all, the impact of the spatial discretisation will be assessed. Then, the different parameters playing in the three field topology optimisation scheme, namely the regularisation length parameter and the projection steepness, will be analysed. The different interpolation functions used for the Brinkman penalisation term and for the thermo-physical properties will be studied. The effect of the Darcy number will be evaluated. Following this, the different ways of updating the design variable α inside the domain will be explained. After that, the impact of the initial conditions will be examined, which will highlight the presence of multiple local optimal solutions in a practical TO problem. Then, the effect of the Reynolds number will be assessed. Finally, in order to check out the validity of the "porous" approach used in fluid TO, the calculations will be verified in a domain with real solid walls.

3.1 Problem definition

In order to perform a parameter study, a simple two dimensional configuration has been chosen. This consists of a CHT problem. The flow inside the domain is steady and laminar. The geometry in the $\vec{X} - \vec{Y}$ plane is shown in Fig. 3.1. It is composed of a square box and inflow/outflow channels. A is equal to 10 cm, and the inlet and outlet heights are both equal to $A/5 = 2$ cm. The walls in red are maintained at a constant temperature equal to $T_{\mathrm{h}} = 425$ K. The other walls in grey are adiabatic walls. The inlet channel is long enough in order to establish a fully developed flow before entering into the square box, and the outflow channel has also been set long enough in order to prevent that the boundary conditions imposed at the outlet influence the optimisation taking place in the square box. Note that the geometry is not drawn to scale regarding the length of the channels.

The air enters into the domain at a constant temperature T_{in}= 375 K with an inlet velocity equal to 0.115 m/s. The direction of the flow is from left to right as it is shown by the blue arrows in Fig. 3.1. At 375 K, the kinematic viscosity of air is equal to 2.317×10^{-5} m^2/s. The Reynolds number, based on the inlet height given by $A/5$ has then a value approximately equal to 100. A volume constraint is imposed on the fluid inside the square box. The amount of fluid is restricted by a maximum fluid volume ration equal to ϕ^f_{max} = 0.4 inside this square box. The considered solid material is aluminium. The thermal properties of air and aluminium at their corresponding temperature are given in Tab. 3.1. These properties are considered to be constant with temperature. The boundary conditions are given in Tab. 3.2.

	k [W/(mK)]	c_p [J/(kg K)]
Air	0.03186	1010.6
Aluminium	240	887

Table 3.1: Thermal properties of air and aluminium at respectively 375 K and 425 K.
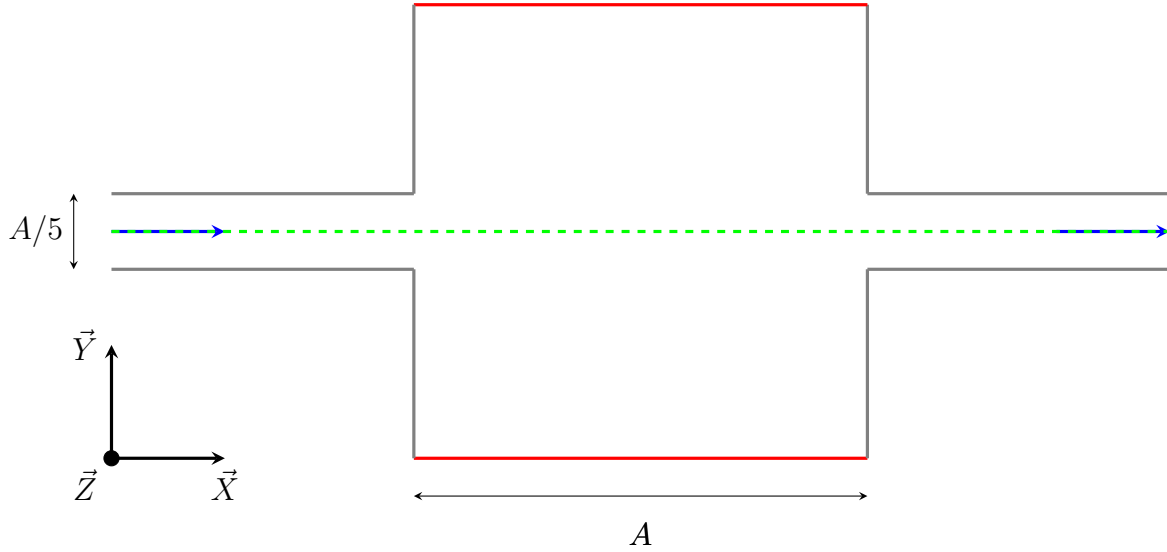
Figure 3.1: 2D design for CHT topology optimisation.

	Inlet	Outlet	Adiabatic walls	Heated walls
U	Dirichlet	Zero Neumann	Zero Dirichlet	Zero Dirichlet
p	Zero Neumann	Zero Dirichlet	Zero Neumann	Zero Neumann
T	Dirichlet	Zero Neumann	Zero Neumann	Dirichlet

Table 3.2: Boundary conditions for the 2D CHT topology optimisation.

As the domain is symmetric with respect to the dashed green line (Fig. 3.1), the simulations will be performed in only the bottom half of the domain (see Fig. 3.2) in order to decrease the computational cost. Throughout the optimisation process, the inlet and exit channels (named Ω_{in} and Ω_{out}) remain fluid. Only the central square box (noted Ω_{opt}) of the domain is optimised, i.e can have a solid material distribution.
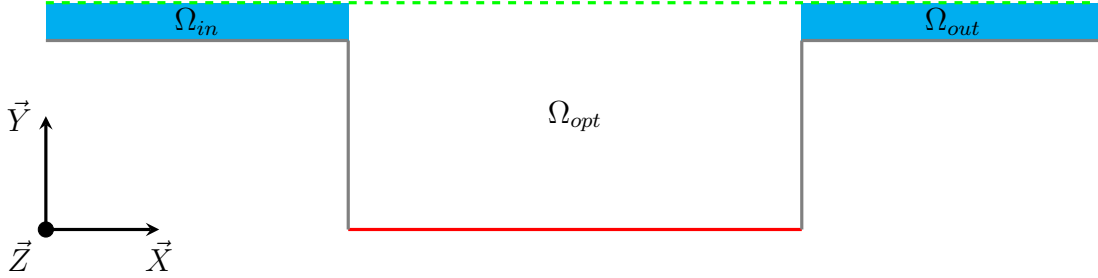
Figure 3.2: Half 2D domain for CHT topology optimisation in which the simulations will run.

3.2 Objective functions and problem formulation

The objectives of a typical CHT optimisation problem is to maximise the heat transfer to the coolant fluid flowing inside the domain while limiting the pressure losses.

Mathematically, these can be expressed in terms of the following objective functions

$$J_{\text{Pt}} = -\int_{S_{I,O}} \left(p + \frac{1}{2}|U|^2 \right) v_i n_i \, dS, \tag{3.1}$$

$$J_{\text{th}} = \int_{S} (\rho c_p T) v_i n_i \, dS. \tag{3.2}$$

where $|U|$ [m/s] is the velocity magnitude, and n_i are the componnets of the normal to the considered surfaces. Eq. 3.1 corresponds to the pressure losses computed between the inlet and the outlet, and Eq. 3.2 quantifies the convective heat flux at a surface S which is the outlet surface in this case. A particular remark has to be done regarding the computation of these quantities in the used software. These are not exactly computed as in Eq. 3.1 and

Eq. 3.2 but in the following form:

$$J_{\text{Pt}} = -\left[\left\langle\left(p + \frac{1}{2}|U|^2\right)\Delta_y \times \Delta_z\right\rangle_{out} - \left\langle\left(p + \frac{1}{2}|U|^2\right)\Delta_y \times \Delta_z\right\rangle_{in}\right] \quad (3.3)$$

$$J_{\text{th}} = \rho c_p \langle T v_i n_i \rangle_S \Delta_y \times \Delta_z \quad (3.4)$$

where the symbol $< ... >$ stands for the mean operator, Δ_y stands for the length of the surfaces along the y direction, and Δ_z is the width of the geometry. As a matter of fact, even if 2D simulations are done, OPENFOAM needs a 3D geometry, so the geometry has a length along the z-direction. Then, in order to have a 2D case, the *empty* condition is applied on the surfaces of normal parallel to the z-direction.

In order to take into account both of the objectives, there exist several solutions. The first one is to construct a multi-objective function composed of both objective functions scaled with a weighting factor ω

$$J = \omega J_{\text{Pt}} - (1 - \omega) J_{\text{th}} = \omega_{\text{Pt}} J_{\text{Pt}} - \omega_{\text{th}} J_{\text{th}}. \quad (3.5)$$

$\omega_{\text{Pt}} = \omega$ stands for the weight accorded to the pressure losses and $\omega_{\text{th}} = (1 - \omega)$ is the weight of the thermal flux to the fluid.

In Eq. 3.5, ω, ω_{Pt}, and ω_{th} are all positive. A negative sign is put in front of J_{th} since the heat flux at the outlet has to be maximized. The optimiser is in fact seeking for a minimum. That is why in order to maximise a quantity, a negative sign must be accorded to its respective term in the objective function J.

This first solution does not end with this weighting of the different objective functions. As a matter of fact, J_{Pt} and J_{th} may have completely different orders of magnitude. As a consequence, the objective functions have to be normalised in order to have a well scaled problem and not to have one of the objectives receiving a greater importance than the other one. In order to apply the appropriate normalisation factors, the optimiser does a first optimisation cycle for both objective functions and then the results of this first optimisation cycle, noted $J_{\text{init, Pt}}$ and $J_{\text{init, th}}$, are used as normalisation factors. The weighted and normalised objective function becomes then

$$\widehat{J} = \omega_{\text{Pt}} \frac{J_{\text{Pt}}}{J_{\text{init, Pt}}} - \omega_{\text{th}} \frac{J_{\text{th}}}{J_{\text{init, th}}} = \omega_{\text{Pt}} \widehat{J_{\text{Pt}}} - \omega_{\text{th}} \widehat{J_{\text{th}}}. \quad (3.6)$$

Another solution is to put one of the objectives under a constraint. In that case, only one of the objective functions will be taken into account in J. A practical case would be to consider only J_{th} in J and impose an upper bound on the pressure losses. To do so, an appropriate value should be chosen for this upper bound in order to avoid overestimating or underestimating the constraint.

An additional constraint that is also commonly taken into consideration in CHT problems is the maximum allowable volume that can be occupied by the fluid. This is stated as follows

$$J_{\text{Vol}} = \frac{\int_{\Omega}(1-\beta)\,d\Omega}{\int_{\Omega} d\Omega} \leqslant V_{\text{tar}} \tag{3.7}$$

where $\int_{\Omega}(1-\beta)\,d\Omega$ is the effective volume occupied by the fluid, $\int_{\Omega} d\Omega$ is the total volume of the domain, and V_{tar} is the target (or maximum) volume fraction the fluid can occupy in the domain. A volume constraint is necessary in almost all TO problems in order to prevent the formation of small fluid islands inside solid regions. For the practical example that will be used, $V_{\text{tar}} = \phi^f_{\max} = 0.4$ in Ω_{opt}.

Considering the above cited objective functions and constraint, the CHT TO problem that will be used in this chapter is formulated as follows:

$$\begin{cases} \min\limits_{\alpha} \quad \widehat{J}(\alpha, \mathbf{U}) = \omega_{\text{Pt}}\widehat{J_{\text{Pt}}} - \omega_{\text{th}}\widehat{J_{\text{th}}} \\ \text{s.t.} \quad \phi^f - \phi^f_{\max} \leqslant 0 \\ \qquad 0 \leqslant \alpha_j \leqslant 1 \quad j = 1, ..., N \\ \qquad \mathbf{R}(\alpha, \mathbf{U}) = 0 \end{cases} \tag{3.8}$$

where N the total number of cells which corresponds to the number of design variables, and $\mathbf{R}(\alpha, \mathbf{U}) = 0$ is the system of equations given by Eq. 2.57 to Eq. 2.61.

3.3   Influence of spatial discretisation

In this section, the influence of the spatial discretisation of the domain on the optimised topology will be shown. To do so, two main categories of convergence studies will be introduced. Note that for all of the cases until section 3.8, the initial condition concerning the design field is $\alpha = 0$ in each cell, i.e. the domain is totally filled with fluid initially.

First of all, a convergence study will be performed on a case with no regularisation nor projection. Then, the same type of analysis will be performed with regularisation and projection. These studies will introduce a first insight in the understanding of the regularisation process that will be explained in the following section. The other optimisation parameters are not detailed here as only the effect of the discretisation is assessed in the current section. These will be studied in the upcoming sections.

To perform the analysis, the solution is solved on four different meshes. Then in order to choose the best one in terms of relative error and computational time, the results of these four cases will be compared to a fifth test case made of a very fine mesh that is considered to be valid. The latter is composed of 200×100 cells in Ω_{opt} and 200×20 cells in each inlet and exit channels. The four test cases are summarised in Tab. 3.3.

	Mesh1	Mesh2	Mesh3	Mesh4
N_{cells} in Ω_{opt}	60×30	75×37	100×50	150×75
N_{cells} in Ω_{in}/Ω_{out}	60×6	75×7	100×10	150×15
N_{tot}	2520	3825	7000	15 750

Table 3.3: Test cases for the spatial discretisation.

In each of the test cases, ω_{Pt} is set to 1, and ω_{th} is set to zero. The solutions and the relative errors for regularised and not regularised nor projected design field are shown in Fig. 3.3. In order to have a consistent comparison between the solutions for the regularised and non-regularised results, the same optimisation parameters have been used. These are not detailed here as the effect of these parameters are not studied in this section. A meticulous analysis of these non cited parameters will be done further in the text. The purpose in this section is to assess only the effect of the grid.

The computed heat flux and pressure losses are the same for the regularised and non-regularised solutions. For the third mesh case, the relative error is equal to zero for the heat flux and very low for the pressure losses. That is why it is safe to choose this third mesh case while assuring a low computational cost.
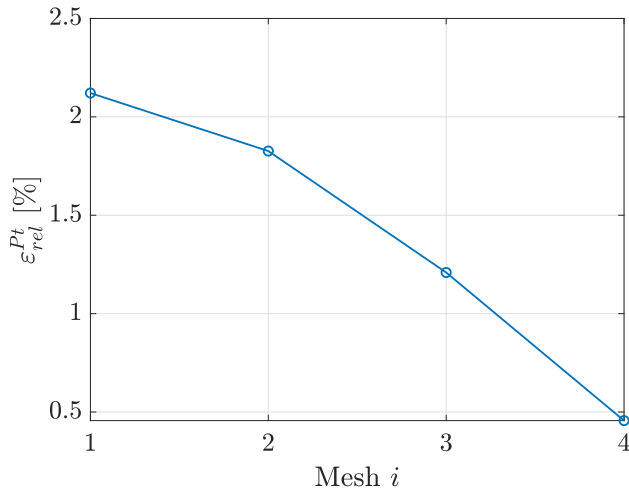
(a) Relative error on the pressure losses.
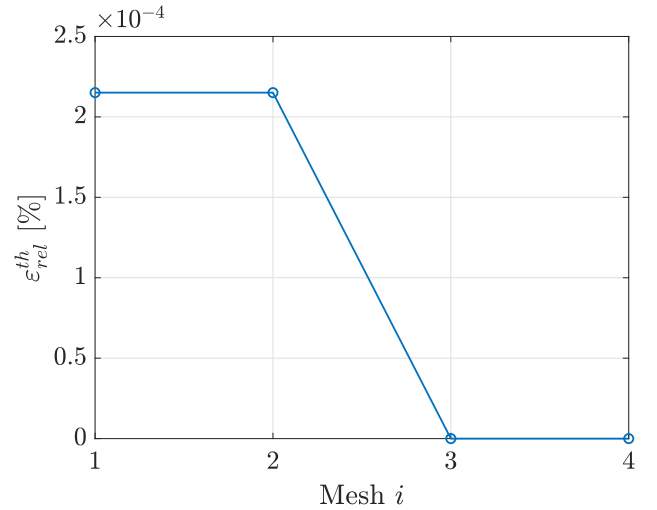
(b) Relative error on the heat flux.

Figure 3.3: Relative error of the regularised and non regularised solutions for the different meshes with respect to the result of a very fine mesh on the heat flux and on the pressure losses.

The topologies obtained for the different cases are shown in Tab. 3.4. An important remark that can be made is that when refining the mesh using no regularisation, the solution captures small features and does not converge. The solution obtained for a non-regularised field has

small voids inside the solid. For the finer mesh 4, this behavior is much more accentuated. In this case, the non-regularised field is not so different in the general topology. The differences with the regularised solutions are not so noted. However, in much complex cases, the absence of regularisation may lead to a more important aspect of the non-convergence of the mesh.

Mesh	Regularised	Non-regularised
1		
2		
3		
4		

Table 3.4: regularised and non-regularised solutions obatined for the different meshes, with $\omega_{\mathrm{Pt}} = 1$ and $\omega_{\mathrm{th}} = 0$.

The conclusion that can be drawn from these observations is that although the computed objectives are converged for the regularised and non-regularised solutions, the obtained β field does not converge when omitting regularisation. Without regularising the design field, the obtained solution will tend toward a different one when refining the mesh, and the convergence will not take place. That is why it is important to perform the regularisation such that the solution is mesh-independent. That represents one of the reasons why regularisation is important in the scope of TO. More specificities related to the regularisation will be provided in the upcoming section.

3.4 Regularisation and projection

In this section, the effect of the regularisation and the projection will be studied by varying their respective parameters.

First of all, the solutions obtained for a regularised nor projected field, and the solution for a regularised but non-projected field are illustrated in Fig. 3.4. The non-regularised and non-projected result (Fig. 3.4a) has a clear transition from fluid to solid regions. This is due to the fact that the penalisation parameter of the blockage interpolation function is high. The latter is a Borrvall and Petersson type interpolation with $q = 10$. These functions will be studied in section 3.5. Moreover, the blurring brought by the regularisation does not take place here, which helps to avoid an unclear transition from fluid to solid parts. However, a small checkerboard effect is observed with fluid cells inside the solid domain. This is due to the absence of regularisation. The regularised but not projected result is shown in Fig. 3.4b. The transition from fluid to solid region is blurred because the regularisation is applied but the projection is omitted.

(a) Not regularised and not projected porosity field.

(b) regularised but not projected porosity field.

0   1

β
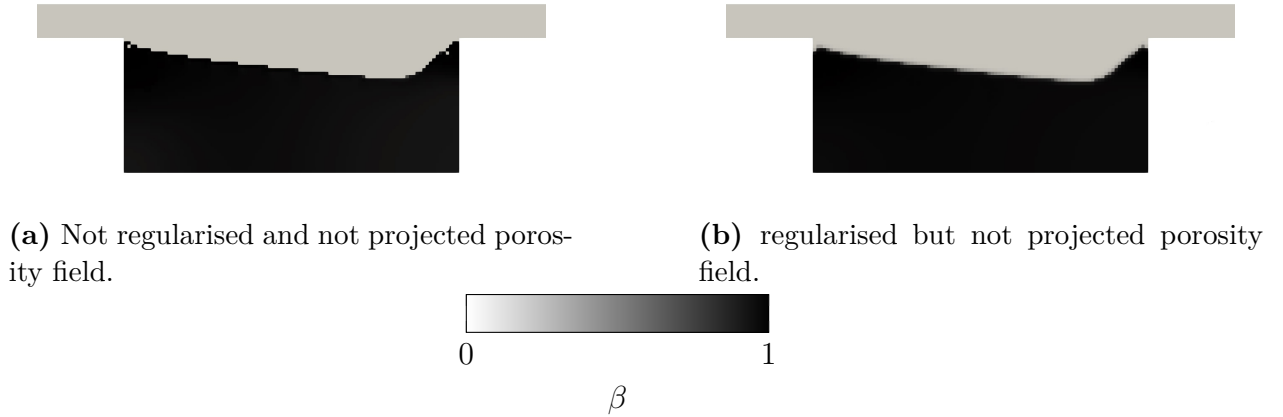
Figure 3.4: Illustration of the impact of the absence of the regularisation and/or projection.

Then, the different parameters of regularisation and projection are studied. These are illustrated in Fig. 3.5, Fig. 3.6, Fig. 3.7, and Fig. 3.8.

In Fig. 3.5, it can be noted that for large radius R of the regularisation filter, the grey zones are present. For these large radius, the sharpening parameter b of the projection is not high enough in order to get rid of this blurry appearance of the solid boundary. Then, the more the radius is decreased, the more precise the separation between the fluid and the solid is. For low values of R, the optimiser is able to generate small features in the solution, leading to the fluid cells in the solid which are not physical.

In Fig. 3.6, a porous zone appear in the right corner of the solidified zone for $R = 2$ mm, and for the last two small radius. This part is not well processed by the projection due to the fact that the value of $\tilde{\alpha}$ is close to 0.5 there and the projection with $b = 10$ keeps this value for the β field. For $R = 4$ mm, the solution has a big difference in the general topology. So the regularisation radius can play a big role in the obtained optimised solution.

Concerning the effect of the projection steepness parameter b, it can be said that for small and moderate values of b, the projection is not sharp, and the obtained β field is not neat and clean in terms of material distribution as it is illustrated in Fig. 3.5 and Fig. 3.6, especially when the regularisation filter radius R is big. From these observations, it can be deduced that b must be high in order to have a sharp distinction between solid and void regions. However, imposing directly a large value for b at the very first optimisation cycles will lead to a solution with almost no solid for which the volume constraint is thus not satisfied. This is observed in Fig. 3.7 where b is constant and set to 30. The explanation for this phenomenon is that at as the problem is relaxed, the design variable α can take intermediate values between zero and one. Therefore, the regularised field $\tilde{\alpha}$ takes also intermediate values between zero and one. Initially, the domain is filled with fluid, i.e. $\alpha = 0$ in each cell. So in the beginning, the value of α is rather close to zero. Also, the maximum allowable change of the design variable α in the course of one optimisation cycle in each cell is set to 0.1 in the software. As a consequence, the projected field β will be equal to zero if a high value is imposed on the steepness parameter b of the projection directly for the first optimisation cycles.
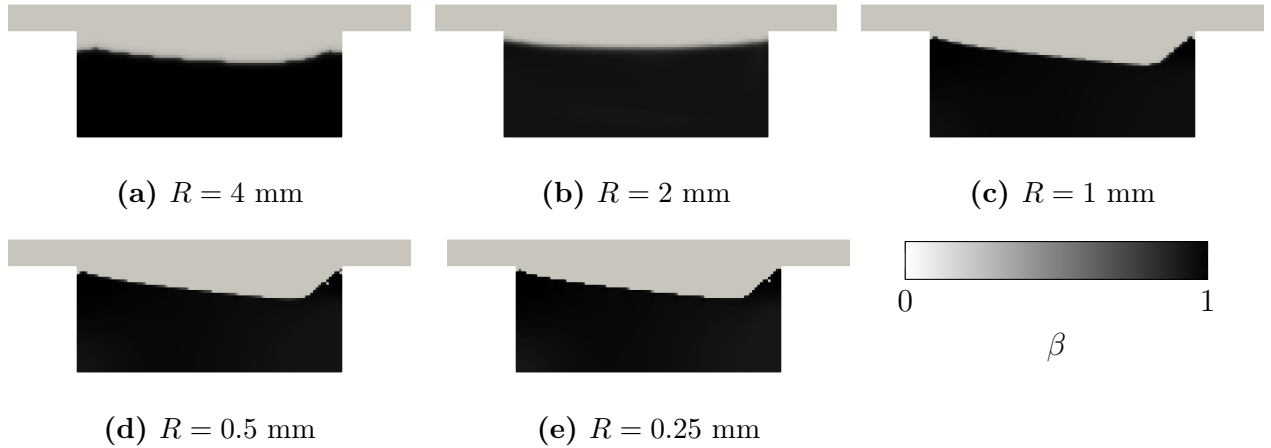
(a) $R = 4$ mm **(b)** $R = 2$ mm **(c)** $R = 1$ mm

(d) $R = 0.5$ mm **(e)** $R = 0.25$ mm

Figure 3.5: β field for different values of the regularisation radius with the projection steepness parameter b equal to 3; $\omega_{\text{Pt}} = 1$, $\omega_{\text{th}} = 0$.
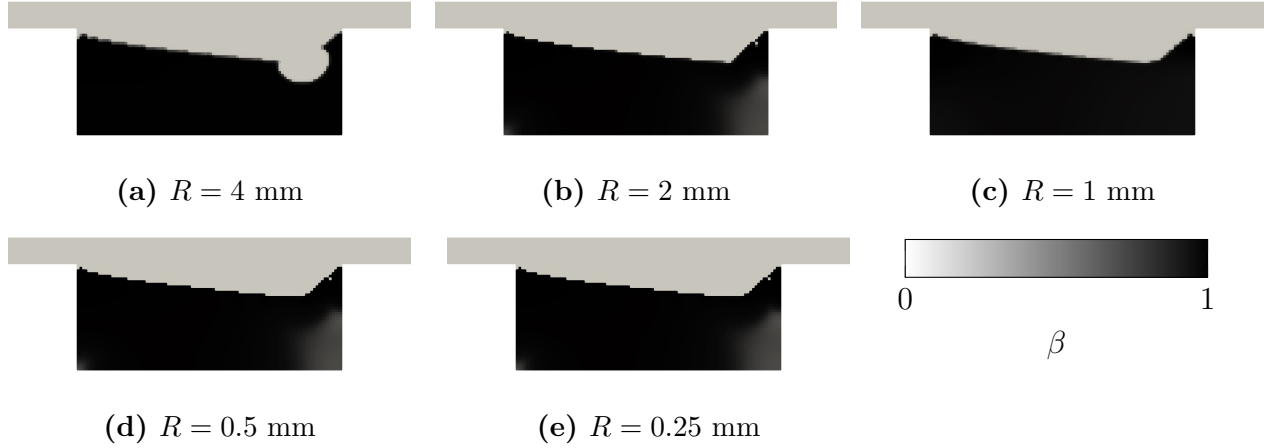
(a) $R = 4$ mm **(b)** $R = 2$ mm **(c)** $R = 1$ mm

(d) $R = 0.5$ mm **(e)** $R = 0.25$ mm

Figure 3.6: β field for different values of the regularisation radius with the projection steepness parameter b equal to 10; $\omega_{\mathrm{Pt}} = 1$, $\omega_{\mathrm{th}} = 0$.

Figure 3.7: β field for different values of the regularisation radius with the projection steepness parameter b equal to 30; $\omega_{\mathrm{Pt}} = 1$, $\omega_{\mathrm{th}} = 0$.

From all these observations, the conclusion is to use an appropriate radius that is small enough in order to prevent the formation of blurred zones but still big enough to avoid the formation of small fluid cells in solid region. But it can be remarked that if the radius has a high value, then the projection can be adapted in order to have a clear material distribution.

Regarding the projection, the conclusion that can be derived from the analysis done here above is that at the very beginning of the optimisation process, the sharpening parameter b should be low enough in order to be able to generate the first solid cells. This allows to find the general topological structure. Then, once the optimiser had enough time to create its blurry material distribution giving a first topology, the parameter b of the projection can become bigger in order to have the final lucid material distribution. This approach is used in the solutions of Fig. 3.8. For these cases, the sharpening parameter varies as a ramp function (Fig. 3.9). In the beginning, b is equal to 3. Then, b is increased by three every two optimisation cycles until it reaches a value of 75 with which the optimisation continues until the end cycle. In the following, this allure of the projection sharpness will be used.
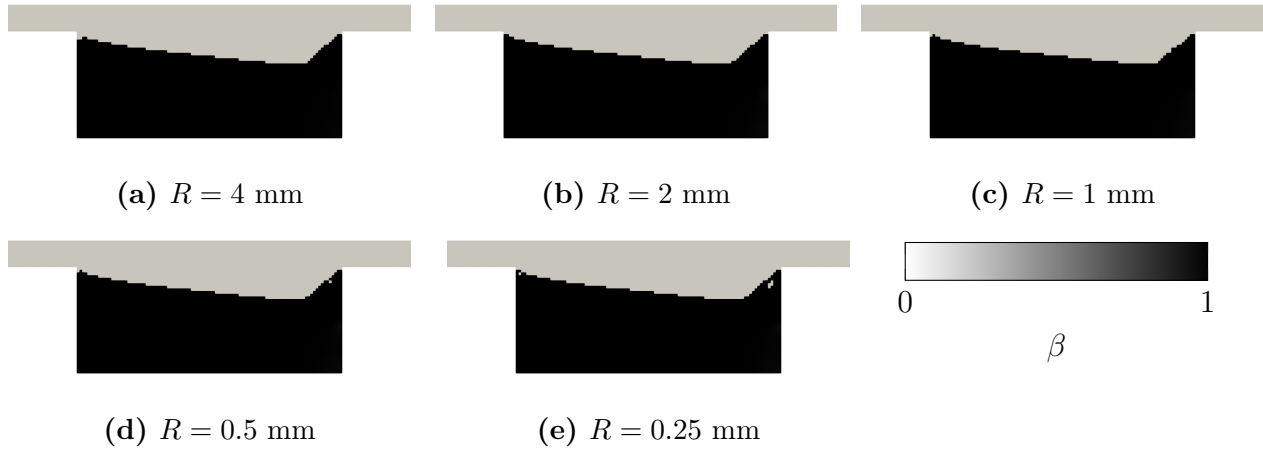
(a) $R = 4$ mm   **(b)** $R = 2$ mm   **(c)** $R = 1$ mm

(d) $R = 0.5$ mm   **(e)** $R = 0.25$ mm

Figure 3.8: β field for different values of the regularisation radius with the projection steepness parameter b varying as a ramp function; $\omega_{\mathrm{Pt}} = 1$, $\omega_{\mathrm{th}} = 0$.
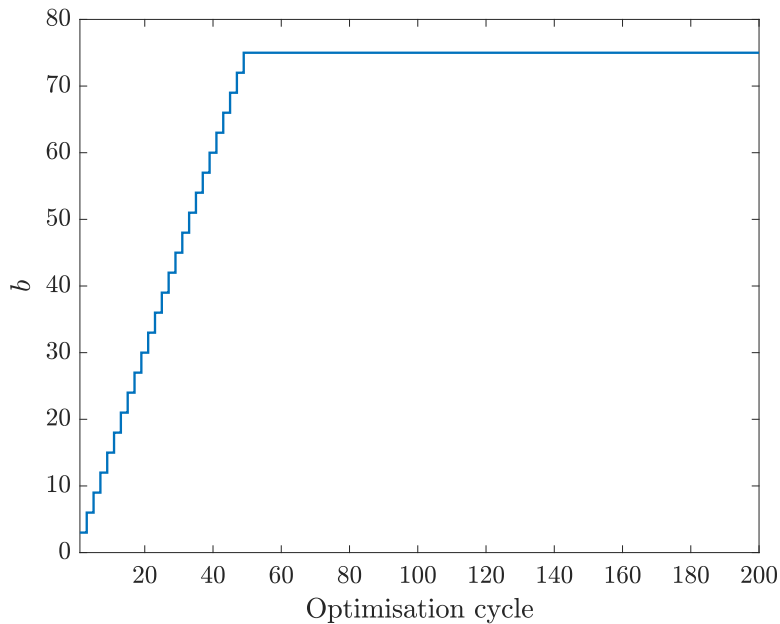
Figure 3.9: Ramp variation of the projection steepness parameter b for the solutions in Fig. 3.8.

3.5 Penalisation term in the flow equations and interpolation of the thermal porperties

As it was explained previously, in order to take into account the presence of solid material immersed in the fluid, a Brinkman type penalisation term is added to the flow equations as a "porosity" source term. This term is composed of the inverse permeability λ proportional

to its maximum value that is then scaled with an interpolation function. The maximum value of λ determines the Darcy number. Proceeding this way, the variation of the inverse permeability can thus be introduced with the value of the design field α. There exist several interpolation functions for this source term. The same type of functions are also used in order to interpolate the thermo-physical properties at each cell depending on the value of the design variable α in the considered cell.

In this section, the influence of the interpolation functions, and the effect of the Darcy number will be assessed. This analysis will then permit to choose the best suited interpolation functions in practical CHT TO problems, and also see how the Darcy number has to be set.

3.5.1 Interpolation of the penalisation term in the flow equations

The Brinkman type penalisation term in the primal equations (Eq. 2.58 to Eq. 2.61) is introduced with the inverse permeability λ that depends on the design field α. This local inverse permeability is related to the design variable though an interpolation function. Ensuing the regularisation and the projection applied on α in each optimisation cycle, this α-dependent source term is written as

$$\lambda(\beta) = \lambda_{\mathrm{max}} I(\beta), \tag{3.9}$$

where $I(\beta)$ is the interpolation function, and λ_{max} is the maximum value of the inverse permeability. The latter should be fixed based on the Darcy number. This will be explained in details later.

There exist several interpolation functions implemented in the software. These are summarised below and their respective graphical illustrations are given in Fig. 3.10.

- **Borrvall and Petersson (BP)**

$$I^{\mathrm{BP}}(\beta) = \frac{\beta}{1 + q(1 - \beta)} \tag{3.10}$$

- **exponential**

$$I^{\mathrm{exp}}(\beta) = \mathrm{e}^{-q(1-\beta)} - [1 - \beta]\mathrm{e}^{-q} \tag{3.11}$$

- **linear**

$$I^{\mathrm{lin}}(\beta) = \beta \tag{3.12}$$

- **SIMP**

$$I^{\mathrm{SIMP}}(\beta) = \beta^q \tag{3.13}$$

- **sinh**

$$I^{\mathrm{sinh}} = 1 - \frac{\sinh[q(1 - \beta)]}{\sinh(q)} \tag{3.14}$$

- **tanh**

$$I^{\mathrm{tanh}}(\beta) = \frac{\tanh(\eta q) + \tanh[q(\beta - \eta)]}{\tanh(\eta q) + \tanh[q(1 - \eta)]} \tag{3.15}$$
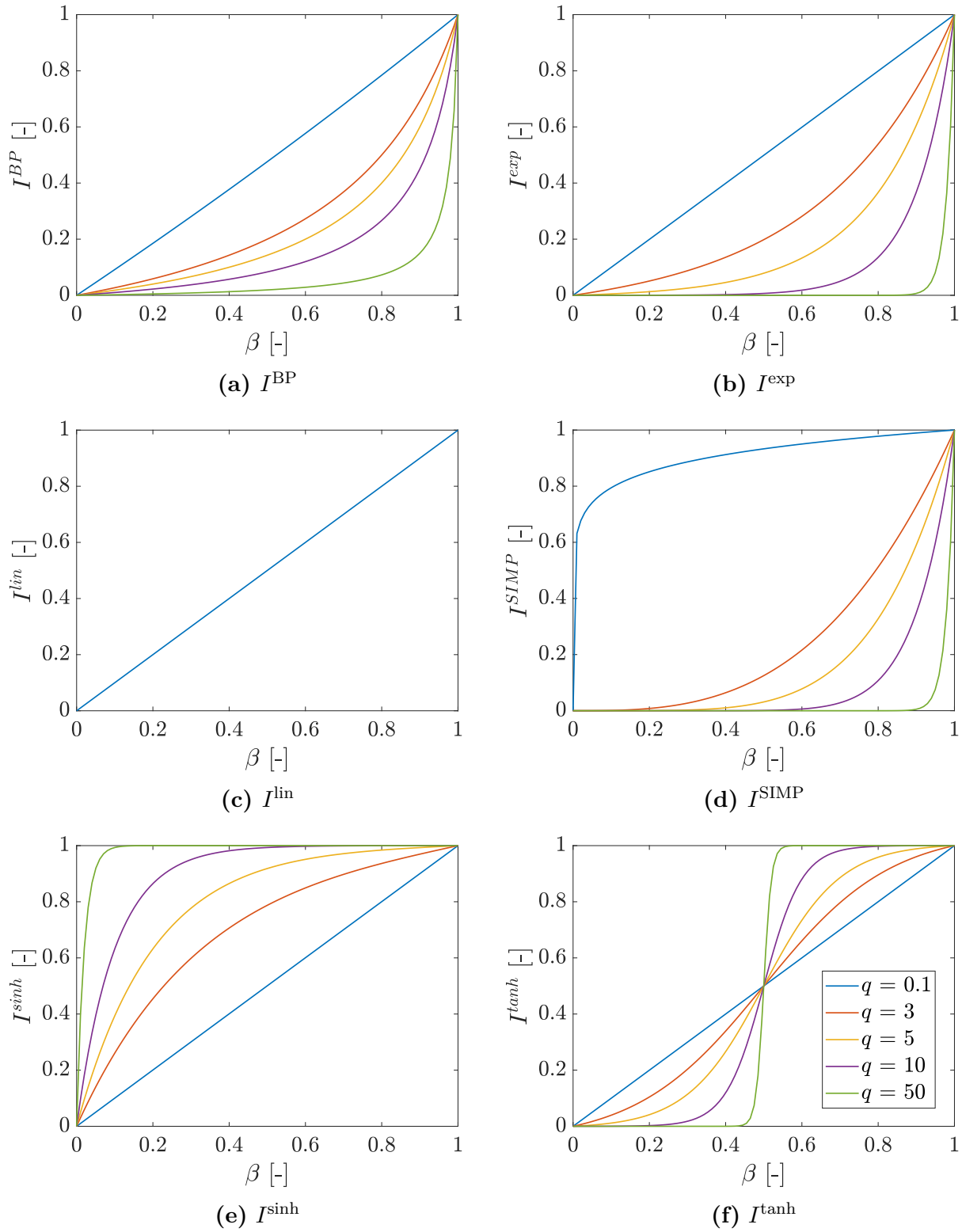
Figure 3.10: Interpolation functions.

When β is equal to one, which corresponds to a solid, each of these functions are equal to

49

one. Then, λ is equal to λ_{max}, so the inverse permeability is at its maximum value, meaning that the permeability tends to zero, and thus this blocks the flow. This can also be understood by considering the impact of the value of λ in the moment equation (Eq. 2.44). When $\lambda(\beta) = \lambda(1) = \lambda_{\mathrm{max}}$, the flow velocity must tend to zero in order to verify the equation.

The parameter q in the interpolation functions controls the steepness of the functions with respect to β. This is illustrated in Fig. 3.10. q [-] can in fact be seen as a penalisation factor. The greater is the value of q, the more penalised are the grey zones. Therefore, in order to have a "binary" material distribution, the value of q should be high enough.

The topologies obtained for the different interpolation functions, fixing the weight of the pressure losses to one and the weight of the heat flux to zero, are shown in Fig. 3.11. For each case, the regularisation radius has been set to 1 mm. This value is obtained based on the average cell volume as it is expressed in Eq. 2.69. The solutions acquired with the SIMP, and tanh interpolations are not regular as the other ones. The convergence history obtained for the different interpolation functions are shown in Fig. A.1. Except the BP and exponential interpolation functions, the convergence of the solutions given by the other functions is very bad. Comparing the solutions of Fig. 3.11a and Fig. 3.11b and their respective values of J_{Pt} (Tab. 3.5) which was the only objective function to minimise, it seems better to chose the BP interpolation function for the porosity source term, which is commonly used in fluid-based TO. In the following, the BP interpolation function is thus used for the Brinkmann penalisation with $q = 10$.

(a) $I = I^{\mathrm{BP}}$ (b) $I = I^{\mathrm{exp}}$ (c) $I = I^{\mathrm{lin}}$

(d) $I = I^{\mathrm{SIMP}}$ (e) $I = I^{\mathrm{sinh}}$ (f) $I = I^{\mathrm{tanh}}$

0 1

β
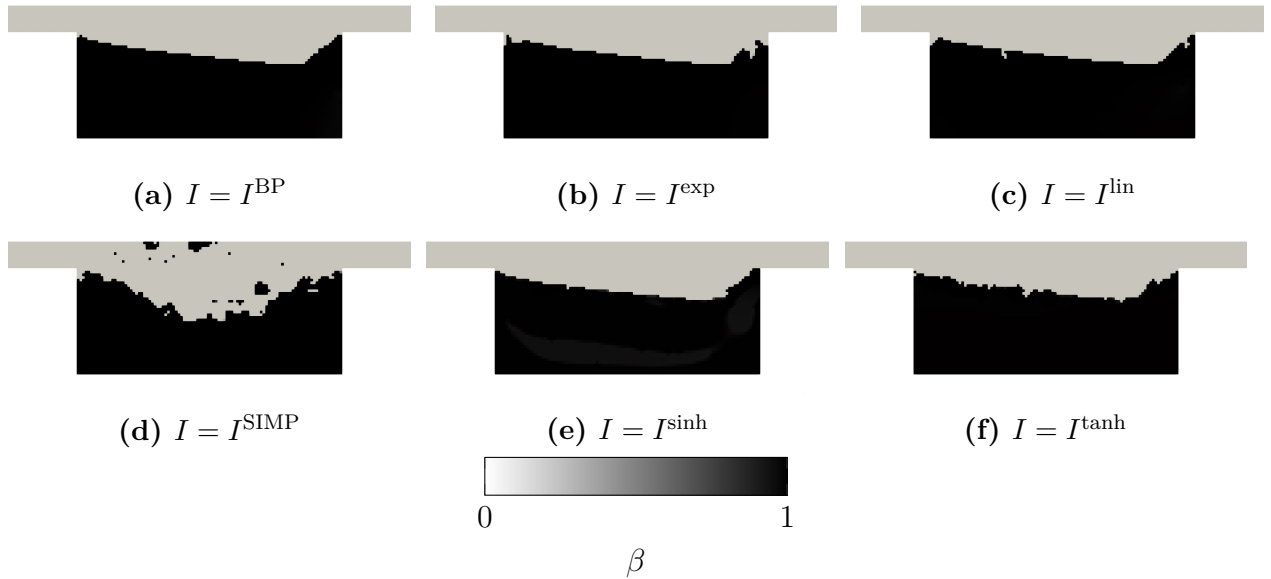
Figure 3.11: Solution for different interpolation functions for the porosity dependent source terms with $q = 10$; $R = 1$ mm; $\omega_{\mathrm{Pt}} = 1$, $\omega_{\mathrm{th}} = 0$.

I	I^{BP}	I^{exp}
J_{Pt} $[\mathrm{m}^5/\mathrm{s}^3]$	2.487×10^{-6}	2.489×10^{-6}

Table 3.5: J_{Pt} for BP and exponential interpolation functions used in the porosity dependent source term with $q = 10$; $R = 1$ mm; $\omega_{\mathrm{Pt}} = 1$, $\omega_{\mathrm{th}} = 0$.

3.5.2 Interpolation of the thermo-physical properties between the fluid and the solid regions

The analysis is now performed regarding the interpolation of the thermo-physical properties for the same weights accorded to both objective functions. The interpolation of the conductivity k between the fluid and the solid is done as follows

$$k(\beta) = k^f + (k^s - k^f)I^k(\beta). \tag{3.16}$$

The same approach is used for the other thermo-physical properties. The type of interpolation functions used for these properties are the same as for the porosity source term (see section 3.5.1) except that the parameter q is replaced by q^{th} [-] which has the same effect as q.

Considering the different interpolation functions, the obtained solutions for $\omega_{\mathrm{Pt}} = 0.5 = \omega_{\mathrm{th}} = 0.5$ with $q^{th} = 5$ and $R = 1$ mm are shown in Fig. 3.12. The optimised material distributions are of poor quality for each of the interpolation functions of the thermal properties. On top of that, the convergence is also very bad (Fig. A.2). Analysing Fig. 3.12, it can be noted that the optimiser is able to generate very small details in the topology, and especially small checkerboard regions. From this observation, it can be deduced that the regularisation radius is small in this case. The radius R must be increased in order to avoid this irregularity in the solution. In light of these remarks, it can be concluded that when the weight of the thermal objective function is non zero, the regularisation radius must be higher than the one calculated based on the average cell volume (Eq. 2.69).

(a) $I = I^{\mathrm{BP}}$ — **(b)** $I = I^{\mathrm{exp}}$ — **(c)** $I = I^{\mathrm{lin}}$

(d) $I = I^{\mathrm{SIMP}}$ — **(e)** $I = I^{\mathrm{sinh}}$ — **(f)** $I = I^{\mathrm{tanh}}$

0 — β — 1
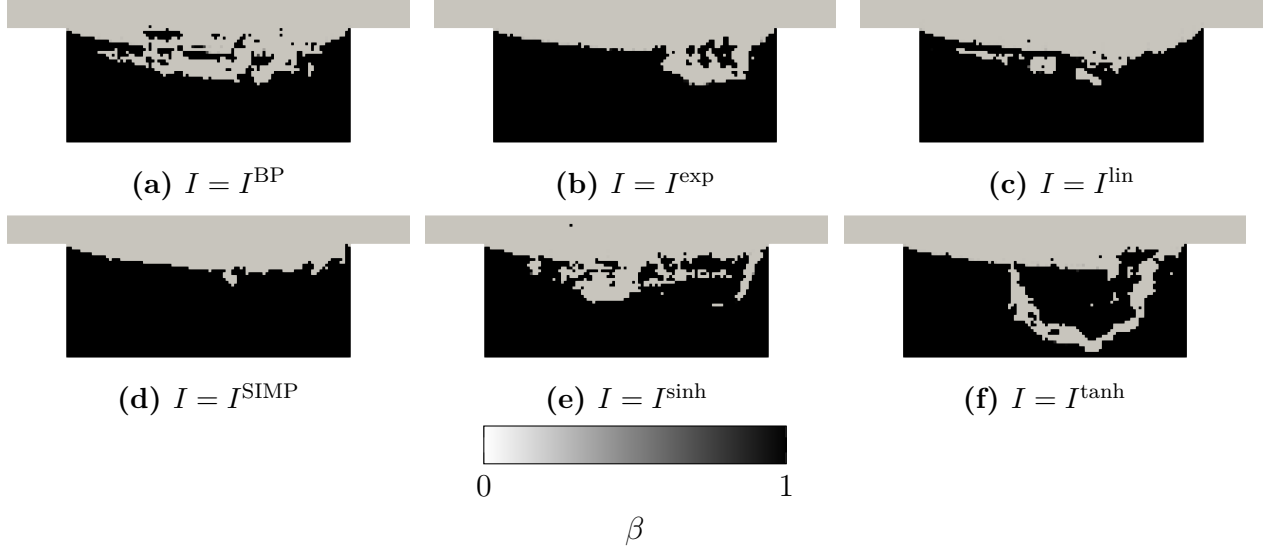
Figure 3.12: Solution for different interpolation functions of the thermo-physical properties with $q^{th} = 5$; $R = 1$ mm; $\omega_{\mathrm{Pt}} = 0.5$, $\omega_{\mathrm{th}} = 0.5$.

(a) $I = I^{\mathrm{BP}}$ — **(b)** $I = I^{\mathrm{exp}}$ — **(c)** $I = I^{\mathrm{lin}}$

(d) $I = I^{\mathrm{SIMP}}$ — **(e)** $I = I^{\mathrm{sinh}}$ — **(f)** $I = I^{\mathrm{tanh}}$

0 — β — 1
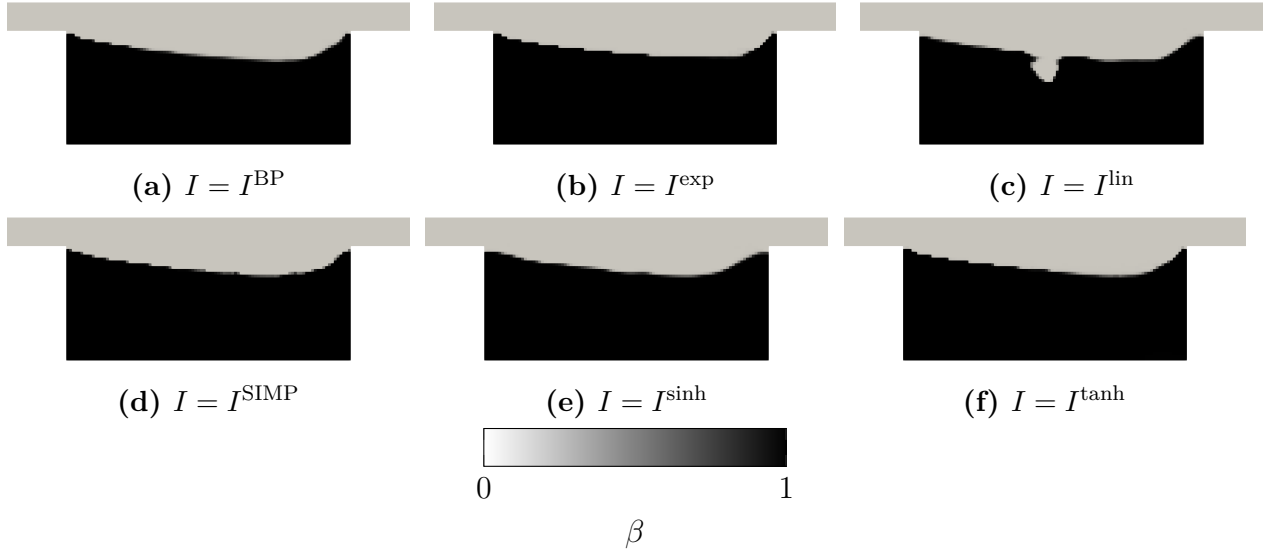
Figure 3.13: Solution for different interpolation functions of the thermo-physical properties with $q^{th} = 5$; $R = 10$ mm; $\omega_{\mathrm{Pt}} = 0.5$, $\omega_{\mathrm{th}} = 0.5$.

This increased radius is used for the cases of Fig.3.13 with $R = 10$ mm. The optimised topologies are very similar except for the linear interpolation of the thermo-physical properties. Regarding their respective convergence (Fig. A.3), there are remarked oscillations of the solution for the BP, linear, and sinusoidal interpolations. These oscillations are drastically reduced but still present in the tangential and exponential interpolations. The SIMP interpolation seems to be the best suited function. Therefore, the SIMP interpolation is used for the interpolation of the thermal properties with $q^{\mathrm{th}} = 5$.

In the following, the BP interpolation function with $q = 10$ will be used for the porosity sourc eterm interpolation, and the thermo-physical properties will be interpolated with the SIMP function with $q^{\text{th}} = 5$.

3.5.3 Effect of the Darcy number

The Darcy number is an important quantity that intervenes through the maximum value of the inverse permeability λ. The Darcy number is defined as

$$Da = \frac{\nu}{\lambda_{\max}L^2} \tag{3.17}$$

where L [m] is the characteristic length of the problem. Da describes the ratio between viscous and porous friction forces. It must be small enough in order to generate almost solid impermeable walls. This in ensured with the high value of $\lambda_{\max}$. The higher is $\lambda_{\max}$, the less permeable are the walls. If $\lambda_{\max}$ is low, then flow will diffuse through the porous media. In contrast, if $\lambda_{\max}$ is high, then solid walls with almost no flow through them will be induced. However, a very high value of $\lambda_{\max}$ will lead to slow convergence of the optimisation process and sub-optimal solutions [58]. So there is a compromise to do in order to choose well the value of $\lambda_{\max}$. This choice is based on Da.

The solution obtained for different values of Da is shown in Fig. 3.6 for $\omega_{\text{Pt}} = \omega_{\text{th}} = 0.5$. Note that only the porous medium of the domain is highlighted in each of the figures in the third right column of Fig. 3.6. This was done thanks to the extraction of the cells with a minimum value of β equal to 0.5. In Fig. 3.6, it can be noted that the higher Da is, the more flow leakage happens in the material distribution. This phenomenon almost ends for $Da \lesssim 10^{-3}$. Also, the changes in the solution are remarkable when going only from $Da = 10^{-1}$ to $Da = 10^{-2}$. In order to be sure to have no leakage and to avoid at the same time convergence problems, Da is set to 10^{-4}.

Da [-]	Material distribution	Leakage in solidified zone
10^{-1}		
10^{-2}		
10^{-3}		
10^{-4}		
10^{-5}		

β : 0 — 1

$|U|$ [m/s] $\cdot 10^{-2}$: 0 — 2
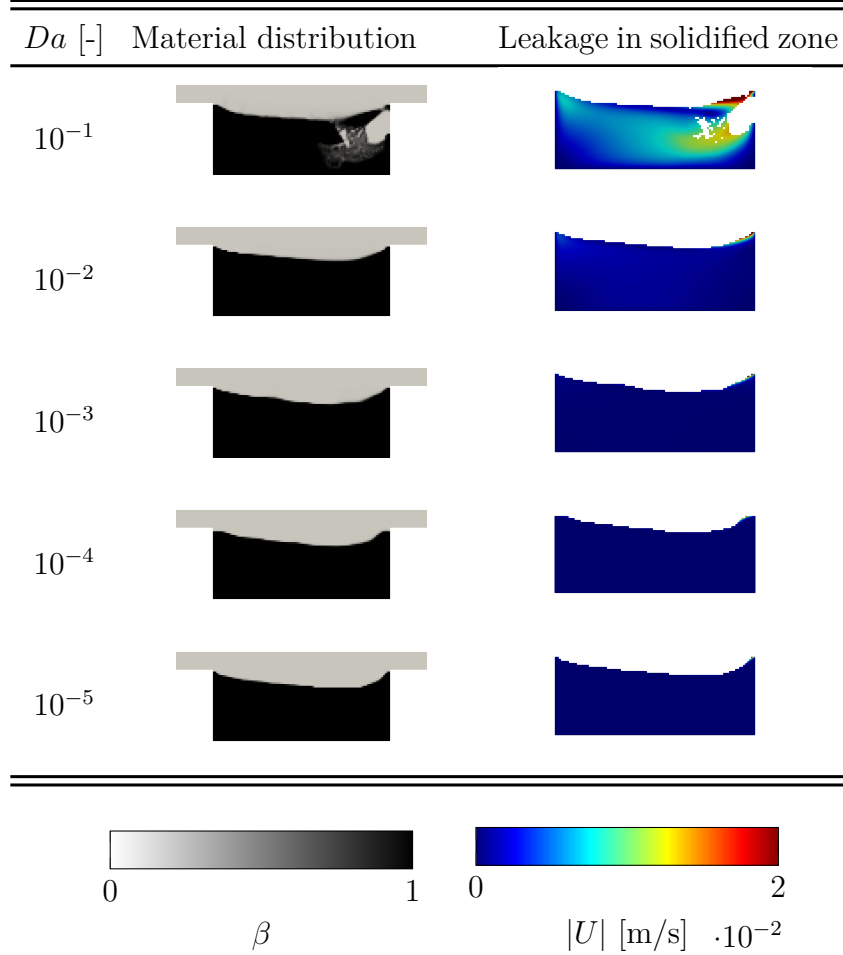
Table 3.6: Effect of the Darcy number on the permeability of the solidified part of the domain; $R = 10$ mm; $\omega_{\mathrm{Pt}} = \omega_{\mathrm{th}} = 0.5$.

3.6 ATC models

The ATC term is the first term of the adjoint momentum equation. For the component u_i of the adjoint velocity, it is written as

$$\mathrm{ATC}_i^u = u_j \frac{\partial v_j}{\partial x_i}.$$

where the primal components of the velocity v_j are known a priori thanks to the resolution of the primal equations.

The ATC term is numerically stiff. It causes in fact a coupling between the different adjoint momentum equations. There exist several models for the ATC term. These are listed hereafter:

- **Standard**
  This option computes the adjoint transpose convection as it is without any modifici-

ation. So the cross-coupling between the adjoint momentum equations is taken into consideration.

- **UaGradU**
  This model computes the ATC term as $-v_j \frac{\partial u_j}{\partial x_i}$.

- **Cancel**
  In this case, the ATC term is completely deleted from the equations.

The solutions obtained for the three models and their corresponding values of the objective functions with $\omega_{\text{Pt}} = \omega_{\text{th}} = 0.5$ are shown in Fig. 3.14 and Tab. 3.7. The number of iterations needed to solve the adjoint equations in each optimisation cycle is represented in Fig. 3.15.

(a) Standard.   **(b)** UaGradU.   **(c)** Cancel.

$$0 \qquad\qquad\qquad 1$$

$$\beta$$
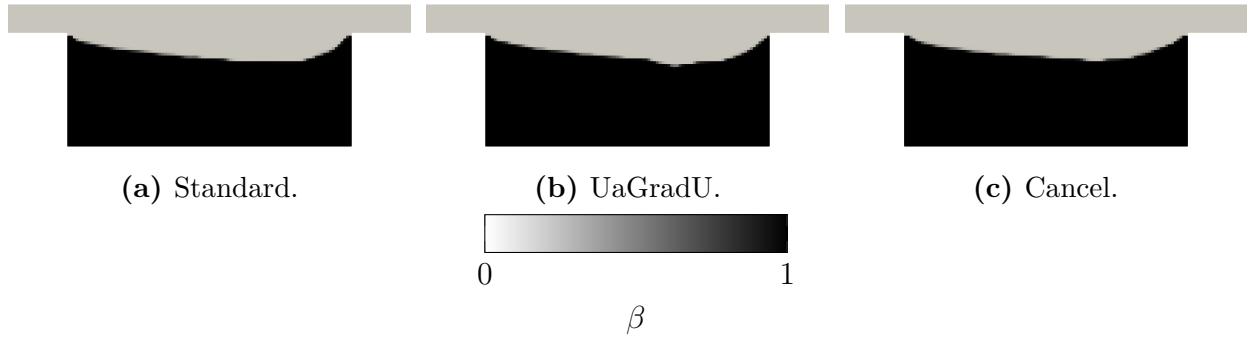
Figure 3.14: Solutions obtained for the different ATC models; $\omega_{\text{Pt}} = \omega_{\text{th}} = 0.5$.

	J_{Pt} [m^5/s^3]	J_{th} [W]
Standard	2.495e-6	43.55
UaGradU	2.503e-6	43.682
Cancel	2.501e-6	43.703

Table 3.7: Pressure losses between the inlet and the outlet, and heat flux at the outlet obtained for the three ATC models.

Regarding the material distribution in Fig. 3.14, it can be pointed out that the different models give very close solutions. As a consequence, the computed heat flux and pressure losses are then very close for the different options.

The difference between the models can be highlighted with the number of iterations needed in each optimisation cycle to solve the adjoint moment equations. In Fig. 3.15, it can be observed that the *Cancel* option needs much less iterations. Then, the number of iterations increases for the two other models. In average, the *Cancel* model needs 110 iterations, the *UaGradU* modle needs 118 iterations, and the *Standard* model needs 127 iterations. From this, it can be concluded that the *Cancel* model could be a good option in order to have

a faster simulation. However, the effect of the ATC on a given problem may be very case dependent. That is why even if in this case the ATC model does not play a big role, in other applications it may be safer if the ATC term is taken into consideration in its standard form.
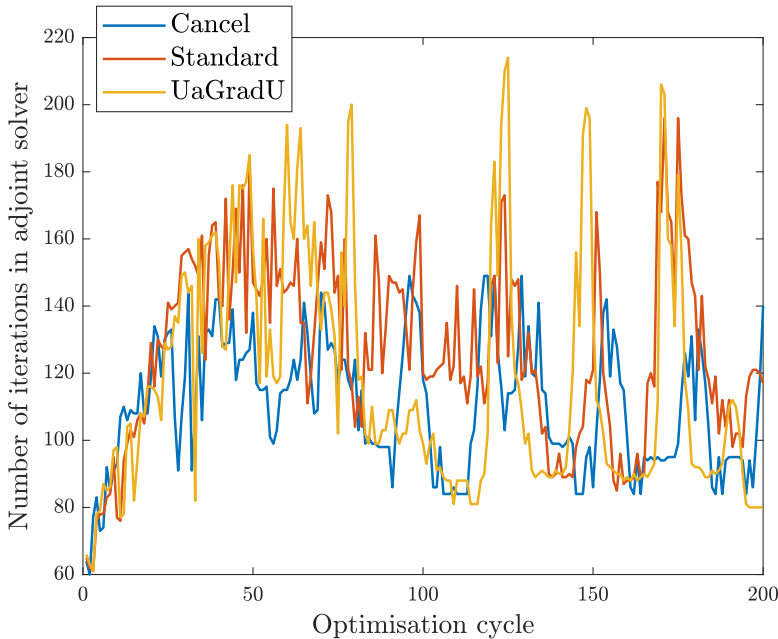
Figure 3.15: Number of iterations to solve the adjoint equations in each optimisation cycle.

3.7   Comparison between *topO* and *dynamicTopO*

There exist two procedures of updating the design variable α in each cell. The first one consists in a process in which all the cells see their design variable updated simultaneously starting from the first optimisation cycle. This corresponds to the *topO* rule. In contrast to this technique, the design variables can be updated dynamically. This is done with the *dynamicTopO* update rule. In this approach, the active cells and the marching step coefficient (MSC) must be defined. The active cells are the first cells whose design variable is updated in the first optimisation cycle. Then, in the next optimisation cycle, the zone of active cells grows with the next neighbouring cells. If the MSC is set to one, the zone expands with the direct neighbours. If it is set to two, then the active cells enlarge with the direct next cells and their neighbours. From these aspects of the two methods, it can be presumed that in TO problems that could be complex and lead to an unstable optimisation process, it could be advantageous to use the second method in order to stabilise the optimisation.

The optimised topologies for the *topO* and *dynamicTopO* options for $R = 10$ mm, and $\omega_{\text{Pt}} = \omega_{\text{th}} = 0.5$ are presented in Fig. 3.16 together with the respective values of the objective functions in Tab. 3.8. The optimised topologies are very similar. It follows from these solutions values for the objective functions that are very close to each other.

Figure 3.16: Solutions obtained with *topO* and *dynamicTopO* with a marching step coefficient of 1 for $R = 10$ mm; $\omega_{Pt} = \omega_{th} = 0.5$.

Update technique	J_{Pt} [m⁵/s³]	J_{th} [W]
topO	2.488×10^{-6}	42.962
dynamicTopO	2.490×10^{-6}	43

Table 3.8: Values of the objective functions for *topO* and *dynamicTopO* update rules with a marching step coefficient of 1 for $R = 10$ mm; $\omega_{Pt} = \omega_{th} = 0.5$.

As it has been noted in section 3.5, when according a non zero weight to the thermal objective function J_{th}, the regularisation radius must be set higher than the one predicted by Eq. 2.69 with the average cell volume. Nevertheless, using this small radius $R = 1$ mm with the *dynamicTopO* update rule, it may be possible to generate an optimised topology that could be interesting. This has been tried on three cases with different marching step coefficients (Fig. 3.17). With MSC = 1, the material distribution is not so original, and on top of that the fluid volume fraction does not verify the volume constraint (ϕ^f - $\phi^f_{max} = 0.5 > 0$). The topology with MSC = 5 is weird with a big void inside the solidified zone. The curious solution obtained with MSC = 3 displays a motivation in order to use the *dynamicTopO* update rule. This solution gives an enhanced heat transfer to the fluid compared to the *topO* update (see Tab. 3.9 and Tab. 3.8), but at the expense of a little increase in the pressure losses. With MSC = 3, the fluid tends to be closer to the heated wall compared to the cases in Fig. 3.16 in which the solid material distribution takes over the fluid close to the heated wall. So the heat is first mainly transferred by conduction through the solid material distribution, and then to the fluid that is not close to the heated lower wall.

(a) MSC = 1. (b) MSC = 3. (c) MSC = 5.
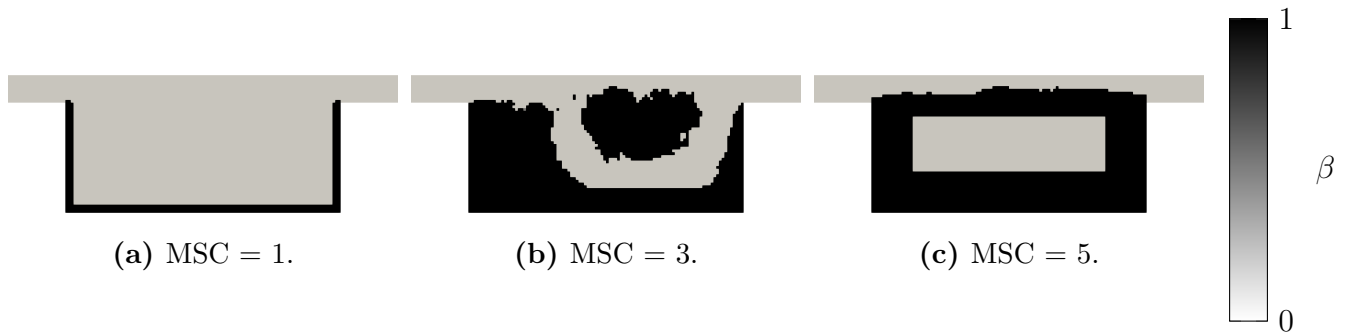
Figure 3.17: Solutions obtained with *dynamicTopO* updating for $R = 1$ mm, and different marching step coefficients; $\omega_{Pt} = \omega_{th} = 0.5$.

MSC	J_{Pt} [m^5/s^3]	J_{th} [W]
1	2.628×10^{-6}	42.99
3	2.603×10^{-6}	43.188
5	8.234×10^{-6}	45.407

Table 3.9: Values of the objective functions for the *dynamicTopO* update rules with different marching step coefficients for R $= 1$ mm; $\omega_{\mathrm{Pt}} = \omega_{\mathrm{th}} = 0.5$

From all of these analysis, it can be concluded that the use of the two different update rules results in the same topologies when using a high radius of regularisation. Reducing this radius on cases with different marching step coefficients when employing the *dynamicTopO* rule gives very dissimilar solutions. This behaviour shows again the high sensitivity of the optimiser to its imposed parameters. In the following, the *topO* update rule will be used.

3.8 Influence of the initial conditions and the weighting parameters

In this section, the effect of the initial conditions (IC) together with the weight accorded to the different functions will be analysed. Two different settings will be studied. The first one (IC1) considers the domain initially filled with fluid, i.e. $\alpha = 0$ in each cell. For the second case (IC2), the domain is fluid everywhere except in a box centered in the middle of the square box where α is initially set to one. The two types of initial conditions are illustrated in Fig. 3.18. In Fig. 3.18b, the solid region corresponds to the black rectangle where $\alpha = 1$, whereas fluid regions are represented in white with $\alpha = 0$.

The solutions and the average outlet temperature $\overline{T}_{\mathrm{out}}$ for IC1 and IC2 for different value of the weighting parameter ω are given in Tab. 3.11. These solutions are all obtained with the *topO* update rule with a regularisation radius equal to 10 mm, a projection steepness parameter evolving as shown in Fig. 3.9. The interpolation functions are a BP function for the porosity source term with $q = 10$, and a SIMP interpolation for the thermo-physical properties with $q^{th} = 5$.

(a) IC1.

(b) IC2.
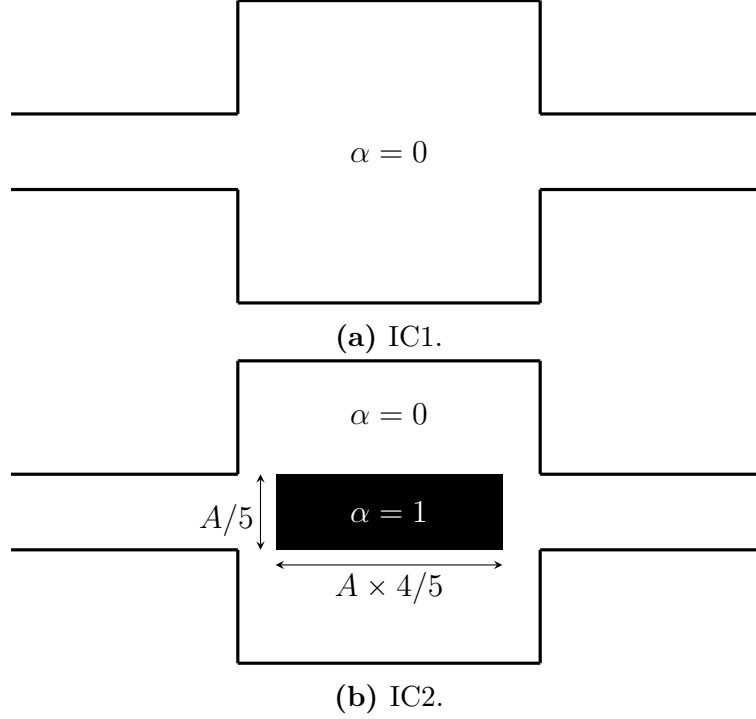
Figure 3.18: Setting of the initial conditions for the two cases (IC1 and IC2).

Weighting factors [-]	IC1			IC2		
	J_{th} [W]	$\overline{T}_{\text{out}}$ [K]	J_{Pt} [m^5/s^3]	J_{th} [W]	$\overline{T}_{\text{out}}$ [K]	J_{Pt} [m^5/s^3]
$\omega_{\text{Pt}} = 0.9$, $\omega_{\text{th}} = 0.1$	42.908	392.223	3.65e-6	42.954	392.647	2.489e-6
$\omega_{\text{Pt}} = 0.8$, $\omega_{\text{th}} = 0.2$	42.919	392.326	3.65e-6	42.992	392.989	2.489e-6
$\omega_{\text{Pt}} = 0.7$, $\omega_{\text{th}} = 0.3$	42.945	392.566	3.65e-6	43.945	401.698	3.393e-6
$\omega_{\text{Pt}} = 0.5$, $\omega_{\text{th}} = 0.5$	42.962	387.72	3.65e-6	44.122	403.324	3.653e-6
$\omega_{\text{Pt}} = 0.4$, $\omega_{\text{th}} = 0.6$	42.973	393.818	3.65e-6	44.23	404.311	3.88e-6
$\omega_{\text{Pt}} = 0.3$, $\omega_{\text{th}} = 0.7$	43.123	394.192	3.66e-6	44.5836	407.539	4.541e-6
$\omega_{\text{Pt}} = 0.1$, $\omega_{\text{th}} = 0.9$	43.301	395.815	3.68e-6	45.038	411.698	7.404e-6
$\omega_{\text{Pt}} = 0.01$, $\omega_{\text{th}} = 0.99$	46.4235	424.364	1.52e-5	46.47	424.787	1.25e-4

Table 3.10: Values of the objective functions for different initial conditions (IC1 and IC2) and different weighting factors.

Weighting factors [-]	Optimised topology of IC1	Optimised topology of IC2
$\omega_{\mathrm{Pt}} = 0.9,\ \omega_{\mathrm{th}} = (1 - \omega_{\mathrm{Pt}}) = 0.1$		
$\omega_{\mathrm{Pt}} = 0.8,\ \omega_{\mathrm{th}} = (1 - \omega_{\mathrm{Pt}}) = 0.2$		
$\omega_{\mathrm{Pt}} = 0.7,\ \omega_{\mathrm{th}} = (1 - \omega_{\mathrm{Pt}}) = 0.3$		
$\omega_{\mathrm{Pt}} = 0.5,\ \omega_{\mathrm{th}} = (1 - \omega_{\mathrm{Pt}}) = 0.5$		
$\omega_{\mathrm{Pt}} = 0.4,\ \omega_{\mathrm{th}} = (1 - \omega_{\mathrm{Pt}}) = 0.6$		
$\omega_{\mathrm{Pt}} = 0.3,\ \omega_{\mathrm{th}} = (1 - \omega_{\mathrm{Pt}}) = 0.7$		
$\omega_{\mathrm{Pt}} = 0.1,\ \omega_{\mathrm{th}} = (1 - \omega_{\mathrm{Pt}}) = 0.9$		
$\omega_{\mathrm{Pt}} = 0.01,\ \omega_{\mathrm{th}} = (1 - \omega_{\mathrm{Pt}}) = 0.99$		

$$
\begin{array}{ccc}
0 \quad\quad 1 & 0 \quad\quad 0.2 & 375 \quad\quad 425 \\
\beta & |U|\ [\mathrm{m/s}] & T\ [\mathrm{K}]
\end{array}
$$
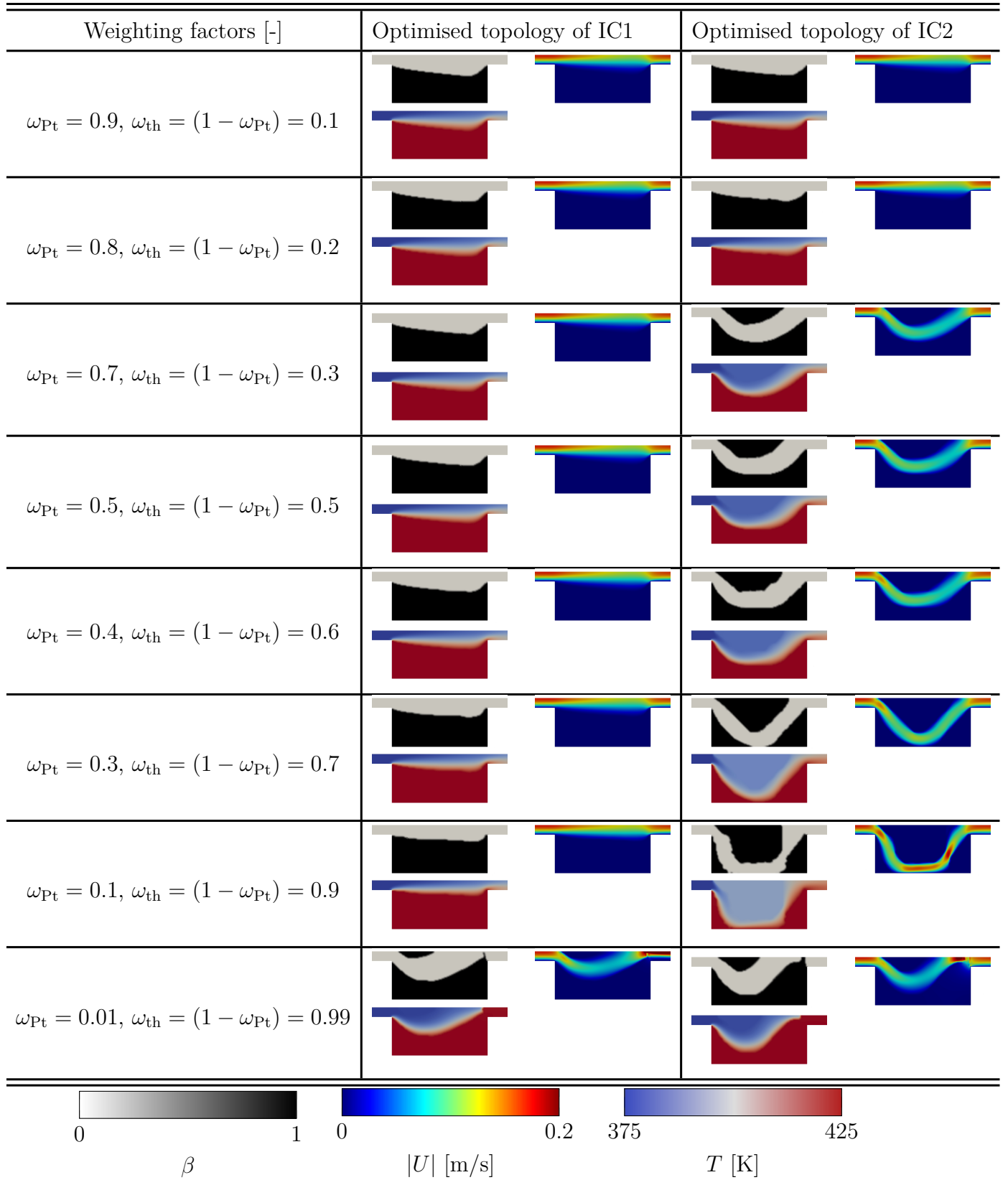
Table 3.11: Optimised topologies obtained for different initial conditions (IC1 and IC2) and different weighting factors.

In order to see well how the topology has been optimised, the Pareto front corresponding to both IC1 and IC2 has been constructed based on the initial values of J_{Pt} and J_{th}. The latter are noted $J_{\text{Pt,init}}$ and $J_{\text{th,init}}$. As a reminder, these are used in order to normalise the objective functions which gives $\hat{J}$. The values of $J_{\text{Pt,init}}$ and $J_{\text{th,init}}$ for IC1 and IC2 are provided in Tab. 3.12 and the Pareto fronts are given in Fig. 3.19 and Fig. 3.20. The couple $(J_{\text{Pt}}/J_{Pt,\text{init}}, J_{\text{th}}/J_{\text{th,init}})$ has been omitted for $\omega_{\text{th}} = 0.99 = (1 - \omega_{\text{Pt}})$. The latter for these weights corresponding to IC1 and IC2 is respectively equal to (5.555, 1.113) and (11.69, 1.096). Analysing the Pareto fronts, it can be noted that the heat flux to the coolant fluid is well increased, and the pressure losses are decreased. For both IC1 and IC2 solutions, the heat flux is almost tripled at the outlet, and the pressure losses are drastically decreased.

	$J_{\text{Pt,init}}$ $[\text{m}^5/\text{s}^3]$	$J_{\text{th,init}}$ $[\text{W}]$
IC1	1.279×10^{-4}	15.351
IC2	1.4216×10^{-4}	15.416

Table 3.12: Initial values of the objective functions for IC1 and IC2.
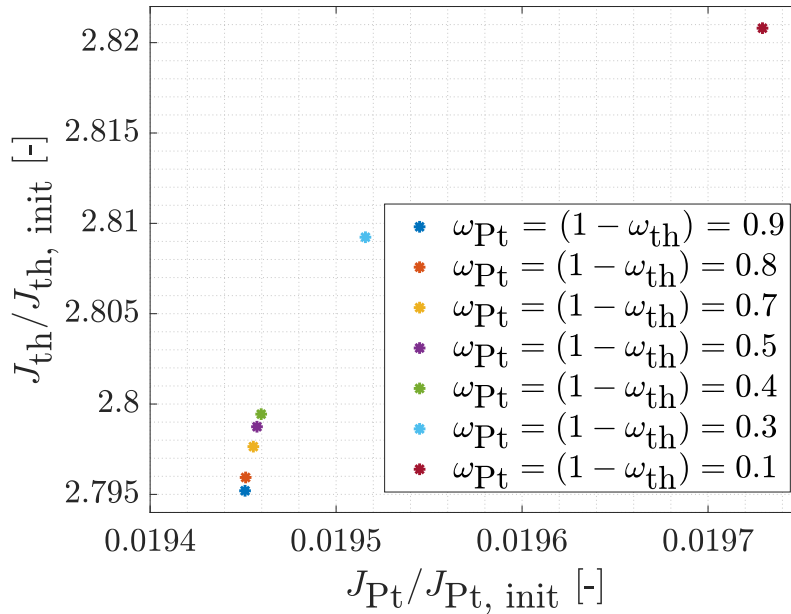
Figure 3.19: Pareto front of IC1.
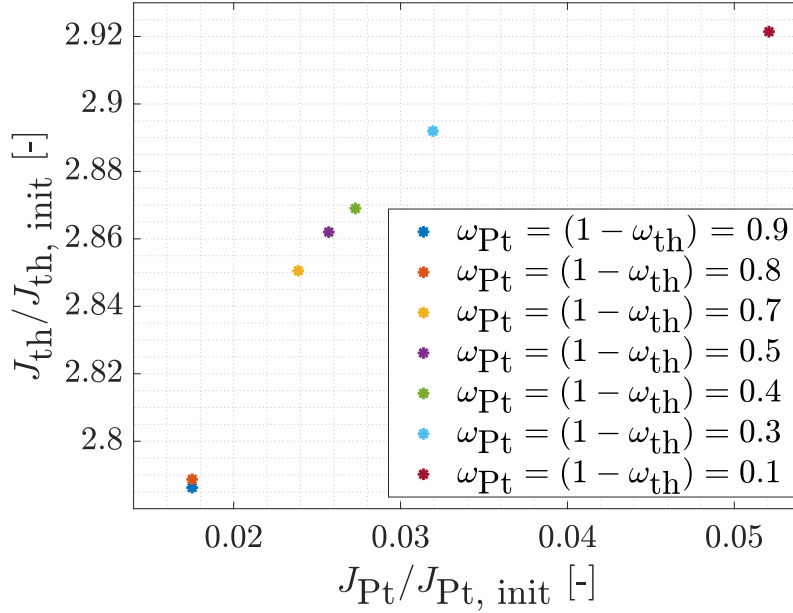
Figure 3.20: Pareto front of IC2.

It is not specified in Tab. 3.11, but the volume constraint is satisfied for all of the solutions of IC1 and IC2. Both IC1 and IC2 do not initially satisfy the volume constraint. But thanks to the dual approach used for the optimality conditions (see section 2.2.3), the generated optimised topologies verify the volume constraint. This figures the power of the method.

Upon increasing the weight accorded to J_{th}, and thus decreasing ω_{Pt}, the solution gets more and more different.

For IC1, the solution is mostly driven by conduction in the sense that more solid material is generated up to $\omega_{th} = 0.9$. Then, for $\omega_{th} = 0.99$, the optimiser generates a curved guidance for the fluid. At the end of this curved channel, a bit of material distribution takes place at the beginning of the outflow channel, which leaves a very tiny passage for the flow, and thus accelerates the latter, which increases the heat flux.

Regarding IC2, the narrow aspect is even more noted with increasing ω_{th} compared to the solutions of IC1. Also, some "roughness" is induced. For instance, the solution of IC2 with $\omega_{th} = 0.9 = 1 - \omega_{Pt}$ has a "wavy" surface. This irregular aspect of the surface is created in order to improve the heat transferred to the coolant fluid. For $\omega_{th} = 0.99$, the flow is blocked at the entrance of the outflow channel. After that, the flow still takes place as it can be seen in the velocity distribution. This has no physical sense since with a real solid wall positioned like this material distribution at the entrance of Ω_{out}, then no flow can take place in the outflow channel.

Finally, a very important remark that has to be done is the difference between the solutions of IC1 and IC2. The solutions obtained for IC1 are essentially driven by conduction while the topologies of IC2 get towards solutions that are controlled by convection through the generation of the narrow flow passages. For IC2, the solution consists in the fluid being closer
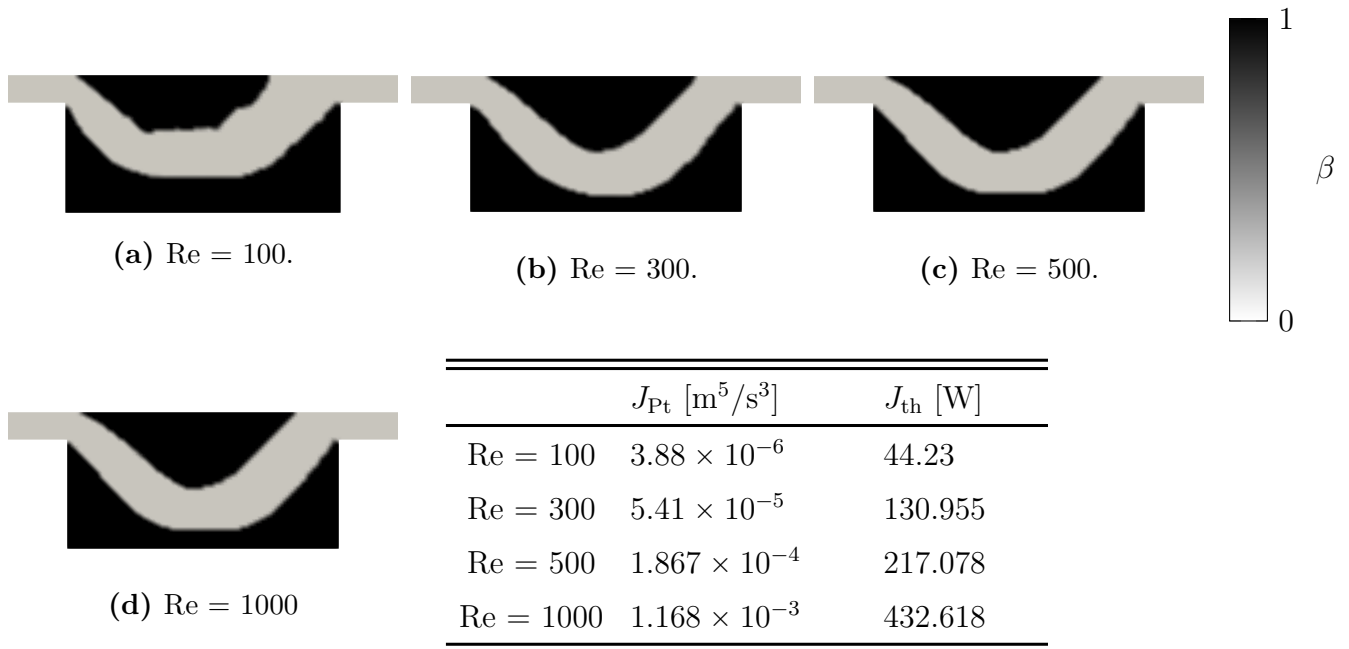
to the heated lower wall. This behaviour shows the presence of a multitude of (sub-)optimal solutions that can verify the constraints and attain the objectives settled in the problem. This aspect is due to the presence of a lot of design variables. It can be said that given an optimised solution that is generated by the optimiser, it is quasi impossible to predict if it is a global optimum. If the aim is to produce the best suited topology for the system, for now it is only possible if multiple initial conditions are tried and then compare their respective solutions between each other. This attitude of TO constitutes a major disadvantage. Future works can be devoted in order to cope with this allure of the methodology.

3.9 Influence of the Reynolds number

In this section, the effect of the Reynolds number on the obtained topologies will be studied. Then, the effect of the frozen turbulence assumption will be evaluated regarding the differences that it can generate in the optimised solutions.

In order to asses the effect of Re, the considered case will be the one of IC2 for $\omega_{\text{Pt}} = 0.4$ and $\omega_{\text{th}} = 0.6$. The topologies obtained for an increasing Reynolds number and the corresponding values of the objective functions are shown in Fig. 3.21. For increasing Re, the heat flux at the outlet is improved thanks to the higher values of the velocity. The increase in the velocities comes at the expense of an amplified pressure drop. It can be noted that even though the difference obtained in the objective functions is remarkable, the impact of the Reynolds number on the optimised topology has not so much effect in this range of Reynolds number except when Re goes from 100 to 300.

(a) Re = 100. (b) Re = 300. (c) Re = 500.

(d) Re = 1000

	J_{Pt} $[\text{m}^5/\text{s}^3]$	J_{th} $[\text{W}]$
Re = 100	3.88×10^{-6}	44.23
Re = 300	5.41×10^{-5}	130.955
Re = 500	1.867×10^{-4}	217.078
Re = 1000	1.168×10^{-3}	432.618

Figure 3.21: Solution of IC2 with $\omega_{\text{Pt}} = 0.4$ and $\omega_{\text{th}} = 0.6$ for different Reynolds number.

The optimisation has also been applied in a case for which the Reynolds number is equal to 2000. At this value of Re, the flow can be considered to become turbulent, and it can be said beforehand that due to the non-ordered aspect of the flow when it is turbulent, the resulting topology is expected to be also irregular. Three approaches are used in order to deal with the turbulence. The first trial (named APP1) consists in performing a fully laminar optimisation, i.e. the turbulence is not taken into account at all, which means that the spalart-Allmaras one equation turbulence equation is not solved. Then, the second test (noted APP2) will consists in what is called "frozen turbulence assumption". In the latter, the primal turbulence equation is solved, but the effect of the variation of the turbulence variable is not taken into consideration in the sensitivities. This means that the adjoint turbulence equation is not solved, leaving $\tilde{\nu}_a$ equal to zero. The last and third approach noted APP3 considers both primal and adjoint turbulnce. This means that the primal turbulence model equation is solved, and the adjoint turbulent equation is also solved. So the effect of the turbulence is taken into consideration in the sensitivities.

The results of the three approaches are given in Tab. 3.13 and Tab. 3.14. The effect of how the turbulence is treated is significant. Comparing the solution of APP1, for which the turbulence is not taken into consideration at all, to the solution of APP2, the great difference between them can be noted. The resolution of the primal turbulence equation gives a totally different optimised solution. The solution of APP3 is rather similar to APP2. For all cases, the topology is quite irregular as it was expected.
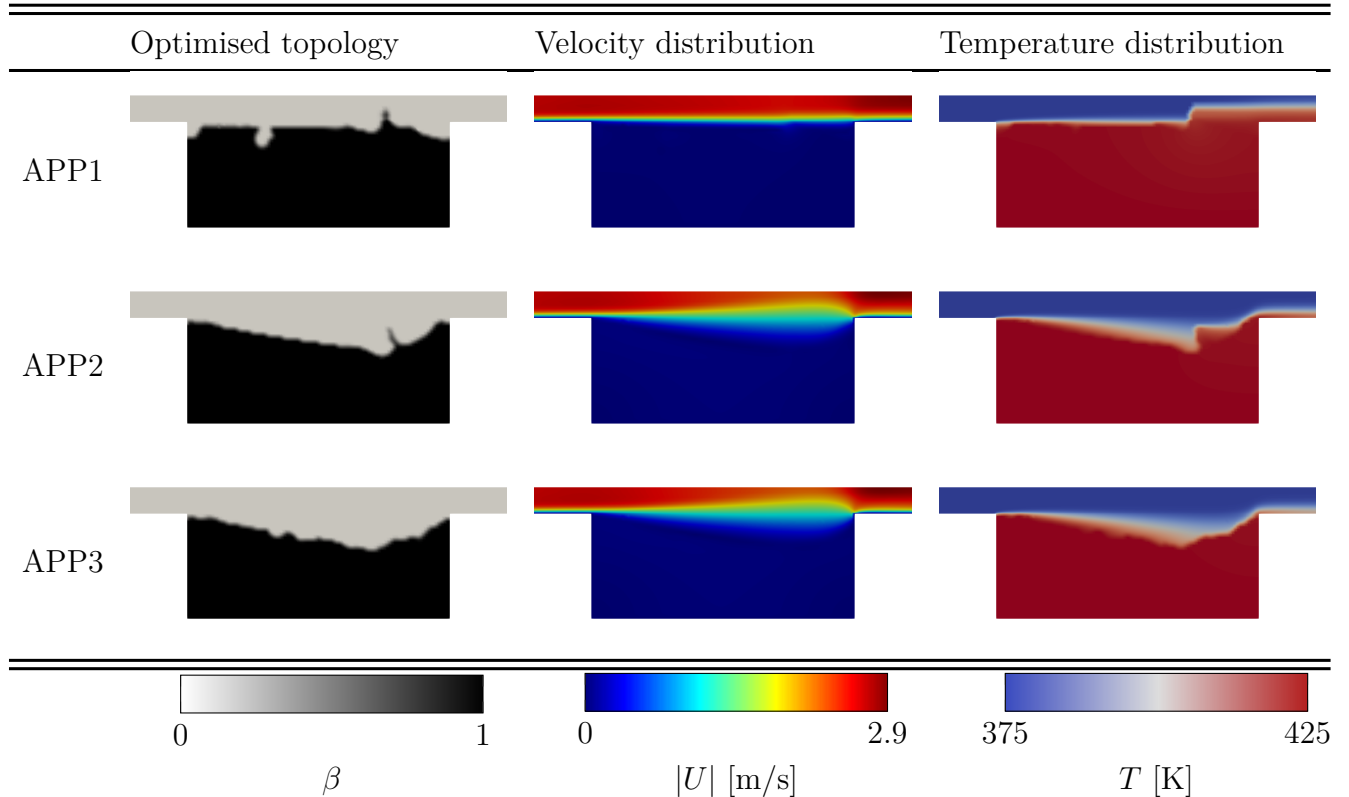
Table 3.13: Optimised topologies of APP1, APP2, and APP3.

	J_{Pt} [m⁵/s³]	J_{th} [W]
APP1	870.345	0.002
APP2	837.97	0.0047
APP3	832.006	0.0046

Table 3.14: Results of APP1, APP2, and APP3.

From all these observations, it can be concluded that in a moderate rage of Reynolds number, the solution for a fixed weighting parameter ω does not change a lot. But when approaching the turbulent regime, the optimised material distribution is driven towards a totally different topology with a significant effect of the treatment of turbulence. Omitting totally the turbulence (APP1) leads to a completely different solution compared to the cases of APP2 and APP3. Then, comparing APP2 and APP3 results, the effect of the turbulence sensitivity is noted. The solution including the turbulence sensitivities inside the analysis is in fact better in terms of the pressure drop. Therefore, it can be inferred that the exclusion of the turbulence variable differentiation can give very inaccurate sensitivities, and thus conduct the optimisation through a completely different path, resulting in unalike solutions.

3.10 Validation of the method with a body-fitted mesh

In order to validate the results given by topology optimisation, the solutions have to be verified in a domain with real solid walls. So the "porous" aspect of the material distribution must be replaced by real solid material. Then, the objective functions will be computed on this real solidified domain. To do so, a practical case that has been generated tanhks to topology optimisation in section 3.8 is used. This is the topology obtained for IC2 with ω_{Pt} = 0.4 and ω_{th} = 0.6 with Re = 100. In the following, the latter will be called "TOSol", and the solution provided by the body-fitted mesh will be called "BFSol". The topology of this case is shown in Fig. 3.22 where the black regions are real solid zones.

Figure 3.22: Topology of the domain in which the body-fitted validation will be done; solid material in black with real solid boundaries.

This structure is composed of three parts: two solid regions and one fluid region. In order to take into account the conduction in the solids, and the convection in the fluid flowing

between the two solid zones, a multi region CHT solver is needed. To come to that end, the *chtMultiRegionSimpleFoam* solver of OPENFOAM is used. This is a steady state solver for a buoyant turbulent fluid flowing inside a domain that undergoes conjugate heat transfer. This is an compressible solver. Therefore, the density variation is taken into account which was not the case in the approach used in topology optimisation where the density of the fluid was considered to be constant.

Concerning the boundary conditions, these are the same as the primal boundary conditions given in Tab. 3.2. In addition to these boundary conditions, the ones related to the new solid walls generated by the optimiser must be included. At these boundaries, the no slip boundary condition is imposed on the velocity, and a zero Neumann boundary condition is set for the pressure. Concerning the temperature at these new boundaries, there must be thermal equilibrium between the solid walls and the fluid by considering the heat transfer. This phenomenon is considered thanks to the *turbulentTemperatureCoupledBaffleMixed* of OPENFOAM.

In the upcoming sections, a mesh convergence study will be performed. This will be followed by the computation of the values of the objective functions that will be compared then to the ones of the "porous" result provided by the optimisation. This will permit to validate the consistency of the results given by topology optimisation and thus see if the density-based method is worth using in the scope of CHT problems.

3.10.1   Grid convergence study

In order to study the grid convergence, five mesh cases have been tried (Tab. 3.15). To choose the best suited one, the values of the thermal flux at the outlet and the pressure loss are compared to a very fine mesh noted Mesh0 which has 173504 cells that is considered to be valid. Considering these five cases, the evolution of the relative error with the different grids computed with the values of J_{th} and J_{Pt} with respect to the results of Mesh0 is displayed in Fig. 3.23.

	Mesh1	Mesh2	Mesh3	Mesh4	Mesh5
N_{cells} [-]	8723	12 400	21 882	33 075	58 477

Table 3.15: Test cases for the spatial discretisation of the body-fitted case.

(a) Relative error on J_{Pt}.

(b) Relative error on the heat flux J_{th}.
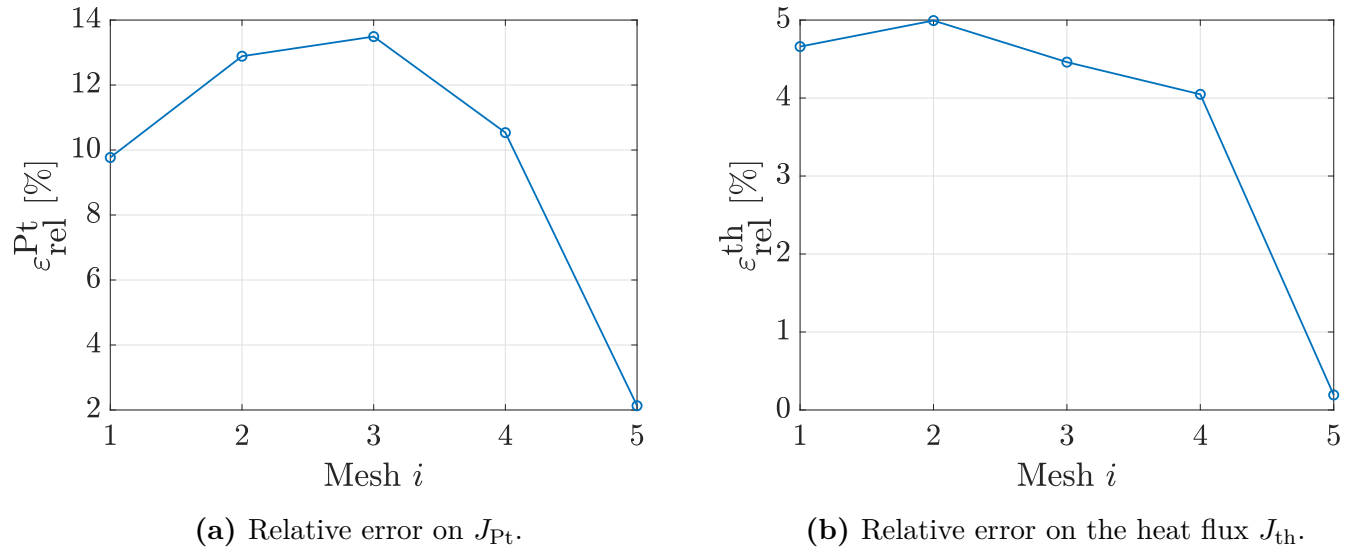
Figure 3.23: Relative error on J_{Pt} and J_{th} with the different body fitted meshes.

The lowest relative errors for both objective functions takes place for the fifth test case. That is why Mesh5 will be used in the following analysis. This grid is shown in Fig. 3.24. A refinement is done at the boundaries between the fluid and the solid.
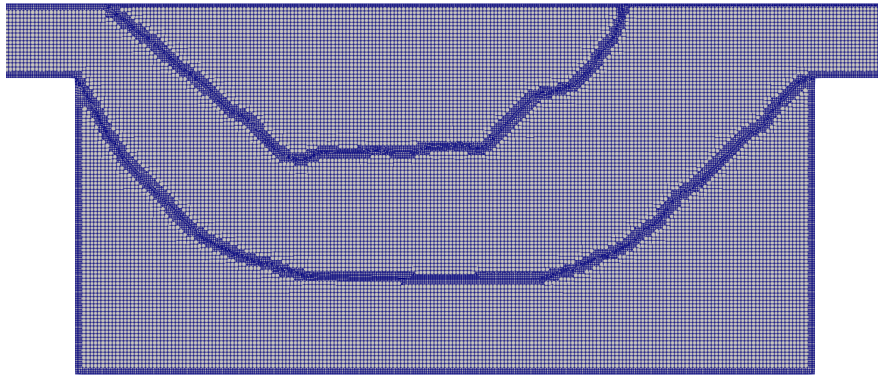
Figure 3.24: Body fitted grid (Mesh5).

3.10.2 Validation of the results

The results of the corresponding topology given by the optimisation must now be compared to the results of the body fitted mesh. The simulation of the body fitted mesh run enough time to achieve the permanent regime and thus have a consistent result to compare with TOSol. The proof of achievement of this permanent regime is illustrated in Fig. 3.25 showing the evolution of the average outlet temperature with the iterations.
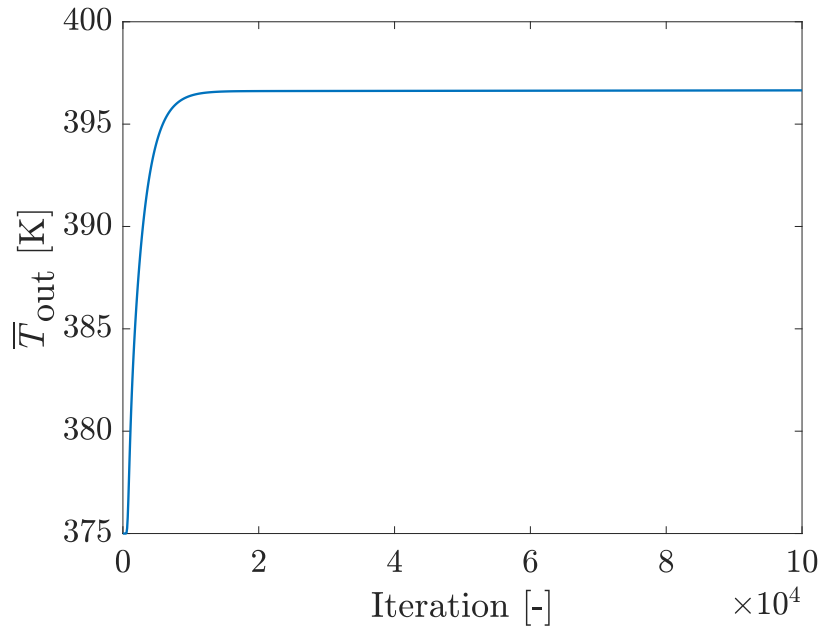
Figure 3.25: Evolution of the average outlet temperature with the iterations for BFSol.

The velocity and temperature profiles of TOSol and BFSol are provided in Fig. 3.26 and Fig. 3.27. The values of J_{Pt}, J_{th} and T_{out} of TOSol and BFSol are given in Tab. 3.16. Regarding the velocity and temperature distributions, a very close similarity for the results provided by TOSol and BFSol can be noted.

(a) TOSol.

(b) BFSol.

$|U|$ [m/s]
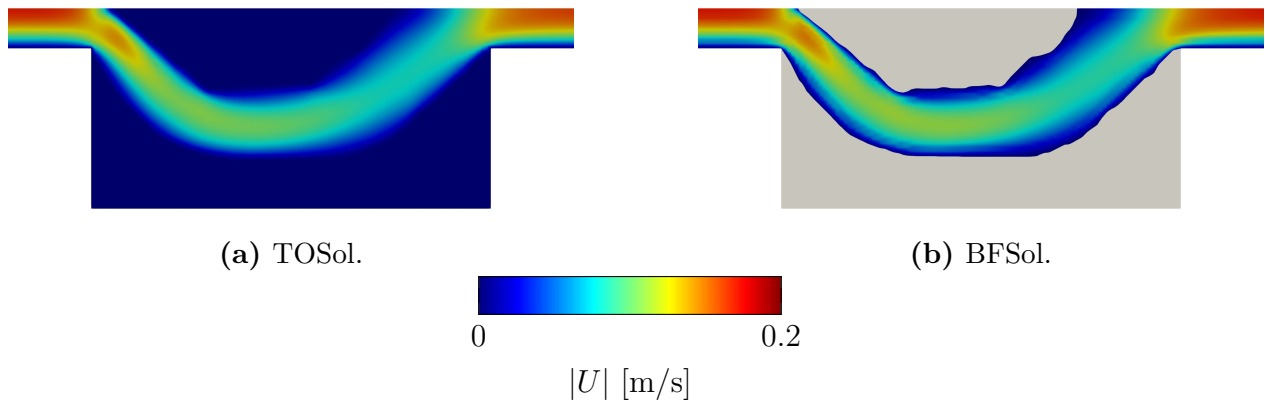
Figure 3.26: Velocity distribution of TOSol and BFSol.

(a) TOSol.

(b) BFSol.

$$375 \qquad\qquad 425$$

$$T \; [\mathrm{K}]$$
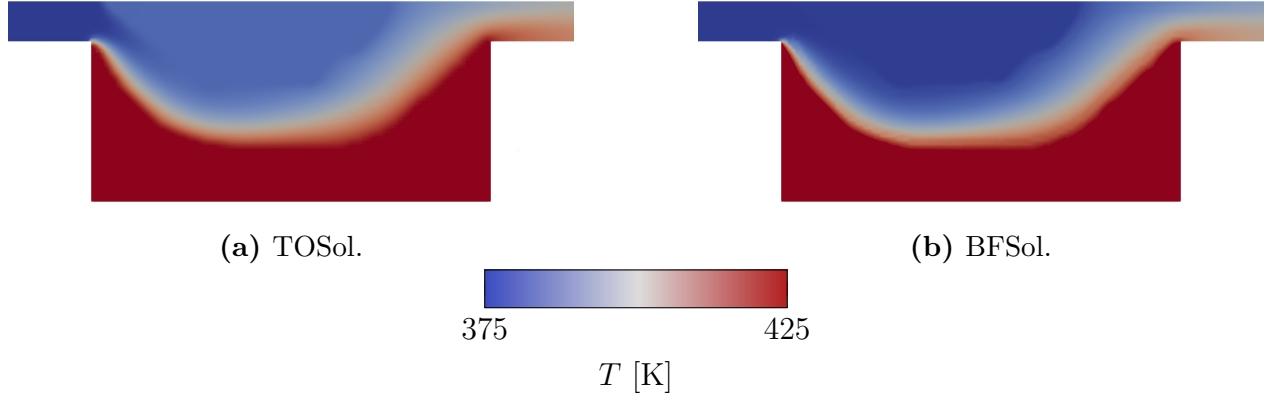
Figure 3.27: Temperature distribution of TOSol and BFSol.

	$J_{\mathrm{Pt}} \; [\mathrm{m^5/s^3}]$	$J_{\mathrm{th}} \; [\mathrm{W}]$	$\overline{T}_{\mathrm{out}} \; [\mathrm{K}]$
TOSol	3.88×10^{-6}	44.23	404.311
BFSol	4.9437×10^{-6}	42.9183	395.6654

Table 3.16: Values of the objective functions of TOSol and BFSol.

As it can be observed in Tab. 3.16, there is some difference in the pressure losses and the heat flux at the outlet provided by the two approaches. These differences are very small. A more objective assessment is achieved by comparing the difference brought by the optimisation (noted Δ^{opt}) in the objective functions, and the difference in the computed values between BFSol and TOSol (noted Δ^{Sol}). This is done in Tab. 3.17.

	$J_{\mathrm{Pt}} \; [\mathrm{m^5/s^3}]$	$J_{\mathrm{th}} \; [\mathrm{W}]$
Δ^{opt}	-1.383×10^{-4}	28.8136
Δ^{Sol}	-1.064×10^{-6}	1.3117

Table 3.17: Comparison of the difference in the objective functions brought by the optimisation with the difference between the values provided by TOSol and BFSol.

The absolute value of Δ^{opt} for each of the objective functions being way bigger than the correspondent difference Δ^{Sol} in absolute value, it can be noted that the result given by the "porous" approach used in topology optimisation was consistent.

An additional remark that can be done regarding the differences between TOSol and BFSol is that the pressure losses are higher for the BFSol since real solid wall leads to a more important obstacle for the fluid compared to a porous medium. Moreover, the fact that the buoyant solver used for BFSol takes into account the density variation impacts the computations. This may explain why the heat flux is lower since the density of the fluid flowing

69

inside the domain decreases with increasing temperature of the fluid.

In conclusion, it can be said that the density-based approach used in topology optimisation is well consistent concerning the results it provides.

Chapter 4

3D CHT Topology Optimisation

In this chapter, a more interesting structure will be optimised topologically. The domain being this time in three dimensions, this will increase the complexity of the optimisation process.

First of all, the spatial discretisation will be presented. Then, TO will be applied on this complex case. The conducted analysis will show how difficult it is to optimise a 3D CHT problem subjected to turbulent flows.

4.1   Problem definition

The problem consists of a 3D heat exchanger. The heat exchanger has two fluid phases: the air and the oil. The oil having a good conductance, there is no need of optimising the flow path of the oil. Therefore, a Dirichlet boundary condition is imposed on the oil side.

The domain in which the optimisation takes place is illustrated in Fig. 4.1 where the presence of the oil is taken as a boundary condition applied for the temperature at the lower red surface called "oil side". The green surfaces are adiabatic walls, and the blue surface are the inlet and the outlet. The domain is symmetric from either side of the grey surfaces whose normal are parallel to the vector $\vec{Z}$. The flow takes place in the $\vec{X}$ direction entering into the domain from the inlet face (blue front surface).

The flow enters into the domain with a velocity equal to 17 m/s at a temperature of 375K. The temperature of the oil is equal to 425 K. The solid material that will constitute the topology of the domain is Aluminium. The properties of air and Aluminium at their respective temperatures are given in Tab. 3.1. Based on the length of the domain along $\vec{X}$, the Reynolds number is approximately equal to 165 084. As the latter is very big, the flow is turbulent. The boundary conditions applied on each surface of the domain are summarised in Tab. 4.1.
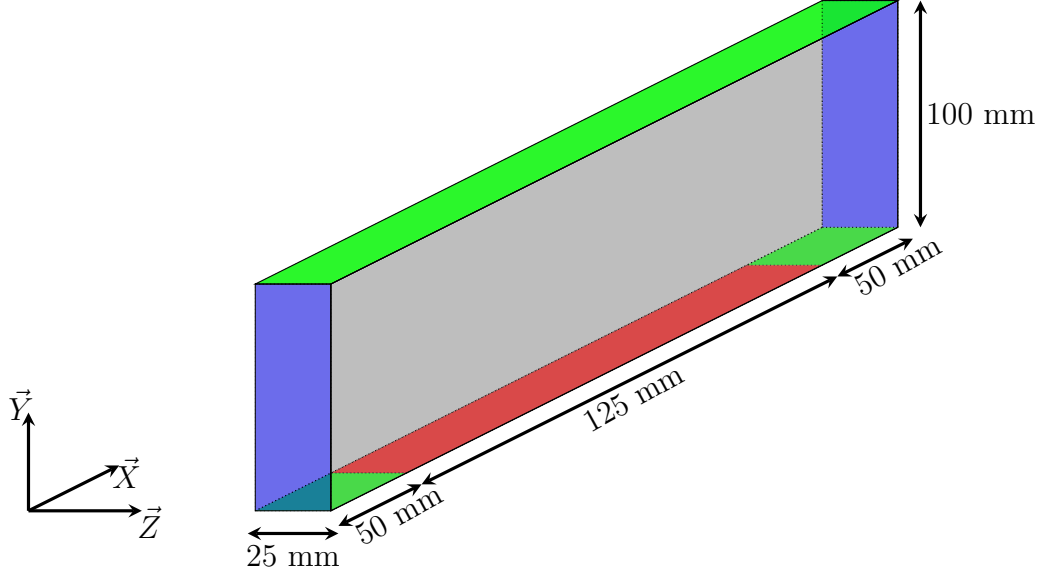
Figure 4.1: 3D heat exchanger geometry.

	Inlet	Outlet	Adiabatic walls	Oil Side	Symmetric walls
U	Dirichlet	Zero Neumann	Zero Dirichlet	Zero Dirichlet	Symmetric
p	Zero Neumann	Zero Dirichlet	Zero Neumann	Zero Neumann	Symmetric
T	Dirichlet	Zero Neumann	Zero Neumann	Dirichlet	Symmetric
ν_t	Calculated	Calculated	Wall function	Wall function	Symmetric
$\tilde{\nu}$	Calculated	Zero Neumann	Zero Dirichlet	Zero Dirichlet	Symmetric

Table 4.1: Boundary conditions of 3D heat exchanger.

The eddy viscosity ν_t is computed as follows

$$\nu_t = \sqrt{\frac{3}{2}} U_{\text{in}} I_t l_{\text{T}} \tag{4.1}$$

where U_{in} in the inlet velocity, I_t is the turbulence intensity set to 0.01, and l_{T} is the turbulent length scale equal to $0.07 \times h_{\text{max}}$, with h_{max} equal to 100 mm in this case. The wall function used at the walls is the one provided in OPENFOAM which models the inner sub-layer and the logarithmic region of the boundary layer using a single formula. More details about this wall function are given in [44].

The effective viscosity $\tilde{\nu}$ is computed based on the fluid viscosity as it is suggested by [59] with the following formula

$$\tilde{\nu} = 5\nu. \tag{4.2}$$

The boundary conditions being specified, the next step is to introduce the spatial discretisation.

4.2 Spatial discretisation

As the domain is simple, the grid is made of square cells of 1×10^{-3} mm^2 in the $\vec{X} - \vec{Y}$ plane. In the $\vec{Z}$ direction, the size of the cells has been divide in three. As a matter of fact, when conducting an optimisation of a heat exchanger, the first idea is to put fins that are aligned in the direction of the flow. This will be done as a first inital guess for the optimisation in the following section. If the width of each fin is considered to be equal to 1 mm and if three cells are desired along the width of the fins, the size of the cells must be divided by three. That is why grids of 0.33×10^{-3} mm of length are putted along the $\vec{Z}$ direction. This is illustrated in Fig. 4.2 obtained by making a zoom on the geometry in the $\vec{Y} - \vec{Z}$ plane. The yellow zones show the distribution of the cells in the fins.
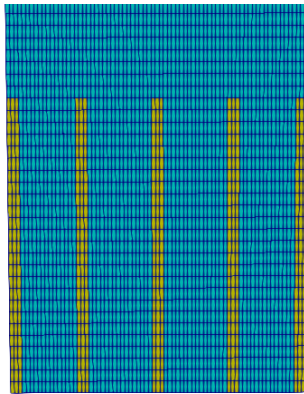

Figure 4.2: 3D heat exchanger grid in the $\vec{Y} - \vec{Z}$ plane.

4.3 Optimisation of the heat exchanger

The flow taking place inside the domain has a great Reynolds number, leading to a highly turbulent flow. On top of that, the geometry is in 3D. Handling such a problem is very difficult. The initial condition consists in a domain filled with fluid except the presence of solid fins in contact from their bottom with the oil side. The fins are distributed symmetrically and their temperature is initially equal to 425 K. The positioning of the fins is shown in Fig. 4.3 with a perspective view.

The goal is to see if starting from these fins, the optimiser can generate a better topology enhancing greatly the thermal flux while limiting the pressure drops. The normalisation factors $J_{\text{Pt, norm}}$ and $J_{\text{th, norm}}$ are respectively equal to 15 m^5/s^3 and 15422.8 W. The normalisation factor of J_{th} is calculated by the optimiser as always, so $J_{\text{th, norm}}$ is equal to $J_{\text{th, init}}$. But the one of the pressure drop is set manually in order to prevent the great importance of the pressure losses in the weighted and normalised objective function $\hat{J}$. If $J_{\text{Pt, norm}}$ is set by the optimiser, then the contribution of J_{Pt} in $\hat{J}$ is important, and the optimiser tends to remove the fins in order to decrease the pressure losses rather than improving the topologies of the fins. The weighting factors are equal to $\omega_{\text{Pt}} = 0.01$ and $\omega_{\text{th}} = 0.99$, the Darcy number is

set 10^{-6}, and the regularisation radius based on the average cell volume is equal to 7×10^{-4} m.
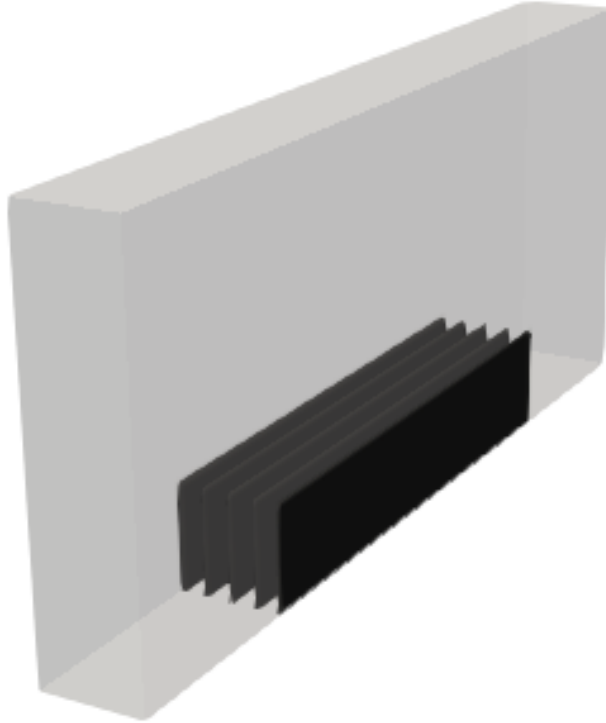

Figure 4.3: Distributions of the fins in the initial setting.

The primal turbulence equation is solved, but the adjoint turbulence is not taken into consideration, i.e. the equation for $\tilde{\nu}_a$ is not solved. So the variation of ν_t is not taken into account in the sensitivities but ν_t manifests its effects through the primal state of equations by being included in the primal momentum equations and in the primal energy equation. The optimisation gave consistent results up to the 22-th optimisation cycle for which the optimised topology looks like in Fig. 4.4. The latter looks better. For this distribution of material, the heat flux at the outlet is equal to 15545.5 W and the pressure losses are equal to 23.355 m^5/s^3. The velocity streamlines and the temperature distributions are given in Fig. 4.5. Concerning the permeability of the domain where there is material, it can be noted that there is a small leakage of flow because of the velocity being larger than zero there. This means that the value of λ_{max} is not high enough. λ_{max} must be increased but at the expense of having a risk of unstable optimisation. In order to have a clearer view of the velocity and the temperature inside the domain, a slice in the middle of the domain of normal $\vec{Z}$ is displayed in Fig. A.4. For the next optimisation cycle, the iterated solution diverges and leads to the topology given in Fig. 4.6 which is not symmetrical at all. Although the optimised solution for the 22-th cycle seems to be a relatively good design, the solution diverges at the next cycle and the convergence does not take place in this case.

From this example, the complexity of optimising a 3D domain with a highly turbulent flow inside it has been experienced. Although the convergence to an optimal design is not achieved,

the method of topology optimisation has proven its ability to generate optimised designs in the first cycles. The part of the optimisation process that causes a great difficulty is the resolution of the adjoint equations for which the convergence is very complicated. The resolution of these equations must be stabilised in possible future works. Also, the adjoint turbulence equation has not been solved. In possible future works, the resolution of this equation must be tried to see if there is a great effect of the adjoint turbulence in the allure of the optimised topology for this cumbersome case.
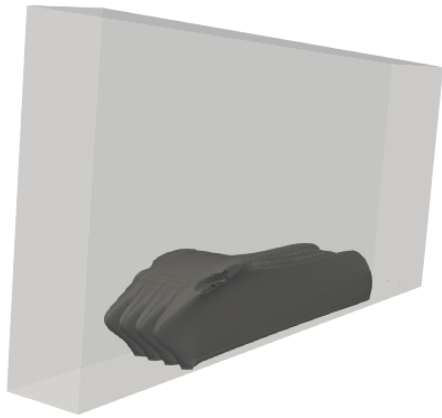
(a) View in perspective.

(b) View in the $\vec{X} - \vec{Y}$ plane.

(c) Solid material viewed from the inlet.

(d) Solid material viewed from the outlet.

(e) Solid material viewed from the top on the $\vec{X} - \vec{Z}$ plane (inlet on the left side, outlet on the right side).

Figure 4.4: Topology of the 3D heat exchanger at the 22-th optimisation cycle with the primal turbulence solved and adjoint turbulence not taken into account; overall domain in clear grey, and solid material in dark grey.

(a) Streamlines of the velocity.

(b) Temperature distribution.
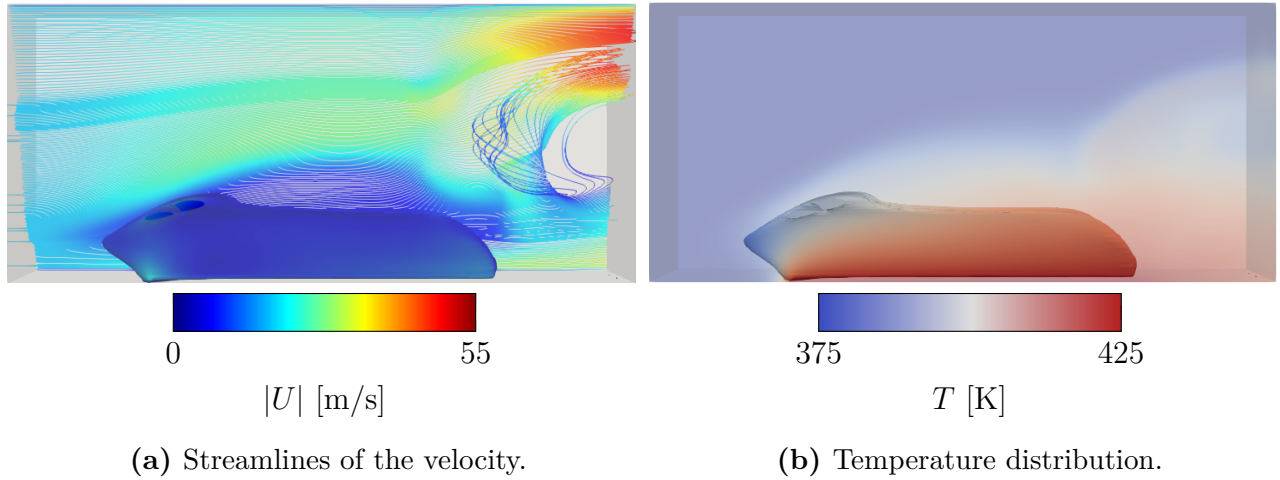
Figure 4.5: Streamlines of the velocity, and temperature distribution of the 3D heat exchanger at the 22-th optimisation cycle with the primal turbulence solved and adjoint turbulence not taken into account.
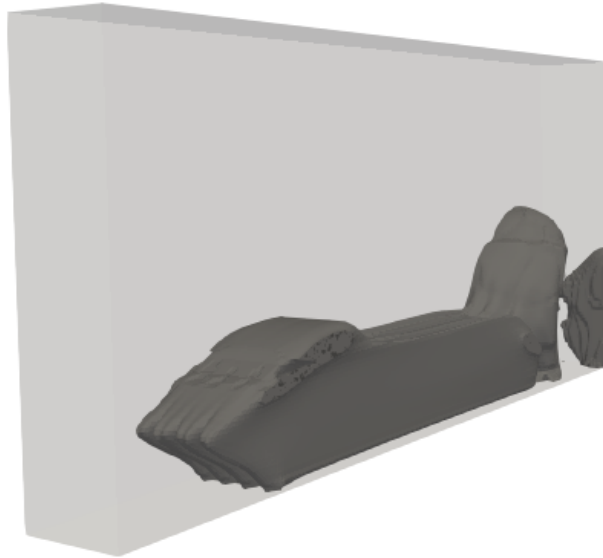
Figure 4.6: Topology of the 3D heat exchanger at the 23-th cycle with the primal turbulence solved and adjoint turbulence not taken into account; overall domain in clear grey, and solid material in dark grey.

Chapter 5

Conclusion and perspectives

5.1 Conclusion

In this thesis, the main goal was to first understand the general approach of topology optimisation and then appropriate the technique to a fluid problem, and especially to a conjugate heat transfer (CHT) problem. After a detailed exposition of the gradient based methods used in the scope of existing structural problems, a review of the application of topology optimisation for fluid flows has been done. The density (or porosity) based topology optimisation has then been specified for a CHT problem. Along with the different equations intervening in the latter, new development related to the regularisation and the projection of the design field have been explained. Following this, the continuous adjoint formulation has been clarified. Then, the global layout of a topology optimisation process for a CHT problem has been summarised.

In order to assess the effect of the numerous parameters intervening in the optimisation procedure, a parameter study has been conducted on a practical two dimensional CHT system. First of all, the influence of the spatial discretisation has been analysed. This has figured out the dependency of the optimised solution on the grid when omitting the regularisation. This dependency was not so marked in the simple case that was considered but in much complicated systems, this could be much more noted. The study of the spatial discretisation gave a first insight in the understanding of the regularisation, showing that the regularisation gives mesh-independent solutions. Successively, the effect of the regularisation has been evaluated along with the projection. As the density based approach uses intermediate values of the design variable allowing thus for grey transitions from fluid to solid regions, a projection of the design field was thus needed in order to have a binary material distribution. Following this, the porosity source term included in the flow equations has been studied. There is in fact different types of functions of interpolation that give this term which is scaled with the inverse permeability depending on the design field. The analysis showed a great sensitivity of the optimisation to these interpolation functions, and it was concluded that a Borrvall-Petersson type interpolation function was best suited for the current type of problem. Successively, the way the thermo-physical properties are treated with the distribution of material has also

been treated by considering the various types of interpolation of these properties between the fluid and the solid. This showed that the SIMP interpolation, as it was commonly used in structural mechanics problem, was also preferable for fluid based problems. Then, the effect of the Darcy number on the porosity of the solidified zones has been assessed. As it was expected, with the decrease of this number, the obtained material distribution got towards a real solid with almost no flow leakage inside it. Subsequently, the influence of the initial conditions has shown an important sensitivity of the method to the initial settings of the design field. For a different initial material distribution, the optimiser gave distinguished results. This phenomenon manifested the presence of many optimal solutions, and when a solution is achieved, it cannot be ensured that the latter is a global one. Then, the effect of the Reynolds number has been evaluated. The important remark is the influence of how turbulence is treated. Omitting turbulence in the sensitivity has led to completely dissimilar results. This aspect seems to confirm the inaccuracy of the computed sensitivities when neglecting turbulence for a high Reynolds number. All of these parametric analysis showed a high dependence of the optimisation on these input data. This makes the difficulty of the usage of the method. Finally, the results of one of the optimised solutions has been validated using a body fitted mesh. This was done in order to ensure that the solutions given by the optimisation concerning the different quantities of interest were close to the ones provided with real solid walls. This comparison showed a close proximity between the results of the "porous" approach used in topology optimisation and the ones of the body fitted case. It can be said that this was due to a good tuning of the projection parameter that gave a neat transition from solidified regions to the fluid zones, and the Darcy number that was low enough.

Finally, the method of topology optimisation has been tried on a 3D heat exchanger subjected to a highly turbulent flow. The convergence to an optimal solution was not achieved but the optimisation could generate interesting designs for the first optimisation cycles.

5.2   Further works

There are many things to do in the future in order to improve the method of topology optimisation.

First of all, the fact that there are lots of (sub-)optimal solutions due to the high number of design variables is a major issue. It is already very complicated to tune the different parameters in order to end with a solution that is physically meaningful. On top of that, achieving a global optimum and then being aware that this optimum is a global one seem for now impossible facts. Future studies can be devoted in order to cope with this allure of topology optimisation.

In the scope of this thesis, topology optimisation has been applied to a problem with only one fluid. But it is possible to use the same approach for problems including multiple fluids. This could be for instance the case of heat exchangers with two fluids where the objectives are to increase the heat transferred from one fluid to the other and limiting the pressure drops

in each fluid. In this work, the pressure losses were comprised inside the objective function, but it could be interesting to test cases where the pressure drop is constrained instead of a function to minimise.

In this study, the optimisation was done on a problem with a well defined regime, i.e. for a unique Reynolds (except when the effect of the Reynolds number was studied) with a unique value of the different temperatures that were imposed at the entrance and at the heated wall of the CHT system. In possible further works, it may be attractive to consider different cases to which corresponds different Reynolds numbers and temperatures. Then, considering these different cases, topology optimisation can be used to generate a unique optimised solution that could meet the objectives of these distinguished cases. This approach can be for instance useful when designing the heat exchanger of an airplane. As the airplane undergoes different flight regimes, it could be motivating to generate an optimised heat exchanger that is well suited for these different regimes. The author of this thesis has tried to optimise a 3D heat exchanger but for one regime, i.e. with a fixed Reynolds number and fixed temperatures. The case being in three dimensions, the optimisation was way more complicated and very difficult to stabilise, and especially because of the very high Reynolds number. Eventual subsequent works could be devoted to optimise such a cumbersome application.

Considering the turbulent cases, the body-fitted mesh has not been applied to the latter. In order to be sure that the results of topology optimisation given for problems including turbulent flows are consistent, a body-fitted validation must be done. One more analysis that can be done is to consider different types of turbulent models used in the scope of topology optimisation. In this thesis, the Spalart-Allmaras one equation model was used.
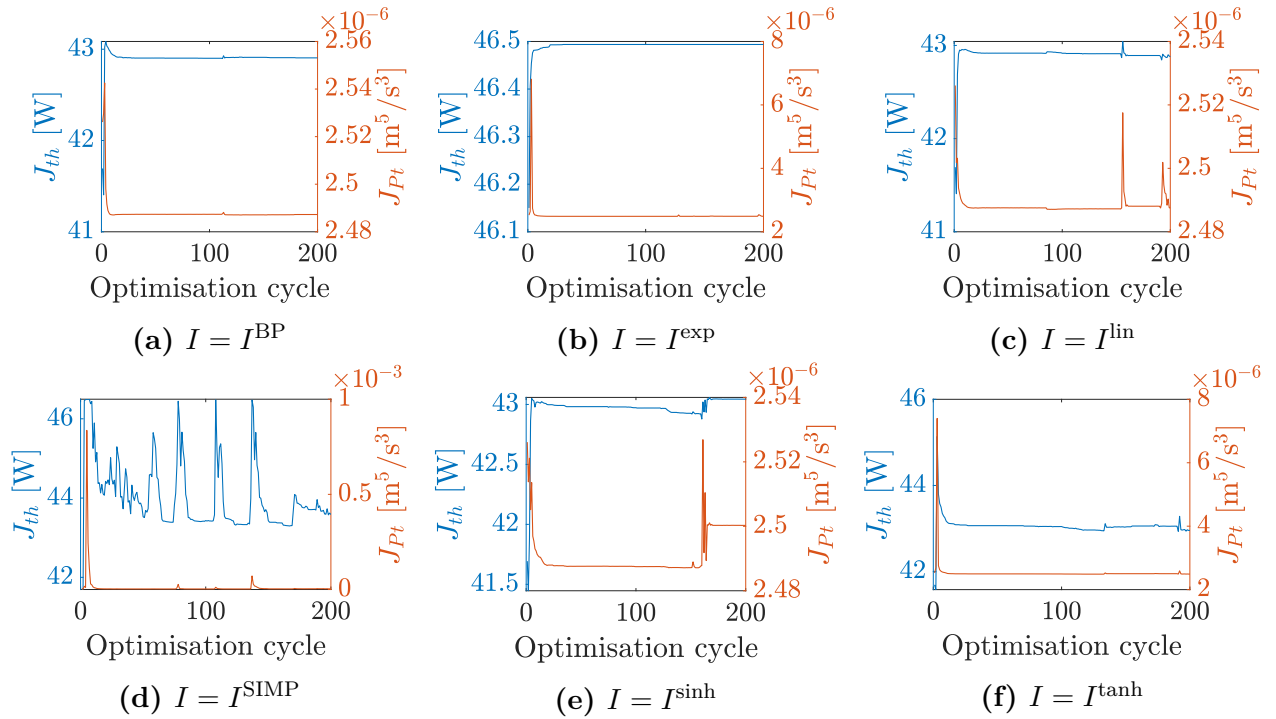
Within the current thesis, the flow was considered to be incompressible. Further works can cope with fluid-based problems subjected to compressible flows. This could be for instance useful for turbomachinery, and other aerospace or aeronautical applications.
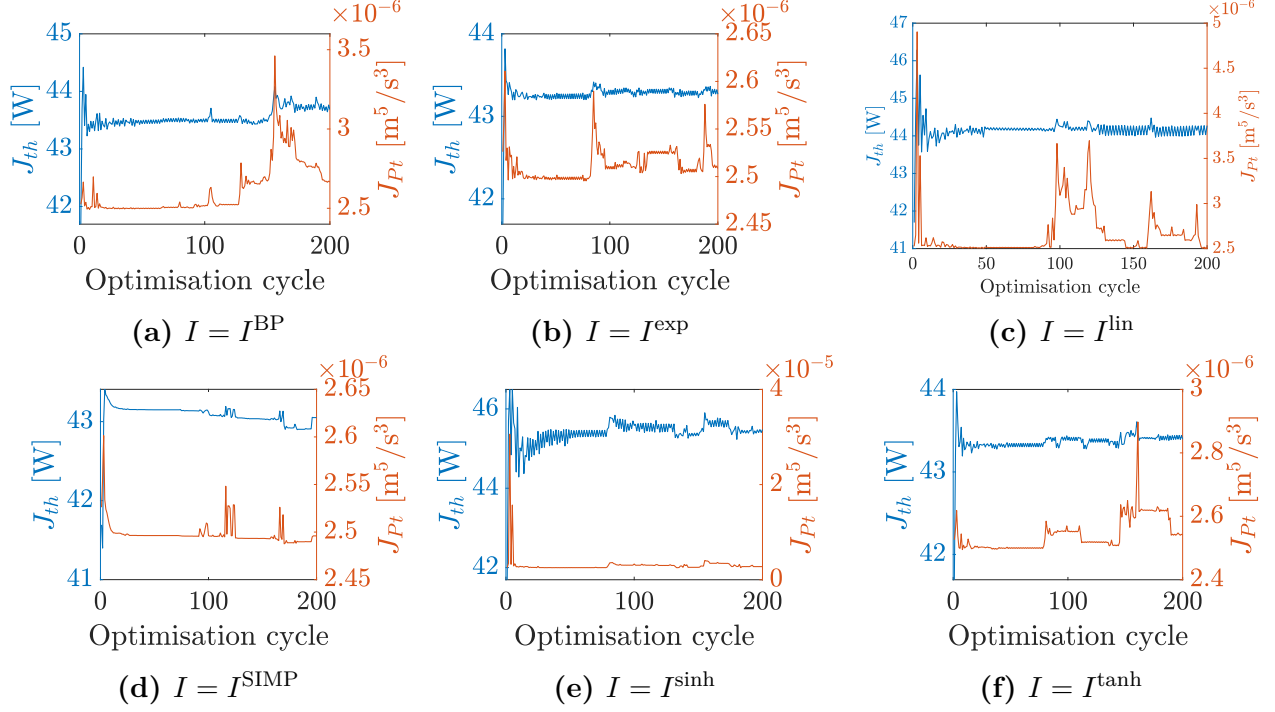
Appendices

Appendix A

Additional figures

Figure A.1: Convergence history for the different interpolation functions for the porosity dependent source terms with $q = 10$; $R = 1$ mm; $\omega_{Pt} = 1$, $\omega_{th} = 0$.

Figure A.2: Convergence history for the different interpolation functions of the thermophysical properties with $q^{th} = 5$; $R = 1$ mm; $\omega_{Pt} = \omega_{th} = 0.5$.
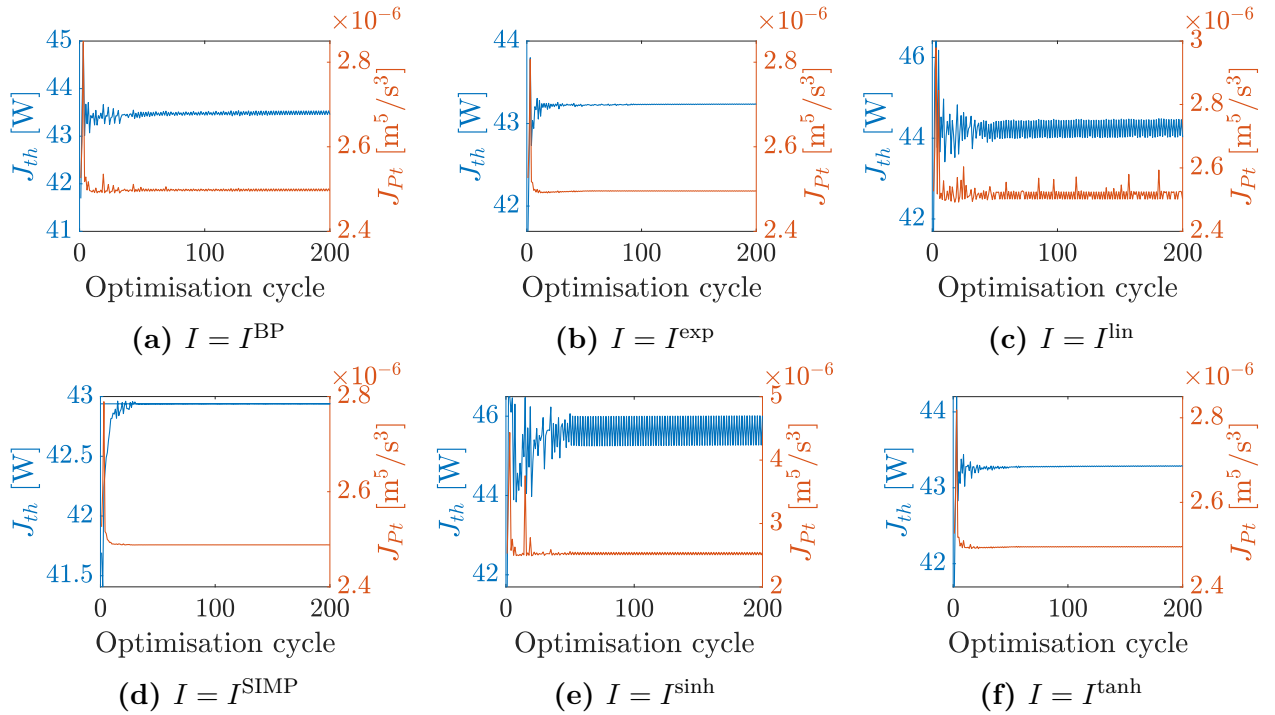
Figure A.3: Convergence history for the different interpolation functions of the thermophysical properties with $q^{th} = 5$; $R = 10$ mm; $\omega_{Pt} = \omega_{th} = 0.5$.

(a) Velocity distribution.

(b) Temperature distribution.
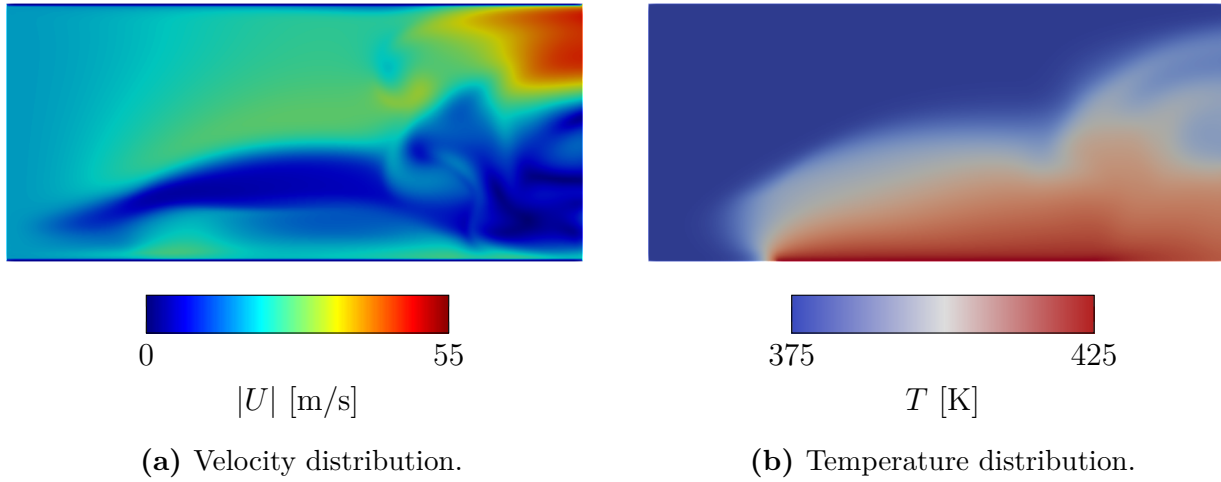
Figure A.4: Velocity and temperature distributions in the $\vec{X} - \vec{Y}$ plane of the 3D heat exchanger at the 22-th optimisation cycle with the primal turbulence solved and adjoint turbulence not taken into account.

Bibliography

[1] A. Gebisa and H. Lemu. A case study on topology optimized design for additive manufacturing. *IOP Conference Series: Materials Science and Engineering*, 276:012026, 12 2017.

[2] M. Bruyneel. *Schémas d'approximation pour la conception optimale de structures en matériaux composites.* PhD thesis, Université de Liège, Belgique, 2002.

[3] A.G.M. Michell M.C.E. Lviii. the limits of economy of material in frame-structures. *The London, Edinburgh, and Dublin Philosophical Magazine and Journal of Science*, 8(47):589–597, 1904.

[4] M. P. Bendsøe and N. Kikuchi. Generating optimal topologies in structural design using a homogenization method. *Computer Methods in Applied Mechanics and Engineering*, 71(2):197–224, 1988.

[5] M. P. Bendsøe. Optimal shape design as a material distribution problem. *Structural Optimization*, 1:193–202, 01 1989.

[6] G. I. N. Rozvany, M. Zhou, and T. Birker. Generalized shape optimization without homogenization. *Structural optimization*, 4:250–252, 1992.

[7] Y. Mei and X. Wang. A level set method for structural topology optimization and its applications. *Adv. Eng. Softw.*, 35(7):415–441, jul 2004.

[8] G. Allaire, F. Jouve, and A. M. Toader. Structural optimization using sensitivity analysis and a level-set method. *Journal of Computational Physics*, 194(1):363–393, 2004.

[9] J. D. Deaton and R. V. Grandhi. A survey of structural and multidisciplinary continuum topology optimization: Post 2000. *Struct. Multidiscip. Optim.*, 49(1):1–38, jan 2014.

[10] K.C. Giannakoglou, E.M. Papoutsis-Kiachagias, and K.T Gkaragkounis. *adjointOptimisationFoam, an OpenFOAM-based optimisation tool.* Parallel CFD & Optimization Unit, School of Mechanical Engineering, National Technical University of Athens.

[11] Y. M. Xie and G. P. Steven. *Evolutionary Structural Optimization.* Springer London, 1997.

[12] X. Huang and Y. Xie. *Evolutionary Topology Optimization of Continuum Structures: Methods and Applications.* John Wiley & Sons, 04 2010.

[13] N. P. Dijk, K. Maute, M. Langelaar, and F. Keulen. Level-set methods for structural topology optimization: A review. *Struct. Multidiscip. Optim.*, 48(3):437–472, sep 2013.

[14] S. Osher and J. A. Sethian. Fronts propagating with curvature-dependent speed: Algorithms based on hamilton-jacobi formulations. *Journal of Computational Physics*, 79(1):12–49, 1988.

[15] V. Daru. Level set methods and fast marching methods – evolving interfaces in computational geometry, fluid mechanics, computer vision, and materials science. *European Journal of Mechanics - B/Fluids*, 19:531–532, 07 2000.

[16] S. Osher and R. Fedkiw. *Level Set Methods and Dynamic Implicit Surfaces.* Applied Mathematical Sciences. Springer New York, 2002.

[17] J.A. Sethian and Andreas Wiegmann. Structural boundary design via level set and immersed interface methods. *Journal of Computational Physics*, 163(2):489–528, 2000.

[18] A. M. Bradley. Pde-constrained optimization and the adjoint method. `https://cs.stanford.edu/~ambrad/adjoint_tutorial.pdf`, November 2010.

[19] K. Svanberg. The method of moving asymptotes - modelling aspects and solution schemes (lecture notes for the dcam 1 course advaneecl topies in structural optimization), July 1998.

[20] T. Borrvall and J. Petersson. Topology optimization of fluid in stokes flow. *International Journal for Numerical Methods in Fluids*, 41:77 – 107, 01 2003.

[21] J. Cahouet and J.-P. Chabard. Some fast 3d finite element solvers for the generalized stokes problem. *International Journal for Numerical Methods in Fluids*, 8(8):869–895, 1988.

[22] A. Evgrafov. The limits of porous materials in the topology optimization of stokes flows. *Applied Mathematics and Optimization*, 52:263–277, 2005.

[23] A. Gersborg-Hansen, O. Sigmund, and R.B. Haber. Topology optimization of channel flow problems. *Structural and Multidisciplinary Optimization*, 30:181–192, 2005.

[24] L. Olesen, F. Okkels, and H. Bruus. A high-level programming-language implementation of topology optimization applied to steady-state navier–stokes flow. *International Journal for Numerical Methods in Engineering*, 65:975 – 1001, 02 2006.

[25] J. Guest and J. Prevost. Topology optimization of creeping fluid flows using a darcy–stokes finite element. *International Journal for Numerical Methods in Engineering*, 66:461 – 484, 04 2006.

[26] C. Othmer. A continuous adjoint formulation for the computation of topological and surface sensitivities of ducted flows. *International Journal for Numerical Methods in Fluids*, 58(8):861–877, 2008.

[27] S. Kreissl, G. Pingen, and K. Maute. Topology optimization for unsteady flow. *International Journal for Numerical Methods in Engineering*, 87:1229 – 1253, 09 2011.

[28] Y. Deng, Z. Liu, P. Zhang, Y. Liu, and Y. Wu. Topology optimization of unsteady incompressible navier–stokes flows. *Journal of Computational Physics*, 230(17):6688–6708, 2011.

[29] E. A. Kontoleontos, E. M. Papoutsis-Kiachagias, A. S. Zymaris, D. I. Papadimitriou, and K. C. Giannakoglou. Adjoint-based constrained topology optimization for viscous flows, including heat transfer. *Engineering Optimization*, 45(8):941–961, 2013.

[30] G. H. Yoon. Topology optimization for turbulent flow with spalart–allmaras model. *Computer Methods in Applied Mechanics and Engineering*, 303:288–311, 2016.

[31] S. B. Dilgen, C. B. Dilgen, D. R. Fuhrman, O. Sigmund, and B. S. Lazarov. Density based topology optimization of turbulent flow heat transfer systems. *Structural and Multidisciplinary Optimization*, 57:1905–1918, 2018.

[32] G. H. Yoon. Topology optimization method with finite elements based on the k-ϵ turbulence model. *Computer Methods in Applied Mechanics and Engineering*, 361:112784, 2020.

[33] E. M. Dede. Multiphysics topology optimization of heat transfer and fluid flow systems. 2009.

[34] E. M. Dede. Optimization and Design of a Multipass Branching Microchannel Heat Sink for Electronics Cooling. *Journal of Electronic Packaging*, 134(4), 08 2012. 041001.

[35] G. H. Yoon. Topological design of heat dissipating structure with forced convective heat transfer. *Journal of Mechanical Science and Technology*, 24:1225–1233, 2010.

[36] T. Matsumori, T. Kondoh, A. Kawamoto, and T. Nomura. Topology optimization for fluid–thermal interaction problems under constant input power. *Structural and Multidisciplinary Optimization*, 47:571–581, 2013.

[37] G. Marck, M. Nemer, and J. L. Harion. Topology optimization of heat and mass transfer problems: Laminar flow. *Numerical Heat Transfer, Part B: Fundamentals*, 63:508–539, 06 2013.

[38] B. Zhang and L. Gao. Topology optimization of convective heat transfer problems for non-newtonian fluids. *Structural and Multidisciplinary Optimization*, 60:1821–1840, 11 2019.

[39] R. Tawk, B. Ghannam, and M. Nemer. Topology optimization of heat and mass transfer problems in two fluids—one solid domains. *Numerical Heat Transfer, Part B: Fundamentals*, 76(3):130–151, 2019.

[40] J. Alexandersen, N. Aage, C. Andreasen, and O. Sigmund. Topology optimisation for natural convection problems. *International Journal for Numerical Methods in Fluids*, 76:699–721, 12 2014.

[41] J. Alexandersen, O. Sigmund, K. E. Meyer, and B. Lazarov. Design of passive coolers for light-emitting diode lamps using topology optimisation. *International Journal of Heat and Mass Transfer*, 122:138–149, 02 2018.

[42] B. Lazarov, O. Sigmund, K. E. Meyer, and J. Alexandersen. Experimental validation of additively manufactured optimized shapes for passive cooling. *Applied Energy*, 226:330–339, 06 2018.

[43] G. H. Yoon. Topology optimization for stationary fluid–structure interaction problems using a new monolithic formulation. *International Journal for Numerical Methods in Engineering*, 82(5):591–616, 2010.

[44] E. Papoutsis-Kiachagias and K. Giannakoglou. Continuous adjoint methods for turbulent flows, applied to shape and topology optimization: Industrial applications. *Archives of Computational Methods in Engineering*, 23:255–299, 12 2014.

[45] Wikipedia. Turbulent Prandtl number — Wikipedia, the free encyclopedia. `http://en.wikipedia.org/w/index.php?title=Turbulent%20Prandtl%20number&oldid=793692372`, 2022. [Online; accessed 22-May-2022].

[46] B. S. Lazarov and O. Sigmund. Filters in topology optimization based on helmholtz-type differential equations. *International Journal for Numerical Methods in Engineering*, 86(6):765–781, 2011.

[47] B. Lazarov, F. Wang, and O. Sigmund. Length scale and manufacturability in density-based topology optimization. *Archive of Applied Mechanics*, 86:189–218, 01 2016.

[48] B. S. Lazarov and O. Sigmund. Sensitivity filters in topology optimisation as a solution to helmholtz type differential equation. 2009.

[49] S. Xu, Y. Cai, and G. Cheng. Volume preserving nonlinear density filter based on heaviside funtions. *Structural and Multidisciplinary Optimization*, 41:495–505, 04 2010.

[50] F. Wang, B. Lazarov, and O. Sigmund. On projection methods, convergence and robust formulations in topology optimization. *Structural and Multidisciplinary Optimization*, 43:767–784, 06 2011.

[51] A. Kawamoto, T. Matsumori, S. Yamasaki, T. Nomura, T. Kondoh, and S. Nishiwaki. Heaviside projection based topology optimization by a pde-filtered scalar function. *Structural and Multidisciplinary Optimization*, 44:19–24, 07 2011.

[52] E. M. Papoutsis-Kiachagias and K. C. Giannakoglou. An adjoint-based topology optimization framework for fluid mechanics and conjugate heat transfer in openfoam. 2020.

[53] K.T. Gkaragkounis, E.M. Papoutsis-Kiachagias, and K.C. Giannakoglou. The continuous adjoint method for shape optimization in conjugate heat transfer problems with turbulent incompressible flows. *Applied Thermal Engineering*, 140:351–362, 2018.

[54] E. M. Papoutsis-Kiachagias, E. A. Kontoleontos, A. S. Zymaris, D. I. Papadimitriou, and K. C. Giannakoglou. Constrained topology optimization for laminar and turbulent flows , including heat transfer. 2011.

[55] Openfoam. `https://www.openfoam.com/`. Accessed: 2022-06-06.

[56] Openfoam v1906. `https://www.openfoam.com/news/main-news/openfoam-v1906/numerics`. Accessed: 2022-06-06.

[57] National technical university of athens: School of mechanical engineering - lab. of thermal turbomachines - parallel cfd & optimization unit (pcopt). `http://velos0.ltt.mech.ntua.gr/research/index.html`. Accessed: 2022-06-06.

[58] C. B. Dilgen, S. B. Dilgen, D. R. Fuhrman, O. Sigmund, and B. S. Lazarov. Topology optimization of turbulent flows. *Computer Methods in Applied Mechanics and Engineering*, 331:363–393, 2018.

[59] P. Spalart and C. Rumsey. Effective inflow conditions for turbulence models in aerodynamic calculations. *Aiaa Journal - AIAA J*, 45:2544–2553, 10 2007.